Title
Stability and bounding of flow quantities in time-modulated convection

Permalink
https://escholarship.org/uc/item/5h483280

Author
Christopher, Todd

Publication Date
2021

Peer reviewed|Thesis/dissertation

UNIVERSITY OF CALIFORNIA SAN DIEGO

Stability and bounding of flow quantities in time-modulated convection

A dissertation submitted in partial satisfaction of the
requirements for the degree
Doctor of Philosophy

in

Engineering Sciences (Mechanical Engineering)

by

Todd W. Christopher

Committee in charge:

Professor Stefan Llewellyn Smith, Chair
Professor Patrick Diamond
Professor Padmini Rangamani
Professor Antonio Sánchez
Professor William Young

2021

The dissertation of Todd W. Christopher is approved, and it is acceptable in quality and form for publication on microfilm and electronically.

University of California San Diego

2021

DEDICATION

To my parents,

for feeding my curiosity with books as I grew up,

and to my wife,

for putting up with all the books.

EPIGRAPH

So, ultimately, in order to understand nature it may be necessary to have a deeper understanding of mathematical relationships. But the real reason is that the subject is enjoyable, and although we humans cut nature up in different ways, and we have different courses in different departments, such compartmentalization is really artificial, and we should take our intellectual pleasures where we find them.

—Richard Feynman

TABLE OF CONTENTS

LIST OF FIGURES

LIST OF TABLES

ACKNOWLEDGEMENTS

The mathematician T. W. Körner has written, “I believe that the making of proofs…is like the making of shoes. It is better taught by watching someone make a shoe in front of you than by trying to figure it out from books.” Even as an ardent bibliophile who has haunted Geisel library for years, from my experience as a graduate student at UCSD I must agree with Körner. I would only add that what applies to proofs in mathematics applies equally well to solving problems in applied mathematics, physics, and engineering.

I have been fortunate to sit at the feet of many master cobblers while pursuing my graduate studies. First and foremost has been my advisor, Professor Llewellyn Smith, who not only taught me much of the applied mathematics I would need for my research, but also demonstrated the habits, thoughts, and actions necessary to be a successful scientific researcher—all the things large and small that can only be picked up from extensive time observing and interacting with an expert. Professor Diamond, Professor Sánchez, and Professor Young, in addition to graciously agreeing to be on my dissertation committee, all taught inspiring courses, where mathematics and fluid dynamics were vividly brought to life as exciting endeavors full of challenges and rewards. Without these experiences, my shoemaking ability would be poorer indeed. Professor Rangamani was also kind enough to serve on my dissertation committee, and her practical advice was especially useful as I neared the end of my PhD.

Many fellow students at UCSD have contributed to enriching my time here. Ching Chang patiently answered my many questions through the years about navigating the graduate school bureaucracy. Once when I was away on the East Coast and forgot what time zone I was in, Ching still answered my phone call in his sleep to advise me on where to print a poster. Achal Mahajan and I spent countless hours taking classes, working on homework, and TAing together, and he was always willing to listen to my crazy ideas on things like how Green's functions and Fourier analysis should be taught. The students in the courses for which I was a teaching assistant taught me more than most of my other courses combined.

The true bedrock of support for all my undertakings in life, academic and otherwise, is my family. A conversation with my brother, who has always had a steadiness to balance my capriciousness, helped catalyze my entry into engineering. My parents provided an ideal environment for a kid interested in everything at the same time to mature into an adult still interested in everything at the same time, but eventually with a career track. The opportunity to pursue higher education and follow my passion in life is a privilege for which I am eminently thankful. And finally, my wife has gamely endured years of stacks of books and piles of notes appearing at random throughout our home and has served as a sounding board, fierce critic, wise counselor, and unconditional supporter when needed. She makes it all worthwhile.

Chapter 4, in part, is being prepared for submission for publication as "Linear and nonlinear stability of Rayleigh–Bénard convection with zero-mean modulated heat flux" by T. W. Christopher and S. G. Llewellyn Smith. The dissertation author was the primary investigator and author of this material.

Chapter 7, in part, has been published in *Physical Review Fluids*, "Bounding temperature dissipation in time-modulated Rayleigh Bénard convection" by T. W. Christopher and S. G. Llewellyn Smith, 2021, **6**, L051501 (American Physical Society). The dissertation author was the primary investigator and author of this material.

Appendix A, in full, has been published in the *Journal of Fluid Mechanics*, "Hollow vortex in a corner" by T. W. Christopher and S. G. Llewellyn Smith, 2021, **908**, R2 (Cambridge University Press). The dissertation author was the primary investigator and author of this material.

NSF award OCE-1829919 provided funding for the majority of the work contained in this dissertation. This project included collaboration with groups led by Professor Austin at the University of Minnesota Duluth and Professor Scotti at the University of North Carolina at Chapel Hill.

VITA

2011	B. S. in History, Technology, and Society, Georgia Institute of Technology
2015	B. S. in Mechanical Engineering, Georgia Institute of Technology
2018	M. S. in Engineering Sciences (Mechanical Engineering), University of California San Diego
2021	Ph. D. in Engineering Sciences (Mechanical Engineering), University of California San Diego

PUBLICATIONS

T. W. Christopher and S. G. Llewellyn Smith, 2021, Bounding temperature dissipation in time modulated Rayleigh–Bénard convection, *Phys. Rev. Fluids*, 6, L051501.

T. W. Christopher and S. G. Llewellyn Smith, 2021, Hollow vortex in a corner, *J. Fluid Mech.*, 908, R2.

ABSTRACT OF THE DISSERTATION

Stability and bounding of flow quantities in time-modulated convection

by

Todd W. Christopher

Doctor of Philosophy in Engineering Sciences (Mechanical Engineering)

University of California San Diego, 2021

Professor Stefan Llewellyn Smith, Chair

The daily cycle of heating and cooling from the rising and setting of the sun creates the potential for periodically-forced convection in the world's atmosphere and bodies of water. In this dissertation, we model a body of water experiencing daily heating from the sun and examine the onset of convection using linear and nonlinear stability analysis. We also find the first exact bound on a flow quantity in time-modulated convection. The setup considered consists of fluid between two surfaces that are infinite in the horizontal directions, with one of the surfaces heated in a time-varying manner. The most important parameters are the Rayleigh number, Ra, which captures the strength of the heating, and the nondimensional frequency of the time modulation, ω.

Radiative heating from the sun is modeled as a source term with exponential decay in the vertical. When confined to a thin layer near the surface, the effects of radiative heating may be approximated by an imposed temperature or heat flux boundary condition, and this approach forms the main focus of the dissertation. Each method of heating has time dependence to capture the sun's daily cycle. For stability analysis a sinusoidal time dependence is used, and for bounding results are found for a generic profile.

The stability results show that while the critical Rayleigh numbers for both linear and nonlinear stability increase with increasing modulation frequency, the linear and nonlinear stability thresholds show very different behavior at high modulation frequencies. As expected, the nonlinear stability threshold is always below the linear stability threshold. For the linear stability threshold, the ratio $\mathrm{Ra}\omega^{-3/2}$ or $\mathrm{Ra}\omega^{-2}$ approaches a constant, with the power of the frequency depending on the type of heating. This is found to match the result from considering a semi-infinite domain. For the nonlinear stability threshold, the growth of the Rayleigh number with the frequency is approximately linear, and no semi-infinite domain result is found. Beyond stability, we find an exact bound on the temperature dissipation that grows like $\sqrt{\mathrm{Ra}}$ and $\sqrt{\omega}$ in the large Ra and ω limits, respectively.

Chapter 1

Introduction

Does the daily heating of a lake by the sun lead to convection in the lake? If so, what are the important length scales revealed by stability analysis? What can be stated in a precise, mathematical manner about the flow variables involved? This dissertation seeks to answer these and related questions by investigating a variety of scenarios in convection and fluid dynamics. The study is motivated by observations of springtime warming in Lake Superior by Austin (2019), which indicate convection throughout the depth of the lake on the timescale of hours. The observations shown in Figure 1.1 demonstrate that on a typical day a temperature rise near the surface is followed by temperature rises throughout the water column, indicating the presence of convection.

Convection has a long and storied history in fluid dynamics, going back to the original observations by Bénard of convective cells in 1900 and the linear stability analysis by Rayleigh in 1916. The configuration with two infinitely large horizontal plates held at fixed temperatures with fluid between them is now called Rayleigh–Bénard (RB) convection, and this is the configuration used throughout this dissertation. Of the many possible aspects one could investigate in this convection scenario, perhaps the most basic is that of stability. For fluid that is initially quiescent, one determines the conditions under

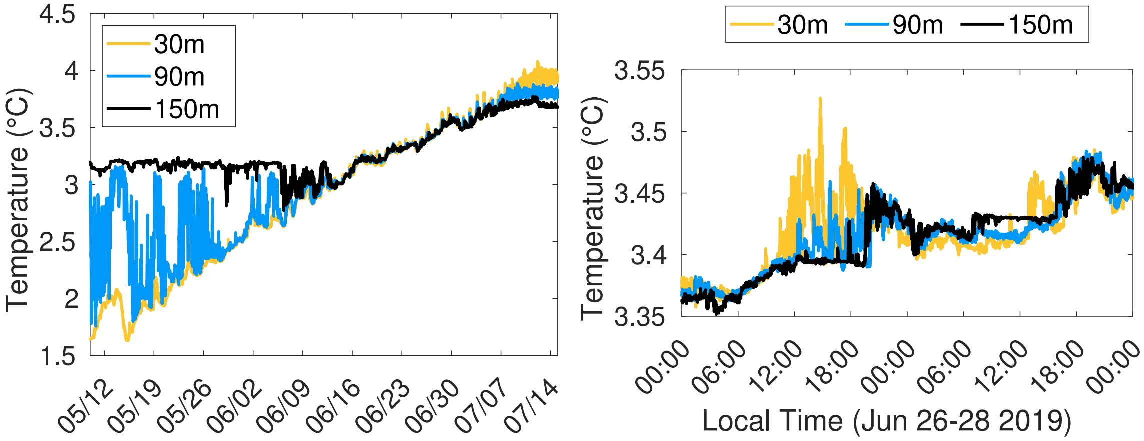

Figure 1.1: Observations in Lake Superior in 2019 (Austin, 2019; Austin, 2020). Left: Lake overturn occurs between May and July; Right: Observations over two days showing that a temperature rise at 30 m appears to propagate down to 90 m and then 150 m over the course of the day, with a relatively uniform temperature reached overnight.

which the fluid begins to move, which is termed the stability threshold. Once the fluid is in motion, describing the exact evolution of the flow is difficult, but in some cases we are still able to make precise, quantitative statements about the flow. For example, in RB convection it is sometimes possible to derive an exact bound on the heat transport between the two plates. These two aspects of convection, stability and bounding of flow quantities, will be treated in this dissertation. For stability, thresholds of linear and nonlinear stability are found and compared. For bounding of flow quantities, a bound is found on the temperature dissipation.

Instability occurs when the buoyancy effects from heating are stronger than the dissipative effects from viscosity and diffusion. For everyday liquids at everyday temperatures, this means instability is created by heating the fluid from the bottom to make the fluid less dense there, so that with strong enough heating the fluid particles begin to rise. In a lake that has just recently become ice-free, the water temperature will be between 0°C and 4°C, a regime in which water actually becomes denser as the temperature is increased, contrary to our normal experience. This means that, during springtime warming, heating at the surface of the lake has the potential to create an instability.

To model this situation, we consider fluid confined between two horizontal surfaces, just as in standard RB convection, but with time-dependent heating. For a relatively murky body of water, one can consider the radiative heating from the sun to be confined to a thin layer near the surface, in which case the heating would appear to reduce to a specified flux at the surface itself. Because it has not been previously addressed and is likely to capture the fundamental physics of radiative heating in a body of water, this is the case we focus on for the stability portion. A source term with true radiative heating and a modulated temperature boundary condition are also considered, with the bounding section using the latter for mathematical simplicity.

The remainder of this introduction serves as an outline of the dissertation. Broadly speaking, we first discuss convection in general and introduce the techniques of stability analysis and bounding with steady RB convection before treating stability and bounding of flow quantities in time-modulated convection. A brief description of each chapter is now given.

In Chapter 2, the important parameters and governing equations for convection in fluid dynamics are introduced. Dimensional analysis is used to discuss the physics of the important dimensionless parameters. This leads to a discussion of the difference between low and high frequency modulation, which will be addressed in depth in later chapters. Complications such as rotation and radiative heating are also discussed. Finally, the Boussinesq equations governing convection are presented and nondimensionalized.

In Chapter 3, the basic RB setup is reviewed. The techniques are introduced that will be used for the stability analysis and bounding of flow quantities, and they are applied to steady RB, both (i) to demonstrate the general procedure of each technique before proceeding to more complicated cases and (ii) to establish steady RB results for later reference. Special attention is paid to what does and does not carry over directly to cases with modulation.

In Chapter 4, the stability of a configuration with time-modulated heat flux or temperature at one boundary is investigated. Both linear and nonlinear stability are addressed. To determine the threshold for linear stability, the periodic nature of the heating allows the use of Floquet theory to decompose the solution into an exponentially growing and a periodic component, leading eventually to an eigenvalue problem with some similarities to the standard RB linear stability eigenvalue problem. A key difference, however, is that the instability is not necessarily stationary, as it is in standard RB, but may instead occur with an oscillating disturbance. The linear stability problem is solved numerically using expansions from Chebyshev spectral methods and Fourier series, truncating these expansions, and solving the resulting linear algebra eigenvalue problem with standard routines.

To determine the threshold for nonlinear stability, the energy method is used, which involves using variational calculus to find when the “energy” of the fluctuations (essentially the kinetic energy added to the square of the temperature) decays over time. One can find conditions for both a strong form of nonlinear stability named strong global stability, where the energy of the fluctuations always decays in time, and a weaker form named asymptotic stability, where the energy is allowed to grow during a period but must have net decay over the whole period.

Most work in modulated RB convection has focused on nonzero-mean modulation of the temperature, meaning the average of the temperature difference or heat flux between the two boundaries is nonzero. For example, researchers have performed linear stability analyses for zero-mean modulation of the temperature at the boundary without considering modulated flux, and have performed nonlinear stability analyses for a configuration with nonzero-mean modulation of the temperature, but not the heat flux. This dissertation extends past work to include these cases, with the novelty being that zero-mean modulation of the boundary heat flux is considered, and that linear and nonlinear stability thresholds are directly compared.

In Chapter 5, the low-frequency regime is analyzed more closely. For no-stress conditions with temperature modulation, the equations governing linear stability reduce to a decoupled set of Mathieu equations. The WKB approximation can then be used to determine the threshold for linear stability. This has been done before in Or (2001), but detailed results and comparisons to full solutions are given here. For other conditions, the governing equations are not decoupled, and a matrix WKB approach must be attempted. We present possible approaches for future researchers to build on, but we are not able to solve for the stability threshold in these more difficult cases.

In Chapter 6, the high-frequency regime is considered with both boundary modulation and modulated radiative heating. A high modulation frequency is equivalent to a very deep body of water, as in either case the effects of the forcing are confined to a boundary layer near the surface. Mathematically, both cases are treated in a semi-infinite domain. The relevant length scale is no longer the depth of the water but is instead what could be termed a thermal Stokes layer, constructed from the modulation frequency and the thermal diffusivity. We treat radiative heating and investigate the dependence of the critical Rayleigh number on the penetration depth of the radiative heating. As the heat penetrates less and less into the body of water, we expect the results to closely resemble those from the case of an imposed boundary heat flux, which is what we find for linear stability.

In Chapter 7, bounding of flow quantities is treated. The background technique is used to find an exact bound on the temperature dissipation rate for the standard two-plate RB setup, but with the temperature of one boundary varying in time. In steady RB convection, researchers generally attempt to bound the Nusselt number, which captures the relative strength of convective to conductive heat transfer. In time-dependent convection, the Nusselt number becomes more complicated, and the natural quantity to bound is the temperature dissipation (the two-norm of the gradient of the temperature, $||\nabla T||_2^2$). The novelty in this result is that it is the first treatment of time-dependent forcing in convection using the background method, building on the bound on shear stress for time-dependent shear flow in Marchioro (1994).

The optimal bound must in general be found numerically, but an asymptotic analysis can be carried out for high frequency ω and large Rayleigh number Ra. There are two distinct regimes for small and large ω. In the small ω limit, the bound reduces to the same bound in the steady case, whereas in the large ω limit, the bound grows like $\sqrt{\omega}$. For large Rayleigh numbers with fixed ω, the bound on temperature dissipation grows like $\sqrt{\mathrm{Ra}}$, as it does in the steady case.

In Chapter 8, we conclude by summarizing the important results in the dissertation and discussing possible avenues of future work. Though the work in this dissertation is inspired by observations of lake convection, the scenarios considered are fundamental fluid dynamics problems abstracted away from the lake setting. Different possible ways of achieving more direct applicability to real-world lake convection are discussed, such as directly incorporating rotation, considering different modulation profiles, and relating the bound more directly to the Nusselt number.

In Appendix A, work inspired from geophysical flow considerations but unrelated to convection is covered. A solution is found for a stationary hollow vortex in a straining flow in a corner of arbitrary angle, which might describe a sharp bend in a river, for example. Complex analysis and conformal mapping techniques are used in conjunction with the Schottky–Klein prime function to construct the stationary hollow vortex boundaries, extending previous work which treated only the case of a hollow vortex in uniform flow near a wall, which can be thought of as a corner of angle π.

Chapter 2

Equations and Parameters

In this chapter, we first discuss the important scales and parameters in modulated convection, with an emphasis on the physics involved. We then present the governing Boussinesq equations and carry out the process of nondimensionalization. The relevant physical quantities and dimensionless parameters are summarized in Table 2.1, and their approximate values are listed in Table 2.2.

2.1 Steady RB scales and parameters

From the physics of convection, we expect a competition between (i) the buoyant force created from temperature differences that lead to density differences and (ii) the dissipation of energy by κ and ν, the thermal diffusivity and momentum diffusivity, respectively. To compare these quantitatively, we construct characteristic time scales for each, and then the phenomenon acting on a smaller time scale is expected to dominate.

The time scale for diffusion of thermal energy and momentum is

$$t_{\mathrm{diff}} = \frac{d^2}{\sqrt{\kappa\nu}}, \tag{2.1}$$

Table 2.1: Parameters and variables corresponding to different configurations.

No Modulation	Ra	$\frac{\text{buoyancy}}{\text{diffusion}}$	$\frac{\alpha g T_{\text{sc}} d^3}{\kappa \nu}$
	Pr	$\frac{\text{momentum diffusivity}}{\text{thermal diffusivity}}$	$\frac{\nu}{\kappa}$
Modulation	ω	$\frac{\text{oscillation}}{\text{diffusion}}$ or $\frac{\text{lake depth}}{\text{boundary layer size}}$	$\frac{\omega_* d^2}{\kappa}$
	Ra_∞	Ra for very deep lake	$\frac{\alpha g T_{\text{sc}} \sqrt{\kappa}}{\nu \omega_*^{3/2}}$
Radiative Heating	γ	$\frac{\text{lake depth}}{\text{radiation penetration depth}}$	$\frac{d}{d_{\text{rad}}}$
Rotation	Ro	$\frac{\text{diffusion}}{\text{rotation}}$	$\frac{\kappa}{d^2 f}$

d: water depth
ω_*: frequency of modulation
κ: thermal diffusivity
k: thermal conductivity
S_0: incoming radiation
f: Coriolis coefficient
ν: momentum diffusivity
α: coef. of thermal expansion
T_{sc}: temperature scale
d_{rad}: radiation e-folding depth
g: gravitational acceleration

where d is the depth of the water. A time scale for buoyancy may be constructed from the buoyant force acting on a fluid particle. The volume change for a volume V experiencing a temperature change T_{sc} is $V\alpha T_{\mathrm{sc}}$. The density change is

$$\delta\rho = -\rho\alpha T_{\mathrm{sc}}. \tag{2.2}$$

The buoyancy force arises from the difference in density between the particle and its surroundings, and is

$$F_b = -V\rho\alpha T_{\mathrm{sc}} g, \tag{2.3}$$

where g is the acceleration due to gravity. We see that a characteristic acceleration is then $\alpha T_{\mathrm{sc}} g$, from which we can use the length scale d to get the time scale for buoyancy of

$$t_b = \sqrt{\frac{d}{\alpha T_{\mathrm{sc}} g}}, \tag{2.4}$$

which is the time scale for the fluid parcel to traverse the depth of the water with constant acceleration $\alpha g T_{\mathrm{sc}}$. We now compare the diffusive time scale to the buoyancy time scale to find

$$\frac{t_{\mathrm{diff}}}{t_b} = \sqrt{\frac{\alpha g T_{\mathrm{sc}} d^3}{\kappa\nu}}. \tag{2.5}$$

The Rayleigh number is traditionally defined as the square of this ratio,

$$\mathrm{Ra} \equiv \frac{\alpha g T_{\mathrm{sc}} d^3}{\kappa\nu}. \tag{2.6}$$

When the time scale for buoyancy is much shorter than the time scale for diffusion, so that the Rayleigh number is large, we expect buoyancy to dominate and for the fluid to be set in convective motion. When the time scale for diffusion is much shorter than the time scale for buoyancy, we instead expect the buoyancy difference to be quickly dissipated so that the fluid remains still.

For RB convection with an imposed temperature difference, the obvious candidate for T_{sc} is the imposed temperature difference. When instead a heat flux is imposed, a temperature scale can be constructed from the heat flux. If the heat flux is imposed at a boundary through an equation of the form $k\partial_z T = S_0$, then the appropriate temperature scale is $S_0 d/k$.

The ratio of the momentum diffusivity to the thermal diffusivity is also important. This ratio is known as the Prandtl number,

$$\mathrm{Pr} \equiv \frac{\nu}{\kappa}. \tag{2.7}$$

2.2 Modulation parameters

When time modulation is introduced into RB convection, new time and length scales are possible. The characteristic frequency of modulation ω_* can be compared with the time scale for diffusion of thermal energy to define a new parameter,

$$\omega \equiv \frac{\omega_* d^2}{\kappa}, \tag{2.8}$$

which we will call the nondimensional modulation frequency. From ω we see that a high modulation frequency has the same effect as a very deep lake, with both leading to high ω, and in fact this parameter can equally well be thought of as the square of the ratio of d to the diffusive length scale $\sqrt{\kappa/\omega_*}$.

For an infinitely deep body of water, d ceases to be a relevant length scale. Instead, a length scale must be created from the thermal diffusivity and momentum diffusivity. Using only the thermal diffusivity leads to a length scale of $\sqrt{\kappa/\omega_*}$. With this length scale in place of d, the Rayleigh number becomes

$$\mathrm{Ra}_\infty \equiv \frac{\alpha g T_{\mathrm{sc}} \kappa^{1/2}}{\omega_*^{3/2} \nu}, \tag{2.9}$$

which we expect to be the important control parameter for a semi-infinite domain. We note that for an imposed temperature, this is equivalent to $\mathrm{Ra}/\omega^{3/2}$. For an imposed heat flux, the temperature scale involves d as well, so that Ra/ω^2 is equivalent to Ra_∞. As d becomes larger, we expect the separate effects of Ra and ω to be captured by Ra_∞. As shown below, this is exactly what we find for linear stability.

2.3 Radiation and rotation parameters

Radiative heating from the sun can be described using the equation for the intensity of light as a function of depth,

$$I(z) = S_0 \mathrm{e}^{z/d_{\mathrm{rad}}}. \tag{2.10}$$

The change in intensity with depth transfers thermal energy to the water, and is

$$\frac{\mathrm{d}I}{\mathrm{d}z} = \frac{S_0 \mathrm{e}^{z/d_{\mathrm{rad}}}}{d_{\mathrm{rad}}}, \tag{2.11}$$

which is the energy per time per volume transferred to the fluid. By relating this to the change in energy of a fluid parcel $\rho c \mathrm{d}T/\mathrm{d}t$, we find the temperature scales $S_0 d_{\mathrm{rad}}/k$ or $S_0 d/k$, which may be used to find the Rayleigh number. A new parameter that arises is the ratio of the e-folding scale of the radiative heating to the depth of the lake,

$$\gamma \equiv \frac{d_{\mathrm{rad}}}{d}. \tag{2.12}$$

Accounting for rotation introduces a new time scale associated with $f = \Omega \sin\theta$, where Ω is the frequency of the earth's rotation and θ is the latitude. The ratio of the inertial term to the Coriolis term leads to the Rossby number

$$\mathrm{Ro} \equiv \frac{1}{\tau f}, \tag{2.13}$$

where τ is the time scale chosen. If we choose the time scale for diffusion, we have $\mathrm{Ro} = \kappa/(d^2 f)$, whereas if we choose the time scale from the fundamental frequency of forcing ω_*, we have $\mathrm{Ro} = \omega_*/f$. If the time scale for diffusion is used, the Rossby number will be low, indicating that rotation is important, though it should be noted that one would have to draw this conclusion for most RB setups because of how small κ is. If the time scale from the forcing frequency is used, however, the Rossby number is $O(1)$, indicating that rotation may or may not play a large role. To limit the number of parameters, we defer treating the case with rotation to later work. In standard RB, rotation has a stabilizing influence on linear stability, and we would therefore expect similar behavior with time-modulated forcing. However, including rotation in the linear stability analysis requires the inclusion of extra variables, namely the components of vorticity. This enlarges the eigenvalue problem for linear stability, and in the time-modulated case the matrices are too ill-conditioned to return results.

For nonlinear stability, the standard techniques involve forming an inner product of the momentum equation with the velocity, which immediately eliminates the Coriolis term $2\boldsymbol{\Omega} \times \boldsymbol{u}$, and therefore all the nonlinear stability results found below hold also for the case with rotation. In order to directly incorporate rotation into nonlinear stability, a more complicated energy must be formed. Unfortunately this leads only to conditional stability results, so we do not attempt to use a more complicated energy to account for rotation here.

2.4 Values of properties and parameters

The relevant properties of water at 3°C along with the other relevant properties in the lake are listed in Table 2.2. We see that the expected Rayleigh number is large, though we do not yet have any context for the expected stability threshold. In Chapter 3, we will see that the Rayleigh number threshold for instability in steady RB is $O(10^3)$, so this would appear to be high, but we must keep in mind that modulation means that the Rayleigh number captures only the maximum of the forcing strength, and that the forcing strength is otherwise lower throughout a forcing period. We therefore might expect the threshold to be higher, which is indeed what we find below. The nondimensional frequency is large, so that in nondimensional terms we are in the very deep or high frequency regime. The parameter γ comparing the radiation penetration depth to the depth of the lake is also small, indicating that treating the incoming radiation as a surface heat flux could be a good approximation to true radiative heating, and we demonstrate this for linear stability on a semi-infinite domain in Chapter 6.

2.5 Governing equations

We use the Navier-Stokes equations in the Boussinesq approximation to model the behavior of the fluid. We present the equations in their full generality here, though we will present the relevant simplified equations again in each section. The equations are

$$\partial_{t_*}\boldsymbol{u}_* + \boldsymbol{u}_* \cdot \nabla_* \boldsymbol{u}_* = -\frac{\nabla_* p_*}{\rho} - g\left[1 - \alpha(T_* - T_{\mathrm{R}})\right]\boldsymbol{e}_z + \nu \nabla_*^2 \boldsymbol{u}_*, \tag{2.14}$$

$$\nabla_* \cdot \boldsymbol{u}_* = 0, \tag{2.15}$$

$$\partial_{t_*} T_* + \boldsymbol{u}_* \cdot \nabla_* T_* = \kappa \nabla_*^2 T_* + \frac{S_*(t_*)\mathrm{e}^{z_*/d_{\mathrm{rad}}}}{d_{\mathrm{rad}}}, \tag{2.16}$$

Table 2.2: Approximate values for properties relevant to convection in a lake at 3°C at a latitude of 47.5°N. (First five properties calculated using Holmgren (2006), which uses data from the International Association for the Properties of Water and Steam.)

Property	Value	Units
ν	$1.6(10)^{-6}$	m^2/s
κ	$1.4(10)^{-7}$	m^2/s
α	$-1.6(10)^{-5}$	1/°C
k	0.57	W/(m°C)
ρ	1000	kg/m^3
d	100–300	m
d_{rad}	3–10	m
S_0	200-1000	W/m^2
ω_*	$7(10)^{-5}$	rad/s
f	10^{-4}	rad/s
Pr	11	
Ra	10^{20}	
ω	10^7	
γ	0.05	

where $S_*(t_*+2\pi/\omega_*) = S_*(t_*)$, so that the fundamental frequency of the bulk heating term is ω_*. The variable $\boldsymbol{u}_*$ is the velocity, T_* is the temperature, p_* is the pressure, t_* is time, and z_* is the vertical position component. The constant T_{R} is a reference temperature, ρ is the density at the reference temperature, d_{rad} is the e-folding scale of the radiation, and α is the coefficient of thermal expansion at the reference temperature. In this section we take the domain as $-d \leq z \leq 0$, though in other sections we will use $0 \leq z \leq d$.

Different boundary conditions are considered. For the velocity, the boundary conditions are no-penetration and then a choice of no-slip or no-stress at both the top and bottom. For the temperature, the following boundary conditions are considered:

$$\text{Top } (z_* = 0) : \begin{cases} T_* = f_*(t_*) & \text{specified temperature} \\ k\partial_{z_*} T_* = k f_*(t_*)/d & \text{bulk heating \& specified flux} \end{cases} \tag{2.17}$$

$$\text{Bottom } (z_* = -d): \begin{cases} T_* = T_\mathrm{R} & \text{specified temperature} \\ k\partial_{z_*} T_* = 0 & \text{no flux,} \end{cases} \tag{2.18}$$

where $f_*(t_* + 2\pi/\omega_*) = f_*(t_*)$ so that the fundamental frequency is ω_*, and

$$T_\mathrm{R} \equiv \begin{cases} \mathrm{mean}(f_*(t_*)) & \text{specified temperature} \\ \mathrm{mean}\left(f_*(t_*) d/k\right) & \text{bulk heating \& specified flux.} \end{cases} \tag{2.19}$$

Most fluids in most circumstances expand when heated, so in most of the literature the fluid is heated from the bottom. Heating at the top in the anomalous regime of water is equivalent to heating at the bottom outside of that regime.

We choose scales L, U, τ, and T_sc for length, velocity, time, and temperature to define the nondimensional variables

$$\boldsymbol{x} \equiv \frac{\boldsymbol{x}_*}{L}, \quad \boldsymbol{u} = \frac{\boldsymbol{u}_*}{U}, \quad t \equiv \frac{t_*}{\tau}, \quad T \equiv \frac{T_* - T_\mathrm{R}}{T_\mathrm{sc}}, \quad S(t) \equiv \frac{S_*(t)}{S_0}, \quad f(t) \equiv \frac{f_*(t) - T_\mathrm{R}}{f_0}, \tag{2.20}$$

where $S_0 = \max S_*(t)$ and $f_0 = \max f_*(t)$. We set $U = L/\tau$, fold the constant term due to gravity into an appropriately scaled pressure term, and choose L and τ depending on the case under consideration,

$$L \equiv \begin{cases} d & \text{finite domain} \\ \sqrt{\kappa/\omega_*} & \text{semi-infinite domain} \end{cases} \tag{2.21}$$

and

$$\tau \equiv \begin{cases} d^2/\kappa & \text{finite domain} \\ \omega_*^{-1} & \text{semi-infinite domain.} \end{cases} \tag{2.22}$$

For a finite domain, any set of choices can be made. For all cases, we have $\tau = L^2/\kappa$. Our choice of the temperature scale depends on where the forcing occurs,

$$T_{\mathrm{sc}} = \begin{cases} f_0 & \text{boundary forcing} \\ S_0 L/k & \text{bulk heating.} \end{cases} \tag{2.23}$$

The resulting nondimensional governing equations are

$$\partial_t \boldsymbol{u} + \boldsymbol{u}\cdot\nabla\boldsymbol{u} = -\nabla p + \mathrm{Ra}\,\mathrm{Pr}\, T\boldsymbol{e}_z + \mathrm{Pr}\nabla^2\boldsymbol{u}, \tag{2.24}$$

$$\nabla\cdot\boldsymbol{u} = 0, \tag{2.25}$$

$$\partial_t T + \boldsymbol{u}\cdot\nabla T = \nabla^2 T + \frac{S(t)}{\gamma}\mathrm{e}^{z/\gamma}, \tag{2.26}$$

where for boundary forcing the source term $S(T)$ is set to zero. The parameters are defined as

$$\mathrm{Ra} \equiv \frac{\alpha g T_{\mathrm{sc}} L^3}{\nu\kappa}, \quad \mathrm{Pr} \equiv \frac{\nu}{\kappa}, \quad \gamma \equiv \frac{d_{\mathrm{rad}}}{L}, \quad \omega \equiv \frac{\omega_* L^2}{\kappa}. \tag{2.27}$$

The boundary conditions become

$$\text{Top } (z=0): \begin{cases} T = f(t) & \text{specified temperature} \\ \partial_z T = f(t) & \text{bulk heating \& specified flux} \end{cases} \tag{2.28}$$

and

$$\text{Bottom } (z=-1): \begin{cases} T = 0 & \text{specified temperature} \\ \partial_z T = 0 & \text{no flux.} \end{cases} \tag{2.29}$$

The fundamental period of the forcing term becomes 2π in the semi-infinite case and $2\pi/\omega$ in the finite case. For radiative heating, a more general boundary condition could be used to connect the water with the atmosphere above it, such as a Newtonian condition, but this would require knowledge of a parameter characterizing that interaction.

As the e-folding scale of the radiative heating goes to zero, the configuration reduces to an imposed heat flux setup. In this limit, $\gamma \to 0$, and the source term is nonzero only in an $O(\gamma)$ region while still imparting all of the incoming heat to the water. This is equivalent to a source term of zero and a boundary condition specifying the incoming heat flux. Chapter 6 shows that these two cases do in fact give equivalent linear stability results in this limit. For this reason, in this dissertation we will deal mostly with the modulated heat flux as representative of radiative heating.

Chapter 3

Stability and Bounding in Steady RB

In this chapter, we review steady RB convection and introduce the tools of linear stability analysis, nonlinear stability analysis, and bounding of flow quantities. We only include details when they will not be given later, as our main goals are to introduce the techniques first in a familiar setting and to derive results to refer back to when we examine more complicated scenarios.

3.1 Setup

The setup for steady RB convection is fluid confined between two surfaces infinitely large in the horizontal directions. In this chapter we will assume temperatures are fixed at the surfaces because that is the best known case. After nondimensionalizing, the equations are (2.24)–(2.26) but with the source term in the temperature equation set to zero. The boundary conditions for temperature are the imposed temperatures, and the boundary conditions for velocity may be taken as no-slip or no-stress. The equations are therefore

$$\partial_t \boldsymbol{u} + \boldsymbol{u} \cdot \nabla \boldsymbol{u} = -\nabla p + \mathrm{Ra}\,\mathrm{Pr}\, T \boldsymbol{e}_z + \mathrm{Pr} \nabla^2 \boldsymbol{u}, \tag{3.1}$$

$$\nabla \cdot \boldsymbol{u} = 0, \tag{3.2}$$

$$\partial_t T + \boldsymbol{u} \cdot \nabla T = \nabla^2 T, \tag{3.3}$$

with temperature boundary conditions

$$T(0) = 1, \quad T(1) = 0. \tag{3.4}$$

The velocity satisfies a no-penetration boundary condition at both surfaces along with either a no-slip or no-stress condition. For no-slip conditions, $\boldsymbol{u} = 0$. For no-stress conditions, $\partial_z u = 0$ and $\partial_z v = 0$; then (3.2) leads to $\partial_z^2 w = 0$.

3.2 Linear stability

To find the linear stability threshold, we choose a base state and then determine what happens to small perturbations of the base state. In linear stability, we ignore all products of perturbations and assume perturbations depend on time through an exponential term. If small perturbations decay, the state is deemed stable, and if small perturbations grow, the state is deemed unstable. If perturbations neither grow nor decay, then the state is referred to as marginally stable. The first linear stability analysis for convection was presented in Rayleigh (1916), and a thorough treatment was given by Chandrasekhar (1961). We use the same procedure but take advantage of modern computing to solve the eigenvalue problem resulting from the linear stability analysis.

The temperature profile for the base state with no motion is determined by (3.3) with $\boldsymbol{u}$ set equal to zero. The result is

$$T_{\mathrm{B}}(z) = 1 - z. \tag{3.5}$$

We let $\boldsymbol{U} = (U, V, W)$ stand for the velocity perturbation and set

$$T(\boldsymbol{x}, t) = T_{\mathrm{B}}(z) + \Theta(\boldsymbol{x}, t), \tag{3.6}$$

where Θ is the temperature perturbation. We write the pressure as $p = p_{\mathrm{B}} + P$. Substituting these forms into the governing equations and neglecting products of perturbations leads to

$$\partial_t \boldsymbol{U} = -\nabla P + \mathrm{Ra}\,\mathrm{Pr}\ \Theta \boldsymbol{e}_z + \mathrm{Pr} \nabla^2 \boldsymbol{U}, \tag{3.7}$$

$$\nabla \cdot \boldsymbol{U} = 0, \tag{3.8}$$

$$\partial_t \Theta + W \partial_z T_{\mathrm{B}} = \nabla^2 \Theta, \tag{3.9}$$

where $\partial_z T_{\mathrm{B}} = 1$ in this case but not in more complicated cases. Taking the double curl of (3.7) and then isolating the z component leads to a system in W and Θ alone,

$$\partial_t \nabla^2 W = \mathrm{Ra}\,\mathrm{Pr}\ \nabla_{\mathrm{H}}^2 \Theta + \mathrm{Pr} \nabla^4 W, \tag{3.10}$$

$$\partial_t \Theta - W = \nabla^2 \Theta. \tag{3.11}$$

The boundary conditions satisfied by the perturbations are $\Theta = 0$, $W = 0$, and $\partial_z W = 0$ for no-slip conditions (from incompressibility) or $\partial_z^2 W = 0$ for no-stress conditions. We now assume normal modes in the horizontal directions and an exponential time dependence so that we have

$$W(\boldsymbol{x},t) = \mathrm{e}^{\mathrm{i}k_x x}\mathrm{e}^{\mathrm{i}k_y y}\mathrm{e}^{\mu t}w(z), \tag{3.12}$$

$$\Theta(\boldsymbol{x},t) = \mathrm{e}^{\mathrm{i}k_x x}\mathrm{e}^{\mathrm{i}k_y y}\mathrm{e}^{\mu t}\theta(z), \tag{3.13}$$

where k_x and k_y are real and μ is complex, and we let $k^2 = k_x^2 + k_y^2$. Equations (3.10) and (3.11) become

$$\mu L w = -\mathrm{Ra}\,\mathrm{Pr}\,k^2\theta + \mathrm{Pr} L^2 w, \tag{3.14}$$

$$\mu\theta - w = L\theta, \tag{3.15}$$

where the operator $L = \partial_z^2 - k^2$. This is an eigenvalue problem. Either Ra or μ can be treated as the eigenvalue. It so happens that for steady RB one can show that the imaginary part of μ is zero at the stability threshold, a situation often called exchange of stabilities. In more complicated cases this is not possible, and when the base state depends on time we will see that the appropriate analog of μ often has an imaginary part of 1/2. In all cases, if we take the real part of μ to be zero and specify its imaginary part, we are left with an eigenvalue problem for Ra as a function of k and Pr giving marginal stability. The critical Rayleigh number for fixed Pr is the minimum Ra over all possible k.

In order to solve the eigenvalue problem, we must in general resort to numerical methods. For the special case of no-stress boundaries and specified temperature, sine functions serve as eigenfunctions and an analytical result is possible. For all other cases this is not possible. Throughout this dissertation we use Chebyshev spectral methods to discretize in space, meaning the variables are expressed in a basis of Chebyshev polynomials. There are a variety of ways to apply Chebyshev spectral methods, and these are discussed in more detail in Chapter 4. One method involves turning the unknown vari-

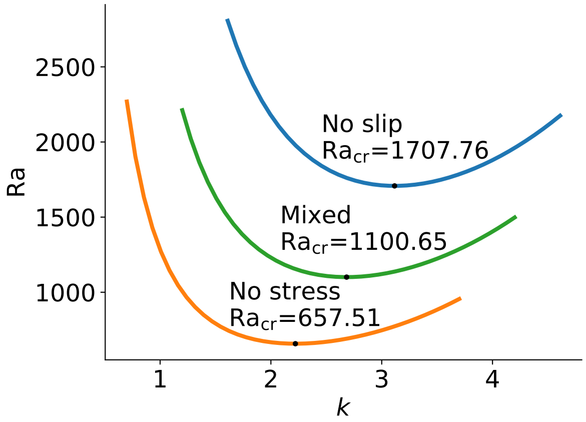

Figure 3.1: Curves of marginal stability for different boundary conditions in steady RB convection. The critical Rayleigh number is noted with a dot for each case and written above the curve.

ables w and θ into vectors of their values at Chebyshev grid points. In this method, the differential operators become matrices, and the boundary conditions are incorporated into the matrices.

When this method is applied, the resulting linear algebra eigenvalue problem is

$$\begin{pmatrix} \mu \boldsymbol{L} - \mathrm{Pr}\boldsymbol{L}^2 & \boldsymbol{0} \\ \boldsymbol{I} & \boldsymbol{L} - \mu \boldsymbol{I} \end{pmatrix} \begin{pmatrix} \boldsymbol{w} \\ \boldsymbol{\theta} \end{pmatrix} = \mathrm{Ra} \begin{pmatrix} \boldsymbol{0} & -\mathrm{Pr}k^2 \boldsymbol{I} \\ \boldsymbol{0} & \boldsymbol{0} \end{pmatrix} \begin{pmatrix} \boldsymbol{w} \\ \boldsymbol{\theta} \end{pmatrix} \tag{3.16}$$

By sweeping through k, a curve of marginally stable Rayleigh numbers is found. The curves of marginal stability are shown in Figure 3.1. Because exchange of stabilities can be shown to apply, $\mu = 0$, and Pr drops out of the eigenvalue problem, so these results hold for all Pr. These results will be important for comparison with the more complicated cases considered in this dissertation.

When we perform a linear stability analysis of time-modulated convection below, we will follow the same general procedure, but the non-autonomous nature of the differential equations will necessitate the use of Floquet theory. The resulting eigenvalue problem will entail a system of coupled sixth order equations rather than a single sixth order system, and the linear algebra eigenvalue problem will therefore be much larger than the corresponding problem in steady RB convection.

3.3 Nonlinear stability

The process for determining nonlinear stability proceeds similarly to the process for determining linear stability, but the perturbations may be of arbitrary size and are therefore termed fluctuations. Whereas linear stability finds a Rayleigh number above which instability is assured, nonlinear stability finds a Rayleigh number below which stability is assured. If the Rayleigh numbers for linear and nonlinear stability are different, potential instabilities occurring between the two are called subcritical instabilities. As we will see in this section, for steady RB the linear and nonlinear thresholds coincide. For cases with modulation, that is no longer necessarily true. The method of nonlinear stability analysis is explained in Straughan (2013), which also details a wide variety of nonlinear stability calculations.

The starting equations are (3.1)–(3.3). We take a base state of no motion and decompose the variables to separate the base state from the fluctuations. The velocity fluctuation is taken to be $\boldsymbol{u}(\boldsymbol{x},t)$, and the temperature fluctuation is $\theta(\boldsymbol{x},t)$, so that

$$T(\boldsymbol{x},t) = T_{\mathrm{B}}(z,t) + \theta(\boldsymbol{x},t). \tag{3.17}$$

For nonlinear stability we use the rescaled temperature variable

$$\phi \equiv \theta R, \tag{3.18}$$

where $R \equiv \sqrt{\mathrm{Ra}}$. The equations become

$$\mathrm{Pr}^{-1}\left(\partial_t \boldsymbol{u} + \boldsymbol{u}\cdot\nabla\boldsymbol{u}\right) = R\phi\boldsymbol{e}_z + \nabla^2\boldsymbol{u}, \tag{3.19}$$

$$\partial_t\phi + \boldsymbol{u}\cdot\nabla\phi = wR + \nabla^2\phi. \tag{3.20}$$

We define the energy as

$$E(t) \equiv \left(\frac{\|\boldsymbol{u}\|_2^2}{2\mathrm{Pr}} + \frac{\|\phi\|_2^2}{2}\right), \tag{3.21}$$

which upon taking a time derivative leads to

$$E'(t) = IR - D, \tag{3.22}$$

where

$$I \equiv 2\int_V w\phi \mathrm{d}V, \tag{3.23}$$

$$D \equiv \|\nabla\boldsymbol{u}\|_2^2 + \|\nabla\phi\|_2^2, \tag{3.24}$$

and the norms are

$$\|\phi\|_2^2 = \int_V \phi^2\mathrm{d}V, \quad \|\nabla\phi\|_2^2 = \int_V |\nabla\phi|^2\mathrm{d}V, \quad \|\nabla\boldsymbol{u}\|_2^2 = \int_V \frac{\partial u_j}{\partial x_k}\frac{\partial u_j}{\partial x_k}\mathrm{d}V. \tag{3.25}$$

Now we turn the evolution equation for the energy into an inequality by defining

$$\frac{1}{R_E} \equiv \max\left(\frac{I}{D}\right) \tag{3.26}$$

so that (3.22) becomes

$$E'(t) \leq -D\left(\frac{R_E - R}{R_E}\right) \tag{3.27}$$

From Poincaré's inequality, we have $D \geq \alpha_1 E$, with $\alpha_1 \geq 0$, so that

$$E'(t) \leq -\alpha_1 \left(\frac{R_E - R}{R_E} \right) E(t). \tag{3.28}$$

Integrating shows that the energy satisfies

$$E(t) \leq E(0) \exp \left\{ -\alpha_1 \left(\frac{R_E - R}{R_E} \right) t \right\}. \tag{3.29}$$

From (3.29) we see that $R < R_E$ leads to exponential decay of the energy, which we will refer to as energy stability or more specifically strong global stability. We see that this holds for any $E(0) < \infty$, which is termed unconditional stability. The energy stability threshold is $R = R_E$. Nonlinear stability with the energy method is a stronger notion than linear stability because the energy method accounts for fluctuations of any size and is not limited to small perturbations.

Finding the energy stability threshold requires solving for R_E in (3.26) using variational calculus methods. To do so, we must solve

$$\delta \left(\frac{I}{D} \right) = 0. \tag{3.30}$$

The quotient rule implies

$$\delta I - \frac{I}{D} \delta D = 0, \tag{3.31}$$

and since by assumption I/D is at its maximum value of $1/R_E$, (3.30) is equivalent to

$$R_E \delta I - \delta D = 0. \tag{3.32}$$

To enforce incompressibility, we use a Lagrange multiplier $\lambda(\boldsymbol{x})$ and write

$$\delta\left(R_E I - D - \int_V \lambda(\boldsymbol{x})\nabla\cdot\boldsymbol{u}\mathrm{d}V\right) = 0. \tag{3.33}$$

Each term is an integral that can be written as

$$I_F = \int_V F(\boldsymbol{u},\phi,\nabla\boldsymbol{u},\nabla\phi)\mathrm{d}V. \tag{3.34}$$

Application of the variational derivative operator then leads to

$$\delta I_F = \int_V\left(\frac{\partial F}{\partial u_k} - \frac{\partial}{\partial x_i}\left(\frac{\partial F}{\partial(\partial_i u_k)}\right)\right)\epsilon\eta_k\mathrm{d}V + \int_V\left(\frac{\partial F}{\partial \phi} - \frac{\partial}{\partial x_i}\left(\frac{\partial F}{\partial(\partial_i \phi)}\right)\right)\epsilon\eta_k\mathrm{d}V, \tag{3.35}$$

where η_k and η_ϕ are the arbitrary variations of u_k and ϕ, respectively, as $\epsilon\to 0$. When carried out for each term in (3.33), the results are

$$\delta I = \int_V 2\epsilon(\eta_\phi w + \eta_w\phi)\mathrm{d}V, \tag{3.36}$$

$$\delta D = -\int_V 2\epsilon\left(\eta_k\nabla^2 u_k\mathrm{d}V + \eta_\phi\nabla^2\phi\right)\mathrm{d}V, \tag{3.37}$$

$$\delta\int_V \lambda(\boldsymbol{x})\nabla\cdot\boldsymbol{u}\mathrm{d}V = -\int_V \epsilon\eta_k\partial_k\lambda\mathrm{d}V. \tag{3.38}$$

Using these in (3.33) leads to

$$\int_V\left[\eta_\phi(R_E w + \nabla^2\phi) + \eta_k(R_E\delta_{k3}\phi + \nabla^2 u_k + \partial_k p)\right]\mathrm{d}V = 0, \tag{3.39}$$

where we have defined $p\equiv\lambda/2$. The variations η_ϕ and η_k are arbitrary, which means the rest of the integrands must be zero, leading to

$$R_E \delta_{k3} \phi + \nabla^2 u_k + \partial_k p = 0, \tag{3.40}$$

$$R_E w + \nabla^2 \phi = 0. \tag{3.41}$$

Transforming back to θ gives

$$\mathrm{Ra}_E \theta \boldsymbol{e}_z + \nabla^2 \boldsymbol{u} + \nabla p = 0, \tag{3.42}$$

$$w + \nabla^2 \phi = 0, \tag{3.43}$$

where $\mathrm{Ra}_E = R_E^2$, which is identical to the eigenvalue problem for linear stability from (3.7)–(3.9) but without the time derivatives, which can be ignored because exchange of stabilities holds for steady RB. The energy stability threshold satisfies the same eigenvalue problem as the linear stability threshold, and they must therefore be the same for steady RB convection.

When we perform a nonlinear stability analysis of time-modulated convection below, the general procedure detailed here will be the same, but there will be a few key differences. First, we will find that the linear and nonlinear stability eigenvalue problems are not the same and that the two thresholds do not coincide. Second, we will make use of a coupling parameter in the definition of the energy in order to improve the result. A coupling parameter is simply a factor multiplying one of the terms in the energy that can be tuned to achieve a better result. Third, the eigenvalue problem itself will be more complicated due to the time modulation.

3.4 Bounding

Stability analysis reveals only whether or not a flow will be stable, and the results do not necessarily give any information about what form the flow will take. Starting with only the setup (geometry, governing equations, and boundary conditions), we would often like to say something about what values various quantities of interest associated with the flow can take. To do this using the background method, we decompose the variables into a background part and a fluctuating part, where the background part meets the boundary conditions. Just as in the energy stability method, we use the governing equations to get power integrals for the evolution of the fluctuating parts, but now after combining the power integrals we use mathematical inequalities to find a bound on a flow quantity. In steady RB, a bound on the Nusselt number Nu is found, which compares the heat transport of convection to the heat transport in a state of pure conduction.

The governing equations are once again (3.1)–(3.3) with temperature boundary conditions (3.4). We take the velocity boundary conditions to be no-slip at the top and bottom. In the horizontal directions, we take both temperature and velocity to be periodic, though it is possible to relax this to no-slip, adiabatic conditions.

We decompose using the background flow technique by writing the temperature as

$$T(\boldsymbol{x},t)=\tau(z)+\theta(\boldsymbol{x},t), \tag{3.44}$$

where τ satisfies the boundary conditions on T so that

$$\tau(0)=1, \quad \tau(1)=0, \quad \theta(0,t)=0=\theta(1,t). \tag{3.45}$$

The next step is to form power integrals from the momentum and temperature equations and combine the results. The details are given in Chapter 7. The resulting differential equation is

$$\frac{1}{2}\frac{\mathrm{d}}{\mathrm{d}t}\left(\|\theta\|_2^2+\frac{\|\boldsymbol{u}\|_2^2}{\mathrm{RaPr}}\right)=-\frac{\|\nabla T\|_2^2}{2}+\frac{\|\partial_z\tau\|_2^2}{2}-\mathcal{H}[\theta,\tau,\boldsymbol{u}], \tag{3.46}$$

where we have defined the quadratic-form functional

$$\mathcal{H}[\theta,\tau,\boldsymbol{u}]\equiv\int_V\left(\frac{|\nabla\theta|^2}{2}+\frac{|\nabla\boldsymbol{u}|^2}{\mathrm{Ra}}+\theta w(\partial_z\tau-1)\right)\mathrm{d}V. \tag{3.47}$$

We now take a time average, denoted by the operator $\langle\cdot\rangle=T^{-1}\int_0^T(\cdot)\mathrm{d}t$, and assume the flow is statistically stationary so that the time average of the time derivative terms is zero. We also enforce

$$\mathcal{H}\geq 0, \tag{3.48}$$

which we call the spectral constraint. As a result, (3.46) turns into the inequality

$$\frac{\left\langle\|\nabla T\|_2^2\right\rangle}{A}\leq\int_0^1(\partial_z\tau)^2\mathrm{d}z, \tag{3.49}$$

where A is the nondimensional horizontal area. For steady RB, it is shown in section 7.8 that $\mathrm{Nu}=\langle\|\nabla T\|_2^2\rangle/A$, so that this represents a bound on the Nusselt number,

$$\mathrm{Nu}\leq\int_0^1(\partial_z\tau)^2\mathrm{d}z. \tag{3.50}$$

The remaining task is to choose τ so as to achieve the best possible bound while meeting the spectral constraint $\mathcal{H}\geq 0$. From (3.47), we see that choosing $\partial_z\tau=1$ would lead to $\mathcal{H}=0$, thereby satisfying the spectral constraint, but the resulting τ would not be able to meet both boundary conditions. As the next simplest option, we choose a linear piecewise profile such that $\partial_z\tau=1$ over most of the domain except for a small boundary layer near the bottom to meet the boundary condition there. In this section, we use only

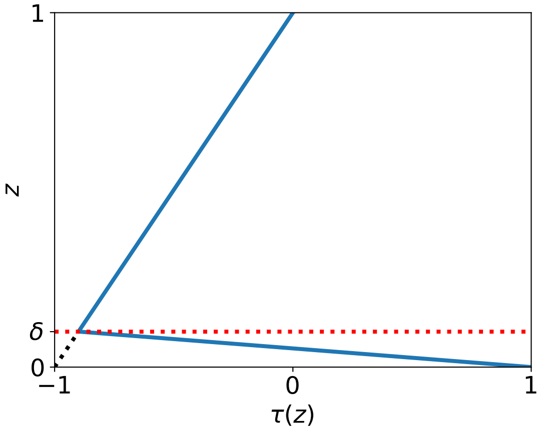

Figure 3.2: Background profile $\tau(z)$ with one boundary layer.

one boundary layer in the definition of τ, but improved results can be found with two boundary layers, as discussed in Chapter 7.

The linear piecewise profile for $\tau(z)$ is shown in Figure 3.2 and is

$$\tau(z) = \begin{cases} \left(\frac{\delta-2}{\delta}\right) z + 1 & 0 \leq z \leq \delta, \\ z - 1 & \delta < z \leq 1. \end{cases} \tag{3.51}$$

We must choose δ to meet the spectral constraint and give the best bound. Using the definition of τ from (3.51) in the definition of $\mathcal{H}$ from (3.47), along with the procedure discussed in Chapter 7 and the inequalities from section 7.6, we find that we must have

$$\delta \leq \frac{2\sqrt{2}}{\sqrt{\mathrm{Ra}}} \tag{3.52}$$

to meet the spectral constraint. The resulting bound on Nu from (3.50) is

$$\mathrm{Nu} \leq \frac{4}{\delta} - 3. \tag{3.53}$$

To achieve the lowest upper bound we must clearly make δ as large as possible. Using the maximum allowable value for δ from (3.52) leads to

$$\mathrm{Nu} \leq \sqrt{2}\sqrt{\mathrm{Ra}} - 3. \tag{3.54}$$

This shows that the bound on Nu scales with $\sqrt{\mathrm{Ra}}$. The constraint $\delta \leq 1$ leads to a constraint on the Rayleigh number, $\mathrm{Ra} \geq 8$. The prefactor $\sqrt{2}$ in the bound can be improved downwards by using another boundary layer and making slightly more clever rearrangements of the equations in the bounding process, as shown in Doering and Constantin (1996). The $\sqrt{\mathrm{Ra}}$ dependence remains the same even with the improved prefactors and appears to be the best possible scaling achievable with a linear piecewise background profile. In Chapter 7, with a time-modulated boundary temperature, we will follow the same general bounding procedure, but the bound will be more complicated to derive and interpret. For example, determining the optimum value of δ will not be as clear as in (3.53), but will instead require numerical optimization or asymptotic treatment. Furthermore, because of the time dependence, Nu and $\langle \|\nabla T\|_2^2 \rangle$ will not have a simple relationship, and the bound found will therefore be on $\langle \|\nabla T\|_2^2 \rangle$.

Chapter 4

Stability: Boundary Modulation

4.1 Introduction

The convection configuration considered in this paper has emerged from the study of radiatively-driven convection in ice-free Lake Superior. During springtime warming of this freshwater lake, observational data in Austin (2019) appears to show that an instability arises each day near the surface and carries heat through the entire water column on a time scale of hours. The temperature of the lake is between approximately 0°C and 4°C, which means the water is in the anomalous regime where increasing temperature serves to increase rather than decrease density.

The instability can be understood physically as follows. The water column begins the day at a uniform temperature throughout. As the sun comes up, radiative heating penetrates into the water column, with the heating concentrated near the surface and falling off exponentially with depth. Because the water is in the anomalous regime where temperature increase leads to density increase, heating at the surface increases the density of the water there. Buoyancy effects then cause the denser water to sink. If the buoyancy effects outweigh the restraining effects of heat diffusion and viscosity, an instability arises.

In many bodies of water, radiative heating penetrates into only a small fraction of the water column, and here we therefore treat the limit of radiative heating confined to a small layer near the surface, meaning that we specify a time-varying heat flux at one of the boundaries rather than including a radiative source term in the governing equations. The two infinite surfaces with heating imposed at one boundary makes this essentially a Rayleigh–Bénard (RB) configuration, but with an imposed flux that is modulated in time rather than an imposed steady temperature difference.

Most previous work has considered modulation on top of a background temperature gradient. Here we treat modulation with zero mean, meaning the average of the temperature difference between the top and bottom surfaces is zero. With zero-mean modulation, if the amplitude of the boundary heat-flux modulation is set to zero, nothing interesting happens as the water column is stably stratified from gravity and uniform in temperature. Only with a nonzero modulation amplitude is there a possibility for an unstable configuration.

The linear stability of modulated convection has been studied in earnest since at least Gershuni and Zhukhovitskii (1963), who looked at the low-frequency limit of modulated temperature gradient in standard Rayleigh-Bénard (RB) convection. Just as temperature boundary conditions were considered first in standard RB convection, temperature modulation was considered first for modulated RB convection. In particular, the combination of no-stress velocity conditions and fixed-temperature boundary conditions allows an analytical solution in terms of sine functions to be obtained, which was the approach taken in Venezian (1969), where the amplitude of modulation of the boundaries in standard RB was taken as a small parameter.

These were followed by a number of studies on the linear stability of modulated convection. Few authors, however, addressed zero-mean modulation, with the exception of Yih and Li (1972), Gershuni and Zhukhovitskii (1976), Or and Kelly (1999), and Souhar and

Aniss (2016). These authors investigated boundary temperature modulation, but no one appears to have addressed boundary heat-flux modulation. Davis (1976) reviewed stability (linear and nonlinear) of a variety of time-periodic flows, including thermal instabilities, but does not explicitly mention zero-mean modulated flow or heat flux modulation.

In addition to linear stability, we also examine nonlinear stability of modulated convection using the energy method. The first major work using the energy method to establish nonlinear stability in fluid dynamics appears to be Joseph (1976), though it was used before that by a variety of researchers, including Serrin (1959), who cited Reynolds and Orr as the progenitors. More recent textbooks covering the energy method include Doering and Gibbon (1995) and Straughan (2013). The work most relevant to our concerns is Homsy (1974), who investigated gravity modulation as well as modulation of the boundary temperatures.

To summarize the two approaches to determining stability, linear stability analysis establishes a sufficient condition for instability, in this case a Rayleigh number above which exponentially growing disturbances exist. Nonlinear stability analysis establishes a sufficient condition for stability, in this case a Rayleigh number below which the energy of all disturbances eventually decays. For asymptotic stability, the disturbance may grow during a cycle but overall experiences net decay, whereas for strong global stability the disturbance decays exponentially in time.

In the present paper, we consider convection in a layer of fluid that is infinite in the horizontal directions. We investigate zero-mean modulation of the heat flux at the bottom boundary, which, from the symmetry of the modulation profile, is equivalent to modulation at the top as would be the case for a lake. For comparison, we also give results for zero-mean modulation of the temperature at the bottom boundary, though we do not detail the derivation of the equations. While it is possible to treat modulated radiative heating, doing so would introduce additional parameters, and we therefore consider modulated heat flux at the boundary as the limit of radiative heating confined near the surface. After discussing the setup and governing equations, we go through the calculation of linear and nonlinear stability thresholds and present results.

At low frequencies, the physical relevance of the results may be limited as the period of the forcing becomes increasingly large. Numerically, the nonlinear stability results can be calculated without difficulty to very small frequencies, while the linear stability results become more difficult for frequencies of $O(1)$ and below.

In certain cases it is possible to make analytical arguments for what the critical Rayleigh numbers should be as $\omega \to 0$. It is possible to derive analytical results in this limit for strong global stability in all configurations and for asymptotic stability with symmetric no-stress boundary conditions and temperature modulation. For linear stability, the WKB approximation in Or (2001) can be used, but only for symmetric no-stress boundary conditions and temperature modulation.

4.2 Setup

We consider two parallel plates extending infinitely far in the x- and y-directions containing fluid satisfying the Boussinesq equations,

$$\partial_{t_*}\boldsymbol{u}_* + \boldsymbol{u}_* \cdot \nabla_* \boldsymbol{u}_* = -\frac{1}{\rho_0}\nabla_* p_* + \alpha g T_* \hat{\boldsymbol{z}} + \nu \nabla_*^2 \boldsymbol{u}_*, \tag{4.1}$$

$$\nabla_* \cdot \boldsymbol{u}_* = 0, \tag{4.2}$$

$$\partial_{t_*} T_* + \boldsymbol{u}_* \cdot \nabla_* T_* = \kappa \nabla_*^2 T_*, \tag{4.3}$$

where asterisks represent dimensional quantities; $\boldsymbol{u}_*$ is the velocity, T_* is the temperature measured with respect to the reference temperature at the upper boundary, ρ_0 is the density at the reference temperature, g is the acceleration due to gravity, ν is the kinematic viscosity, κ is the thermal diffusivity, α is the thermal expansion coefficient, and p_* is the pressure. The bottom boundary is at $z = 0$, and the top boundary is at $z = d$.

The velocity boundary conditions can be either no stress or no slip, and the temperature boundary conditions are

$$k\partial_z T_* = H\cos(\omega_* t_*) \quad \text{at} \quad z_* = 0, \tag{4.4}$$

$$T_* = 0 \quad \text{at} \quad z_* = d, \tag{4.5}$$

where d is the domain size in the z-direction, H is the amplitude of the modulated heat flux, and k is the conductivity. We nondimensionalize using

$$t \equiv \omega_* t_* \quad \boldsymbol{x} \equiv \frac{\boldsymbol{x}_*}{d}, \quad \boldsymbol{u} \equiv \frac{d\boldsymbol{u}_*}{\kappa}, \quad T \equiv \frac{kT_*}{Hd}, \tag{4.6}$$

and an appropriate scaling for pressure. We note that choosing to scale time by a diffusive time scale (e.g. d^2/κ) may be more appropriate in certain cases such as in the low frequency limit $\omega_* \to 0$.

Using the nondimensional variables in (4.6), the nondimensional governing equations become

$$\omega\partial_t \boldsymbol{u} + \boldsymbol{u}\cdot\nabla\boldsymbol{u} = -\nabla p + \mathrm{RaPr}T\hat{\boldsymbol{z}} + \mathrm{Pr}\nabla^2\boldsymbol{u}, \tag{4.7}$$

$$\nabla\cdot\boldsymbol{u} = 0, \tag{4.8}$$

$$\omega\partial_t T + \boldsymbol{u}\cdot\nabla T = \nabla^2 T. \tag{4.9}$$

The temperature boundary conditions become

$$\partial_z T = \cos t \quad \text{at} \quad z = 0, \tag{4.10}$$

$$T = 0 \quad \text{at} \quad z = 1. \tag{4.11}$$

The nondimensional frequency ω, Rayleigh number Ra, and Prandtl number Pr, are defined as

$$\omega \equiv \frac{\omega_* d^2}{\kappa}, \quad \mathrm{Ra} \equiv \frac{\alpha g H d^4}{k \nu \kappa}, \quad \mathrm{Pr} \equiv \frac{\nu}{\kappa}. \tag{4.12}$$

We write the base state velocity, temperature, and pressure as $\boldsymbol{u}_\mathrm{B}$, T_B, and p_B. For the stability analysis, we take a base state with no motion ($\boldsymbol{u}_\mathrm{B} = 0$) and a temperature profile satisfying equation (4.9) with the velocity set to zero, namely

$$\omega \partial_t T_\mathrm{B} = \nabla^2 T_\mathrm{B}, \tag{4.13}$$

and the boundary conditions (4.10) and (4.11). We write the solution for the base state temperature as

$$T_\mathrm{B}(z,t) = \mathrm{Re}\left\{ \frac{\mathrm{e}^{\mathrm{i}t}}{\beta} \left[\sinh(\beta z) - \frac{\sinh\beta \cosh(\beta z)}{\cosh\beta} \right] \right\}, \tag{4.14}$$

where $\beta = \sqrt{\mathrm{i}\omega}$.

4.3 Linear stability calculation

For linear stability, we consider small perturbations to the base state and write the independent variables as

$$\boldsymbol{u} = \boldsymbol{u}_{\mathrm{B}} + \boldsymbol{u}_{\mathrm{p}}, \quad T = T_{\mathrm{B}} + \theta_{\mathrm{p}}, \quad p = p_{\mathrm{B}} + P. \tag{4.15}$$

Using these in the governing equations (4.7) and (4.8), neglecting products of perturbations, and isolating the vertical velocity component ($\boldsymbol{e}_z \cdot \boldsymbol{u}_{\mathrm{p}} = w_{\mathrm{p}}$) results in

$$\left(\omega\partial_t\nabla^2 - \mathrm{Pr}\nabla^4\right) w_{\mathrm{p}}(\boldsymbol{x},t) = \mathrm{RaPr}\nabla^2_{\mathrm{H}}\theta_{\mathrm{p}}(\boldsymbol{x},t), \tag{4.16}$$

$$\left(\omega\partial_t - \nabla^2\right)\theta_{\mathrm{p}}(\boldsymbol{x},t) = -(\partial_z T_{\mathrm{B}}) w_{\mathrm{p}}(\boldsymbol{x},t), \tag{4.17}$$

where $\nabla^2_{\mathrm{H}} = \partial_x^2 + \partial_y^2$. The governing equations have constant coefficients in space, and therefore the horizontal spatial components of the functions can be analyzed using normal modes, so that we can write the perturbations as

$$w_{\mathrm{p}}(\boldsymbol{x},t) = \mathrm{e}^{\mathrm{i}k_x x}\mathrm{e}^{\mathrm{i}k_y y} w(z,t), \tag{4.18}$$

$$\theta_{\mathrm{p}}(\boldsymbol{x},t) = \mathrm{e}^{\mathrm{i}k_x x}\mathrm{e}^{\mathrm{i}k_y y}\theta(z,t). \tag{4.19}$$

The resulting equations are

$$\left(\omega\partial_t L - \mathrm{Pr}L^2\right) w(z,t) = -k^2\mathrm{RaPr}\theta(z,t), \tag{4.20}$$

$$\left(\omega\partial_t - L\right)\theta(z,t) = -(\partial_z T_{\mathrm{B}}) w(z,t), \tag{4.21}$$

where $k^2 \equiv k_x^2 + k_y^2$ and $L \equiv (\partial_z^2 - k^2)$.

To remove the z dependence, we use Chebyshev polynomials. One possibility is to use Chebyshev differentiation matrices, as discussed in Weideman and Reddy (2000) and Trefethen (2000), so that w and θ are solved for at specific grid points. Another possibility is to express w and θ as Chebyshev polynomials and then use collocation or Galerkin projection to remove the z dependence so that the coefficients in the Chebyshev expansion of w and θ become the relevant unknowns, which is the approach taken in Or and Kelly (1999). The boundary conditions must be satisfied in each case. For details on the numerical methods used, see 4.8.

In all cases, the resulting matrix equation can be written as

$$\begin{pmatrix} \boldsymbol{A} & \boldsymbol{0} \\ \boldsymbol{0} & \boldsymbol{E} \end{pmatrix} \frac{\mathrm{d}}{\mathrm{d}t} \begin{pmatrix} \boldsymbol{w} \\ \boldsymbol{\theta} \end{pmatrix} = \left[\begin{pmatrix} \boldsymbol{B} & \boldsymbol{0} \\ \boldsymbol{0} & \boldsymbol{F} \end{pmatrix} + \mathrm{Ra} \begin{pmatrix} \boldsymbol{0} & \boldsymbol{C} \\ \boldsymbol{0} & \boldsymbol{0} \end{pmatrix} + \begin{pmatrix} \boldsymbol{0} & \boldsymbol{0} \\ \boldsymbol{G}_1 & \boldsymbol{0} \end{pmatrix} \mathrm{e}^{\mathrm{i}t} + \begin{pmatrix} \boldsymbol{0} & \boldsymbol{0} \\ \boldsymbol{G}_{-1} & \boldsymbol{0} \end{pmatrix} \mathrm{e}^{-\mathrm{i}t} \right] \begin{pmatrix} \boldsymbol{w} \\ \boldsymbol{\theta} \end{pmatrix}, \tag{4.22}$$

where $\boldsymbol{w}$ and $\boldsymbol{\theta}$ are vectors of coefficients or of the solutions at chosen grid points, depending on the method chosen. The base state gradient is expressed as $\partial_z T_{\mathrm{B}} = T_1(z)\mathrm{e}^{\mathrm{i}t} + T_{-1}(z)\mathrm{e}^{-\mathrm{i}t}$ and discretized using the same method as the solutions. By defining

$$\boldsymbol{x} = \begin{pmatrix} \boldsymbol{w} \\ \boldsymbol{\theta} \end{pmatrix}, \tag{4.23}$$

we can write (4.22) as

$$\boldsymbol{H}_d \frac{\mathrm{d}\boldsymbol{x}}{\mathrm{d}t} = \left[\boldsymbol{H}_0 + \mathrm{Ra}\boldsymbol{H}_R + \boldsymbol{H}_1 \mathrm{e}^{\mathrm{i}t} + \boldsymbol{H}_{-1}\mathrm{e}^{-\mathrm{i}t} \right] \boldsymbol{x}. \tag{4.24}$$

The system of ordinary differential equations represented by equation (4.24) has coefficients that are periodic in time, and we therefore use Floquet theory. There are two ways we can use Floquet theory, which we will call the Floquet–Fourier–Hill (FFH) and monodromy matrix methods. The FFH method requires solving an eigenvalue problem, while the monodromy matrix method requires solving a system of ODEs. Here we use the FFH method because it is computationally more efficient. The FFH and monodromy matrix methods both fail to reach converged solutions at low enough frequencies, and we therefore report results only for frequencies high enough so that the results are converged and validated. For details on the FFH method, see Deconinck and Kutz (2006).

4.3.1 Floquet–Fourier–Hill method

For the FFH method, we use Floquet theory to decompose $\boldsymbol{w}(t)$ and $\boldsymbol{\theta}(t)$ into an exponential function of time multiplying a function that is periodic in time with the same period as the coefficients, namely 2π. The solution vector is then

$$\boldsymbol{x}(t) = \mathrm{e}^{\mu t} \sum_{n=-\infty}^{\infty} \boldsymbol{x}_n \mathrm{e}^{\mathrm{i}nt}, \tag{4.25}$$

where μ is the Floquet exponent. Using this representation in (4.24) leads to

$$\sum_{n=-\infty}^{\infty} \boldsymbol{H}_d(\mathrm{i}n + \mu)\boldsymbol{x}_n \mathrm{e}^{\mathrm{i}nt} = \sum_{n=-\infty}^{\infty} \left[\boldsymbol{H}_0\boldsymbol{x}_n + \mathrm{Ra}\boldsymbol{H}_R\boldsymbol{x}_n + \boldsymbol{H}_1\boldsymbol{x}_{n-1} + \boldsymbol{H}_{-1}\boldsymbol{x}_{n+1}\right] \mathrm{e}^{\mathrm{i}nt}. \tag{4.26}$$

Orthogonality of the exponential functions leads to

$$\boldsymbol{H}_d(\mathrm{i}n + \mu)\boldsymbol{x}_n = \boldsymbol{H}_0\boldsymbol{x}_n + \mathrm{Ra}\boldsymbol{H}_R\boldsymbol{x}_n + \boldsymbol{H}_1\boldsymbol{x}_{n-1} + \boldsymbol{H}_{-1}\boldsymbol{x}_{n+1}, \tag{4.27}$$

which is an infinite system of coupled equations for the Fourier coefficients and can be treated as an eigenvalue problem for Ra or μ. We solve this coupled set numerically by truncating the Fourier series and solving the resulting generalized eigenvalue problem, which is block tridiagonal on one side and block diagonal on the other.

The eigenvalue problem depends on Pr, ω, k, Ra, μ, the number of Fourier modes, the number of Chebyshev modes or grid points, and the boundary conditions. Once other parameters are fixed, either the Rayleigh number, Ra, or the Floquet exponent, μ, can be considered as the eigenvalue. The critical Rayleigh number for a given Pr and ω is the lowest Rayleigh number found through varying k that results in $\mu_{\text{real}} = 0$.

If the Rayleigh number is treated as the eigenvalue, then we fix $\mu_{\text{real}} = 0$ to look for marginal stability If we write $\mu = \mu_0 + \mathrm{i}m$ in (4.25), with $0 \leq \mathrm{Im}(\mu_0) \leq 1$ and m a positive integer, we find

$$\boldsymbol{x}(t) = \mathrm{e}^{\mu_0 t} \sum_{n=-\infty}^{\infty} \boldsymbol{x}_n \mathrm{e}^{\mathrm{i}(n+m)t}, \tag{4.28}$$

We see that m serves only to shift the association between the coefficient index and the frequency of the exponential it accompanies, and we can therefore restrict $\mathrm{Im}(\mu)$ to be between zero and one without loss of generality. The lowest Rayleigh number found over all wavenumbers is the critical Rayleigh number. If instead the Floquet exponent μ is chosen as the eigenvalue, then k and Ra must be swept through to find the minimum value of Ra resulting in $\mu_{\text{real}} = 0$.

For our numerical results, we have generally found the critical Rayleigh number by treating Ra as the eigenvalue. We have then checked the resulting critical Rayleigh number and wavenumber by using these values and treating μ as the eigenvalue to ensure μ_{real} is truly close enough to zero to represent the stability threshold. Furthermore, we have checked the surrounding (k, Ra) parameter space to be sure that the critical Rayleigh number found is truly a local minimum leading to marginal stability.

We have generally used 18 Chebyshev grid points. The highest Fourier mode used when solving for Ra as the eigenvalue varied between 15 and 30, depending on the frequency, with more Fourier modes being necessary to reach a converged solution at lower frequencies. When solving for μ as the eigenvalue, it is possible to use sparse eigenvalue, and we have therefore been able to use a largest Fourier mode of 35 to 50.

4.3.2 Low-frequency limit

At a certain $O(1)$ value of ω, the eigenvalue problem resulting from the FFH method becomes too ill conditioned to continue working. For small ω, the leading order of the z-derivative of the base state in (4.14) becomes independent of space and can be written as

$$\partial_z T_{\mathrm{B}} = \cos t + O(\omega). \tag{4.29}$$

This coincides with what we expect physically since for very slow modulation, the temperature profile will be almost linear, and the slope will be that imposed at the boundary, namely $\cos t$. With the spatial dependence eliminated, we can compare the eigenvalue problems for stability in the modulated case to the eigenvalue problems for stability in the steady case with boundaries held at different temperatures, which has a nondimensional temperature profile slope of negative one.

For temperature modulation with no-stress boundary conditions, the governing equations reduce to a Mathieu equation in this limit, and a WKB analysis can be done, as discussed in Or (2001). For all other cases, a similar approach leads to a system of coupled Mathieu equations, which can formally be solved with an extension of the WKB ansatz to systems of equations. Unfortunately, connecting the WKB solutions through turning points is much more difficult with higher-order systems of equations than it is for the standard second-order ODE. Mathematical details are discussed in Wasow (1985), but there does not appear to be a simple way to use the WKB approach for the cases considered here.

4.4 Nonlinear stability calculation

To determine the threshold for nonlinear stability, we use the energy method and two notions of nonlinear stability: strong global stability and asymptotic stability, as used and described in Homsy (1974) for nonzero-mean temperature modulation. The analysis in Homsy (1974) uses the mean of the boundary temperature difference as the temperature scale, which is not possible for zero-mean modulation, and the base state is different, but otherwise the approach is similar. We therefore give only the essentials and refer the reader to Homsy (1974), Joseph (1976), or Straughan (2013) for more details.

The first step is to form an energy functional using power integrals. The first integral comes from taking the dot product of (4.7) with $\boldsymbol{u}$ and integrating over the volume. The second integral comes from writing the temperature as the base state plus a fluctuation of arbitrary size, $T(\boldsymbol{x},t) = T_{\mathrm{B}}(z,t) + \theta(\boldsymbol{x},t)$, using this expression in (4.9), and then multiplying by θ and integrating over the volume. Finally, we multiply the temperature integral by $\lambda\mathrm{Ra}$ and add the result to the momentum integral, where λ is a coupling parameter that we can later tune to achieve better stability results. The resulting equation for the time evolution of the energy is

$$\omega \frac{\mathrm{d}}{\mathrm{d}t}\left(\frac{\|\boldsymbol{u}\|_2^2}{2\mathrm{Pr}} + \frac{\|\phi\|_2^2}{2}\right) = \frac{R}{\sqrt{\lambda}} \int_V w\phi\left(1 - \lambda\partial_z T_{\mathrm{B}}\right)\mathrm{d}V - \left(\|\nabla\boldsymbol{u}\|_2^2 + \|\nabla\phi\|_2^2\right), \tag{4.30}$$

where $R = \sqrt{\mathrm{Ra}}$, $\phi = \theta\sqrt{\lambda\mathrm{Ra}}$, and the norms are

$$\|\phi\|_2^2 = \int_V \phi^2 \mathrm{d}V, \quad \|\nabla\phi\|_2^2 = \int_V |\nabla\phi|^2 \mathrm{d}V, \quad \|\nabla\boldsymbol{u}\|_2^2 = \int_V \frac{\partial u_j}{\partial x_k}\frac{\partial u_j}{\partial x_k}\mathrm{d}V. \tag{4.31}$$

We now define

$$E = \left(\frac{\|\boldsymbol{u}\|_2^2}{2\mathrm{Pr}} + \frac{\|\phi\|_2^2}{2}\right), \quad I_\lambda = \lambda^{-1/2}\int_V w\phi\left(1 - \lambda\partial_z T_{\mathrm{B}}\right)\mathrm{d}V, \quad D = \left(\|\nabla\boldsymbol{u}\|_2^2 + \|\nabla\phi\|_2^2\right), \tag{4.32}$$

so that we have

$$\omega\frac{\mathrm{d}E}{\mathrm{d}t} = RI_\lambda - D. \tag{4.33}$$

From (4.33) we develop strong global stability and asymptotic stability.

4.4.1 Strong global stability

For strong global stability, we divide both sides of (4.33) by D to find

$$\omega \frac{E'(t)}{D} = R\frac{I_\lambda}{D} - 1 \leq R \max_{\mathcal{H}} \left(\frac{I_\lambda}{D}\right) - 1. \tag{4.34}$$

We define

$$\frac{1}{\rho_\lambda(t)} \equiv \max_{\mathcal{H}} \left(\frac{I_\lambda}{D}\right), \tag{4.35}$$

where $\mathcal{H}$ is the space of divergence-free functions satisfying the boundary conditions and $\rho_\lambda(t)$ is periodic with the same period as the base state temperature gradient. We then define

$$R_{S,\lambda} \equiv \min_{t\in[0,2\pi]} \rho_\lambda \tag{4.36}$$

to arrive at

$$E'(t) \leq -\frac{D}{\omega}\left(\frac{R_{S,\lambda} - R}{R_{S,\lambda}}\right). \tag{4.37}$$

From Poincaré's inequality, we have $D \geq \alpha_1 E$, with $\alpha_1 \geq 0$. We therefore have

$$E(t) \leq E(0) \exp\left(-\frac{\alpha_1 t(R_{S,\lambda} - R)}{\omega R_{S,\lambda}}\right). \tag{4.38}$$

For $R < R_{S,\lambda}$, the energy decays exponentially in time, which we call strong global stability.

To find $R_{S,\lambda}$, we must first solve the variational problem for $\rho_\lambda(t)$ in (4.35), which upon using variational calculus with a Lagrange multiplier for the incompressibility constraint leads to

$$\frac{\rho_\lambda(t)}{2\sqrt{\lambda}}\left(1-\lambda\partial_z T_{\mathrm{B}}\right)\nabla_H^2\phi+\nabla^4 w=0, \tag{4.39}$$

$$\frac{\rho_\lambda(t)}{2\sqrt{\lambda}}\left(1-\lambda\partial_z T_{\mathrm{B}}\right)w+\nabla^2\phi=0. \tag{4.40}$$

We use normal modes and write

$$(w(\boldsymbol{x},t),\phi(\boldsymbol{x},t))=(W(z,t),\Phi(z,t))\mathrm{e}^{\mathrm{i}k_x x}\mathrm{e}^{\mathrm{i}k_y y}. \tag{4.41}$$

The equations then become

$$L^2 W(z,t)=\frac{k^2\rho_\lambda(t)}{2\sqrt{\lambda}}\left(1-\lambda\partial_z T_{\mathrm{B}}\right)\Phi(z,t) \tag{4.42}$$

$$L\Phi(z,t)=-\frac{\rho_\lambda(t)}{2\sqrt{\lambda}}\left(1-\partial_z T_{\mathrm{B}}\right)W(z,t). \tag{4.43}$$

This is a generalized eigenvalue problem for $\rho_\lambda(t)$, which can be written as

$$\begin{pmatrix} L^2 & 0 \\ 0 & L \end{pmatrix}\begin{pmatrix} W \\ \Phi \end{pmatrix}=\rho_\lambda(t)\left(\frac{1-\lambda\partial_z T_{\mathrm{B}}}{2\sqrt{\lambda}}\right)\begin{pmatrix} 0 & k^2 \\ -1 & 0 \end{pmatrix}\begin{pmatrix} W \\ \Phi \end{pmatrix}. \tag{4.44}$$

We solve this generalized eigenvalue problem by discretizing on a Chebyshev basis (as discussed in the linear stability section). To find $R_{S,\lambda}$, we then minimize $\rho_\lambda(t)$ over time as specified in (4.36). Finally, we vary λ to find the best stability result, namely the highest $R_{S,\lambda}$, which we define as the threshold for strong global stability, R_S. Altogether this is

$$R_S=\max_\lambda\min_k\min_t\rho_\lambda(t;k). \tag{4.45}$$

Low-frequency limit

For strong global stability, as $\omega \to 0$ the eigenvalue problem from (4.39) and (4.40) becomes

$$\frac{\rho_\lambda(t)}{2\sqrt{\lambda}}\left(1-\lambda\cos t\right)\nabla_H^2\phi+\nabla^4 w=0, \tag{4.46}$$

$$\frac{\rho_\lambda(t)}{2\sqrt{\lambda}}\left(1-\lambda\cos t\right)w+\nabla^2\phi=0. \tag{4.47}$$

The eigenvalue problem for the linear stability threshold in standard RB can be written as

$$R\nabla_H^2\theta+\nabla^4 w=0, \tag{4.48}$$

$$Rw+\nabla^2\theta=0, \tag{4.49}$$

The spatial operators in the two cases are equivalent, and so $\rho_\lambda(t)$ must satisfy

$$\frac{\rho_\lambda(t)}{2\sqrt{\lambda}}\left(1+\lambda\cos\left(t\right)\right)\in\{R_{j,\mathrm{steady}}\}, \tag{4.50}$$

where each $R_{j,\mathrm{steady}}$ satisfies the eigenvalue problem in (4.48) and (4.49). Rearranging, we have

$$\rho_\lambda(t)=\frac{2\sqrt{\lambda}}{1+\lambda\cos\left(t\right)}R_{j,\mathrm{steady}} \tag{4.51}$$

for each possible j. Now we use normal modes and perform $R_S=\max_\lambda\min_k\min_t\rho_\lambda(t;k)$. Minimizing in time clearly means we must take $\cos t=1$. We are then left to maximize over λ, which leads to $\lambda=1$. Finally, we minimize the resulting $\rho_\lambda(t;k)$ over k, which leads to $R_S=\min_k\{R_{j,\mathrm{steady}}\}$. Because $\mathrm{Ra}_{L,\mathrm{steady}}\equiv\min_k\{R_{j,\mathrm{steady}}\}$, we conclude that $\mathrm{Ra}_S\to\mathrm{Ra}_{L,\mathrm{steady}}$ as $\omega\to 0$. This is the limit approached by the numerical results, as seen in figures 4.1 and 4.4 for modulated flux and temperature, respectively.

4.4.2 Asymptotic stability

For asymptotic stability, we start from (4.33) and write

$$E'(t) = \left(\frac{RI_\lambda(t) - D}{\omega E(t)}\right) E(t). \tag{4.52}$$

First we define

$$\nu_\lambda(t) \equiv \max_{\mathcal{H}} \left(\frac{RI_\lambda(t) - D}{\omega E(t)}\right), \tag{4.53}$$

where $\mathcal{H}$ is the space of divergence-free functions satisfying the boundary conditions. This leads to

$$E'(t) \leq \nu_\lambda(t) E(t), \tag{4.54}$$

which means that

$$E(t) \leq \exp\left(\int_0^t \nu_\lambda(t')\mathrm{d}t'\right) E(0). \tag{4.55}$$

Variational calculus with a Lagrange multiplier for incompressibility leads to

$$\frac{R}{2\sqrt{\lambda}}(1 - \lambda\partial_z T_\mathrm{B})\nabla_H^2\phi + \nabla^4 w = \frac{\nu_\lambda}{2\mathrm{Pr}}\nabla^2 w, \tag{4.56}$$

$$\frac{R}{2\sqrt{\lambda}}(1 - \lambda\partial_z T_\mathrm{B})w + \nabla^2\phi = \frac{\nu_\lambda}{2}\phi. \tag{4.57}$$

The eigenvalue $\nu_\lambda(t)$ is periodic, and we define the configuration as asymptotically stable if the integral of ν_λ over one period is less than zero, defining

$$\bar{\nu}_\lambda \equiv \int_0^{2\pi} \nu_\lambda(t)\mathrm{d}t. \tag{4.58}$$

We use normal modes as in (4.41) and find the generalized eigenvalue problem

$$\begin{pmatrix} L^2 & \frac{-k^2 R}{2\sqrt{\lambda}}\left(1-\lambda\partial_z T_{\mathrm{B}}\right) \\ \frac{R}{2\sqrt{\lambda}}\left(1-\lambda\partial_z T_{\mathrm{B}}\right) & L \end{pmatrix} \begin{pmatrix} W \\ \Phi \end{pmatrix} = \nu_\lambda(t) \begin{pmatrix} \mathrm{Pr}^{-1}L/2 & 0 \\ 0 & 1/2 \end{pmatrix} \begin{pmatrix} W \\ \Phi \end{pmatrix}. \quad (4.59)$$

We then discretize in z using a Chebyshev basis and solve this generalized eigenvalue problem numerically in order to estimate $\bar{\nu}_\lambda$, the integral of $\nu_\lambda(t)$ over one period. For fixed Ra, Pr, and ω, we first sweep through wavenumbers and take the worst case (largest) value for $\nu_\lambda(t)$ at the chosen points in time over one period, which upon integrating in time gives us $\bar{\nu}_\lambda$. For efficiency, we have used Gauss quadrature with 30 grid points for the integral. Checks using more advanced integration methods indicate a relative error in the resulting Rayleigh number of well below one percent when using Gauss quadrature with 30 grid points. We then vary λ to minimize this integral, and we define the result as

$$\bar{\nu} \equiv \min_{\lambda} \max_{k} \bar{\nu}_\lambda. \quad (4.60)$$

Finally, we find the largest R satisfying $\bar{\nu} < 0$ and define it as R_A, so that

$$R_A \equiv \max R \quad \text{s.t.} \quad \bar{\nu} < 0. \quad (4.61)$$

Low-frequency-limit

For heat-flux modulation, we have not found any simplification to be possible in the low-frequency limit for asymptotic stability, and we therefore discuss temperature modulation with symmetric no-stress boundary conditions in this section. In this case, sine functions may be used as eigenfunctions as in standard RB, and the z derivative of the base state is $\partial_z T_{\mathrm{B}} \approx -\cos t$.

In (4.59), we use

$$W(z,t)=\sum_{n=0}^{\infty}w_n(t)\sin n\pi z,\quad \Phi(z,t)=\sum_{n=0}^{\infty}\phi_n(t)\sin n\pi z. \tag{4.62}$$

to arrive at a quadratic equation for $\nu_\lambda(t)$,

$$\nu_\lambda^2-2\lambda_n(1+\mathrm{Pr})\nu_\lambda+\frac{4\mathrm{Pr}}{\lambda_n}\left(\lambda_n^3+k^2g(\lambda)^2R^2\right)=0, \tag{4.63}$$

where $\lambda_n=-(k^2+n^2\pi^2)$ and $g(\lambda)=(1-\lambda\partial_zT_{\mathrm{B}})/(2\sqrt{\lambda})$.

To find the stability threshold, we solve the quadratic, set the resulting $\bar{\nu}_\lambda$ equal to zero, and find

$$\mathrm{Ra}_A\leq\mathrm{Ra}_{L,\mathrm{steady}}\left(\frac{2\pi\sqrt{\lambda}}{2\cos^{-1}\left(-1/\lambda\right)-\pi+2\lambda\sin\left(\cos^{-1}\left(-1/\lambda\right)\right)}\right)^2, \tag{4.64}$$

with $k_{\mathrm{cr}}=\pi/\sqrt{2}$, the critical wavenumber in steady RB with the same boundary conditions. The λ leading to the largest Ra_A is $\lambda\approx1.319$, leading to $\mathrm{Ra}_A\approx2891.38$, which is exactly what we find numerically, as seen in figure 4.4.

4.5 Results

4.5.1 Heat flux modulation

Carrying out the linear and nonlinear stability calculations as described in the preceding sections, we are able to find results for linear stability, asymptotic stability, and strong global stability for specified ω, Pr, and boundary conditions. Results for no-slip conditions on the top and bottom are shown on the left side in figure 4.1, while no-stress conditions are shown on the right side of the same figure. As usual in Rayleigh–Bénard

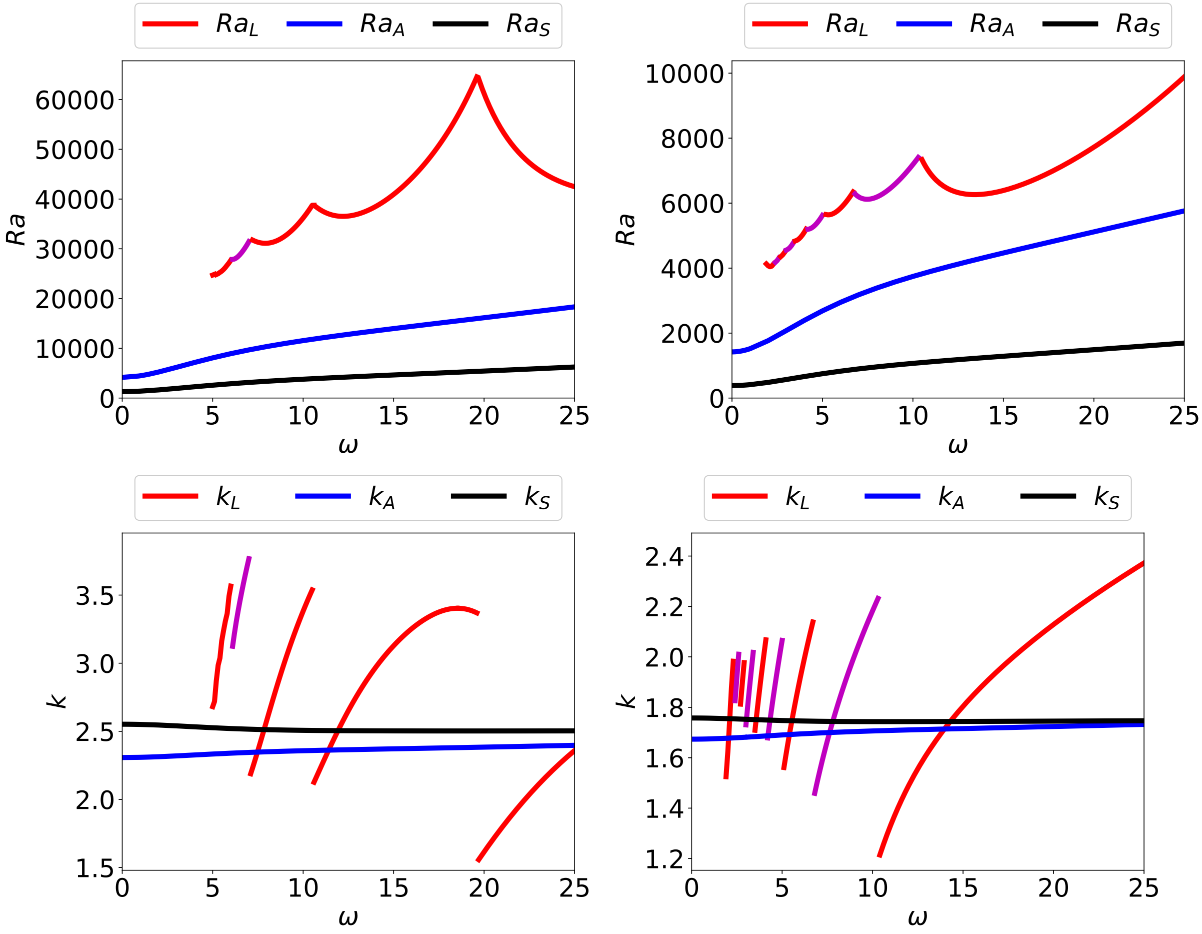

Figure 4.1: Critical Rayleigh numbers and wavenumbers for heat flux modulation. Left: no-slip; Right: no-stress. $\mathrm{Pr} = 1$. For Ra_L, magenta indicates a synchronous disturbance and red indicates a subharmonic disturbance. Linear stability results at low frequencies are absent because the numerical problem becomes ill conditioned.

convection, no-slip conditions lead to a higher critical Rayleigh number.

For linear stability, we find that the critical Rayleigh number always arises from either $\mu_{\text{imag}} = 0$ or $\mu_{\text{imag}} = 1/2$, representing synchronous and subharmonic disturbances, respectively. There is a stark contrast between low and high frequencies. At low frequencies, Ra_L generally decreases with ω, but in an oscillatory manner as the critical instability switches between a synchronous and subharmonic disturbance. At high frequencies, the critical instability is always subharmonic, and an asymptotic balance is

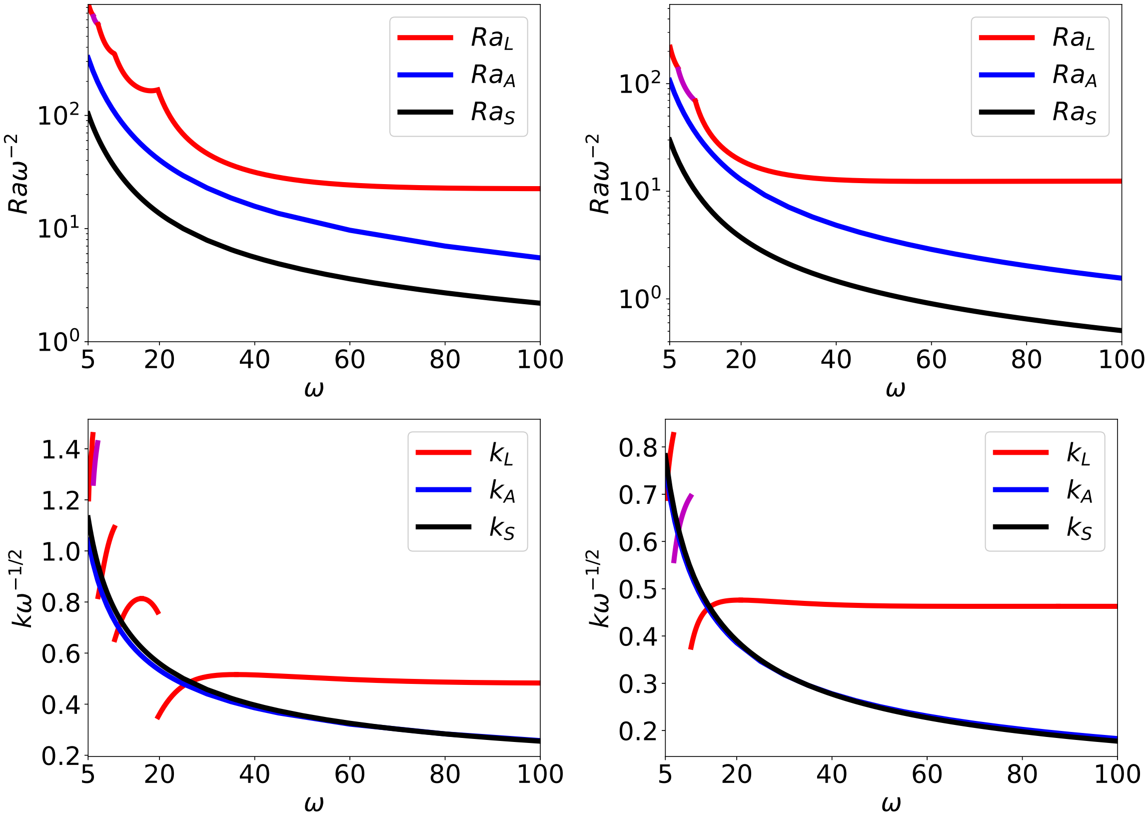

Figure 4.2: Critical Rayleigh numbers and wavenumbers for heat flux modulation scaled for high ω. Left: no-slip; Right: no-stress. $\mathrm{Pr} = 1$. For Ra_L, magenta indicates a synchronous disturbance and red indicates a subharmonic disturbance.

reached with $\mathrm{Ra}_L\omega^{-2}$ approaching a nonzero constant, as shown in figure 4.2. For linear stability, no-slip conditions with $\mathrm{Pr} = 1$ lead to $\mathrm{Ra}_L\omega^{-2} \to 22.58$, while no-stress conditions lead to $\mathrm{Ra}_L\omega^{-2} \to 12.44$. The nonlinear stability thresholds do not appear to reach the same asymptotic relationship between the critical Rayleigh number and the modulation frequency. The nonlinear stability results do not change as radically with frequency as the linear stability results overall, though the threshold for both asymptotic stability and strong global stability does go down at low frequencies.

A lower Prandtl number generally leads to a higher linear stability threshold. A rationale for this is that decreasing the Prandtl number means increasing the thermal diffusivity relative to the momentum diffusivity, thereby allowing heat to escape more easily and hence requiring a greater strength of heating to create an instability. It is somewhat surprising then to find that Ra_A reaches a maximum near $\mathrm{Pr} = 0.6$ and then decreases with decreasing Pr for $\omega = 100$ and no-stress boundary conditions, with a similar result for no-slip conditions. Calculations for $\omega = 10$ show the same pattern of behavior.

The dependence of the critical Rayleigh number on Pr is shown in figure 4.3, where it can be seen that Ra_L changes by orders of magnitude as Pr is varied while Ra_A stays in a relatively narrow range. In contrast, strong global stability is independent of the Prandtl number. A subcritical instability is an instability arising for a Ra between the linear and nonlinear stability thresholds. There is therefore a very large region for potential subcritical instabilities at low Pr, with the region increasing as Pr decreases, as seen in figure 4.3.

4.5.2 Temperature modulation

Linear stability results for nonzero-mean temperature modulation of one boundary can be found in Or and Kelly (1999). For completeness, we include here nonlinear stability results for that same setup. These results are shown in figure 4.4. The general dependence

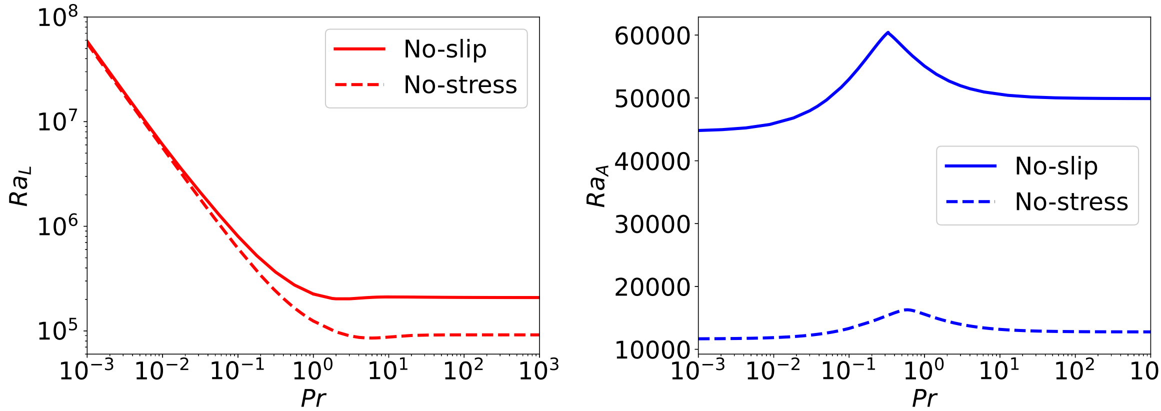

Figure 4.3: Dependence of Ra_L and Ra_A on Pr for $\omega = 100$ with symmetric no-slip and no-stress conditions and heat flux modulation.

of the critical Rayleigh number is the same as in the modulated flux case, and only the specific numbers are different.

The no-stress case can be treated with sine eigenfunctions, meaning the stability problem reduces to a single ODE. It is also possible to use the WKB approximation for this case, as in Or (2001), but we do not pursue further WKB calculations here for the reasons discussed in section 4.3.2.

Results scaled for large ω are shown in figure 4.5. As $\omega \to \infty$, the appropriately defined Rayleigh number grows with $\omega^{3/2}$. For linear stability, no-slip conditions with $\mathrm{Pr} = 1$ lead to $\mathrm{Ra}_L \omega^{-3/2} \to 27.86$, while no-stress conditions lead to $\mathrm{Ra}_L \omega^{-3/2} \to 18.38$. The nonlinear stability thresholds do not appear to reach the same asymptotic relationship between the critical Rayleigh number and the modulation frequency.

4.5.3 High frequency

In this section we look at high-frequency results for all configurations to compare the behavior of the linear and global stability thresholds. Though we have explicitly treated only the zero-temperature top boundary condition listed in (4.11), it is of course possible to use a no-flux top boundary condition. As the modulation frequency is increased, the base

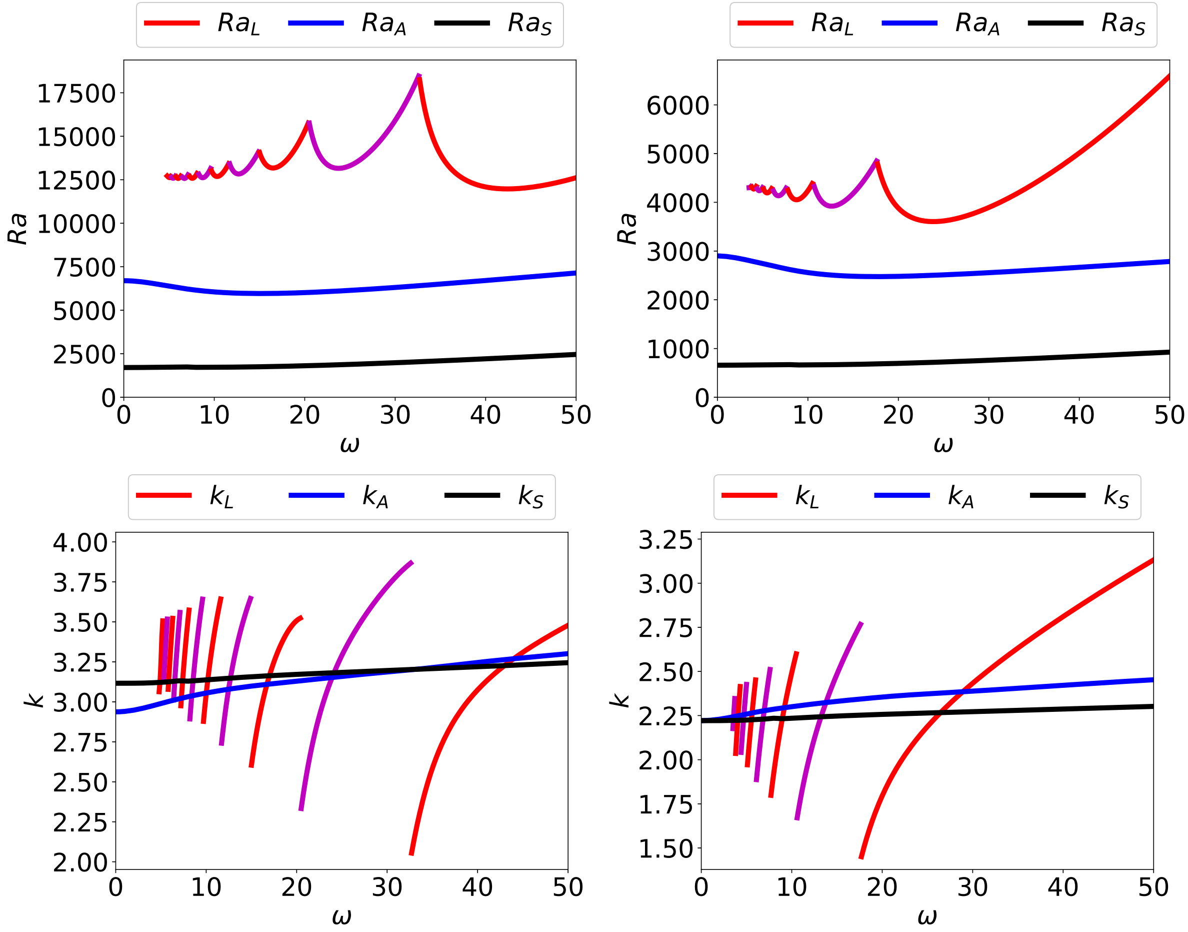

Figure 4.4: Temperature modulation results with Pr = 1. Left: no-slip; Right: no-stress.

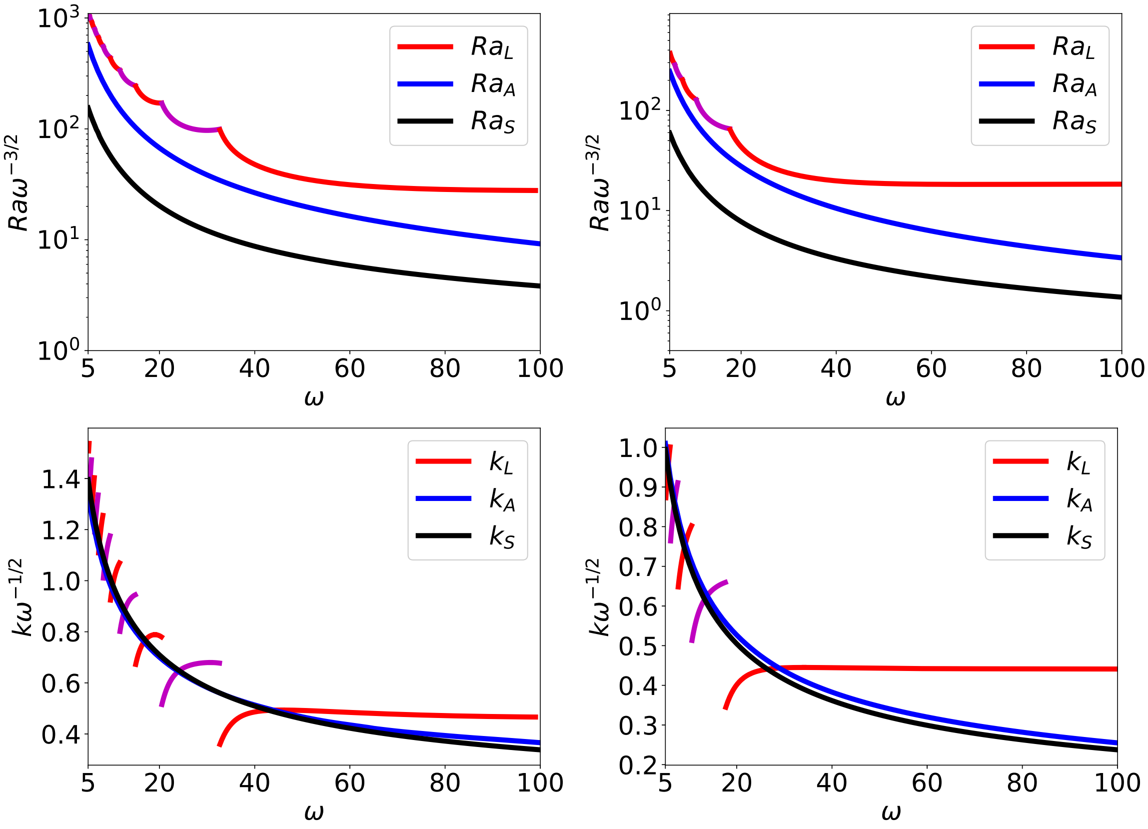

Figure 4.5: Temperature modulation results scaled for high ω with $\mathrm{Pr} = 1$. Left: no-slip; Right: no-stress. For Ra_L, magenta indicates a synchronous disturbance and red indicates a subharmonic disturbance.

state temperature profile becomes largely confined to a small layer near the modulated surface at the bottom. For large ω, the base state for heat-flux modulation in (4.14) leads to the following form for the base state derivative,

$$\partial_z T_{\mathrm{B}}(z,t) \approx \mathrm{e}^{-z\sqrt{\omega/2}} \cos\left(t - z\sqrt{\frac{\omega}{2}}\right). \tag{4.65}$$

The boundary layer thickness is therefore $O(\omega^{-1/2})$, so that for large enough ω we might expect the same results even with different boundary conditions imposed at the top at $z = 1$ because the base state derivative has hardly any influence there.

For linear stability, the top boundary conditions do not matter for large ω. Figure 4.6 shows the critical Rayleigh numbers for all possible configurations, demonstrating that by $\omega = 100$, the boundary conditions at the non-modulated surface have ceased to affect the critical Rayleigh number, which for $\omega \gtrapprox 100$ is essentially dependent only on the conditions at the modulated surface. For all frequencies shown in figure 4.6, the critical disturbance is subharmonic. The scaled Rayleigh number used in the figure is defined as

$$\mathrm{Ra}_\infty = \begin{cases} \mathrm{Ra}\,\omega^{-3/2} & \text{temperature modulation} \\ \mathrm{Ra}\,\omega^{-2} & \text{heat-flux modulation.} \end{cases} \tag{4.66}$$

In contrast, for nonlinear stability the bottom boundary condition does affect the critical Rayleigh number even at high frequencies. Figure 4.6 shows that results for the four possible top boundary conditions do not converge at high frequency as they do in linear stability. Asymptotic stability results indicate the same pattern, with the top boundary conditions influencing results even at higher frequencies.

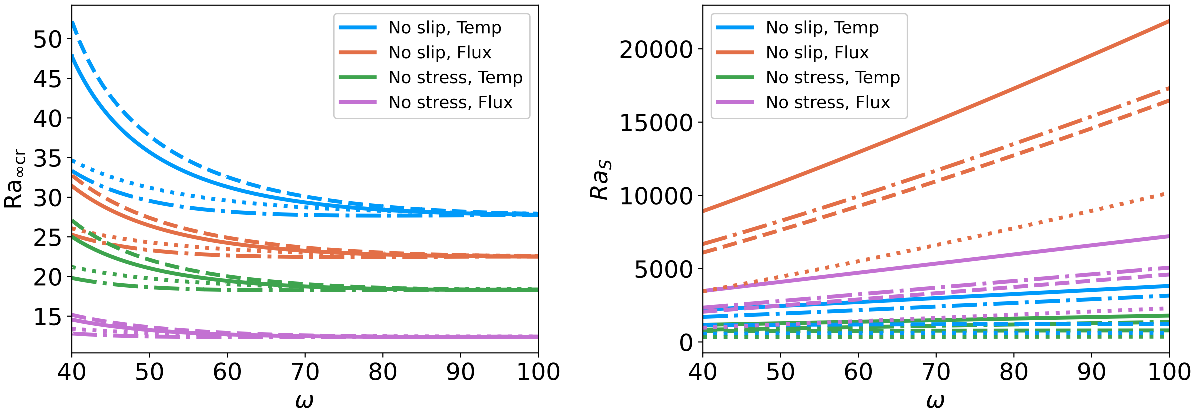

Figure 4.6: Comparison of results for all 16 possible combinations of boundary conditions and modulation style: no slip or no stress for velocity, zero temperature or no flux for temperature, and heat-flux or temperature modulation. Left: linear stability; Right: global stability. Color indicates the velocity boundary condition at the surface of modulation and the modulation type, with the associations listed in the legend. Line style indicates the boundary conditions at the non-modulated surface, with solid meaning no slip & zero temperature, dashed meaning no slip & no flux, dotted meaning no stress & no flux, and dash-dot meaning no stress & zero temperature. $\mathrm{Pr} = 1$.

4.6 Discussion

For all results found here, we have $\mathrm{Ra}_L > \mathrm{Ra}_A > \mathrm{Ra}_S$. Because nonlinear stability is a stronger notion and establishes a threshold below which the energy of all disturbances eventually decays, a weaker result, in this case a lower critical Rayleigh number, is expected for nonlinear stability when compared to linear stability.

At low frequencies, we have an analytical asymptotic result for strong global stability. As shown in section 4.4.1, the strong global stability threshold should approach the steady stability result for the same configuration, which is what we find in both the no-stress and no-slip results in figure 4.1. We also have an analytical asymptotic result for asymptotic stability with symmetric no-stress boundary conditions, temperature modulation, and a zero-temperature condition at the non-modulated surface. The numerical results agree with the analytical asymptotic result.

At high frequencies, we find that $\mathrm{Ra}_L\omega^{-2}$ approaches an $O(10)$ constant. This combination of the nondimensional parameters emerges from considering the problem from the beginning with an infinite depth, so that the governing parameter that emerges in the equation is $\mathrm{Ra}\omega^{-2}$, which is independent of d. For temperature modulation, the parameter is instead the $\mathrm{Ra}\omega^{-3/2}$, as used in Gershuni and Zhukhovitskii (1976) and Or and Kelly (1999). In the high-frequency limit, the critical disturbance is always found to be subharmonic.

For linear stability, solving the problem on a semi-infinite domain with the parameters Ra and ω replaced by the single parameter $\mathrm{Ra}\omega^{-2}$ or $\mathrm{Ra}\omega^{-3/2}$ confirms the results found for $\omega \gg 1$. For nonlinear stability, the critical Rayleigh numbers grow at a rate closer to $\mathrm{Ra} \sim \omega$ as $\omega \to \infty$, and it appears that both $\mathrm{Ra}_{\mathcal{S}}\omega^{-2}$ and $\mathrm{Ra}_{\mathcal{S}}\omega^{-2}$ go to zero in that limit. This means that the potential region for subcritical instabilities grows rapidly as $\omega \to \infty$. It would be of interest to explore this region with experiments or simulations to determine which stability threshold more accurately captures reality.

The dependence on Pr exhibited in figure 4.3 means that as $\mathrm{Pr} \to 0$, there is a wide range of possible Rayleigh numbers for subcritical instability. Asymptotic stability turns out to behave more like strong global stability than linear stability in the limits of small and large ω and Pr. For linear stability, the difference between the Rayleigh numbers for no-slip and no-stress decreases as $\mathrm{Pr} \to 0$.

4.7 Conclusion

We have described the first stability results for Rayleigh–Bénard convection with a modulated flux condition at one boundary, and we have also included results for a modulated temperature condition at one boundary. Three different notions of stability have been used: linear stability, asymptotic stability, and strong global stability. For all results found, the linear stability threshold is above both nonlinear stability thresholds, as expected. For velocity, both no-stress and no-slip velocity boundary conditions have been considered. For temperature, the bulk of the results come from a zero-temperature condition at the non-modulated surface, but a no-flux condition there has also been considered.

The critical Rayleigh number for linear stability Ra_L has different behavior in the small and large ω limits. Below a certain value of ω, the critical Rayleigh number arises alternately from synchronous and subharmonic disturbances and decreases non-monotonically as ω decreases, and the linear stability problem becomes ill conditioned for an $O(1)$ frequency.

For large enough ω, the critical instability is always subharmonic, and $\mathrm{Ra}_L\omega^{-2}$ and $\mathrm{Ra}_L\omega^{-3/2}$ approach an $O(10)$ constant in the modulated flux and modulated temperature cases, respectively. The critical Rayleigh numbers for nonlinear stability grow more slowly with ω, approximately linearly.

The modulated-flux setup considered here is relevant to situations in nature where a body of fluid experiences periodic heating at the surface, such as the diurnal heating of a lake by the sun. An example of this setup arising in the analysis of natural phenomena is Coenen et al. (2021). The nonlinear stability results complement the linear stability results, showing that the window of possible Rayleigh numbers for subcritical instability is relatively small for low frequencies but increases rapidly as $\omega \to \infty$.

We have treated the modulated-flux condition at one boundary as being representative of radiative heating confined to a thin layer near the surface, and we have also neglected effects from rotation. Future work could include these additional factors. Radiatively-driven convection without modulation has recently been used experimentally in Bouillaut et al. (2019) to observe the transition to the ultimate scaling regime of RB convection, where the Nusselt number scales with the square root of the Rayleigh number. Radiative heating could be incorporated into the stability methods used here, but the modulation profile would need to avoid unphysical radiative cooling.

When considering linear stability, rotation generally has a stabilizing effect on RB convection, as shown in Chandrasekhar (1961), and we would expect the same effect when combined with modulation. When considering nonlinear stability, the form of the energy used here in the energy method is not sensitive enough to include rotation because the inner product of the velocity with the Coriolis term is zero. To find nonlinear stability results with rotation, researchers have had to use a modified energy that leads only to conditional stability results, as detailed in Galdi, Straughan, and Chandrasekhar (1985), for example.

4.8 Numerical Methods

The stability calculations in this paper are all solved numerically by discretizing in space with Chebyshev polynomials. We have done this in three different ways, both for checking results with a different method and because different methods work better for different cases. The three ways are (1) Chebyshev differentiation matrices, (2) Chebyshev collocation in coefficient space, and (3) Chebyshev Galerkin projection.

4.8.1 Chebyshev differentiation matrices

The use of Chebyshev differentiation matrices is covered in Weideman and Reddy (2000) and Trefethen (2000). The basic idea is to approximate the solution using a truncated Chebyshev polynomial expansion. The result of applying the derivative operator to the solution may then be expressed as the result of a matrix times a vector containing the solution at Chebyshev grid points, so that $\mathrm{d}u/\mathrm{d}x$ becomes $\boldsymbol{Du}$. The Chebyshev grid points we use are defined by $x_j = \cos\left(\pi[1-(j-1)/(N-1)]\right)$, with $j = 1, 2, \ldots, N$.

To meet the boundary condition, we use what we will call the nullspace method, which does not seem to have been discussed in the literature until recently in Hsu, Hung, and Liao (2018). If the boundary conditions can be written in the form $\boldsymbol{B}\boldsymbol{u} = 0$, then the solution $\boldsymbol{u}$ must be in the nullspace of $\boldsymbol{B}$. We define $\boldsymbol{U} \equiv \text{nullspace}(\boldsymbol{B})$, and then we project the entire problem into the nullspace of $\boldsymbol{B}$. For example, if the eigenvalue problem is $u''(x) = -\lambda u(x)$, $u(0) = 0 = u(1)$, then the discretized problem is.

$$\boldsymbol{D}^2\boldsymbol{u} = -\lambda\boldsymbol{u}, \quad \boldsymbol{B}\boldsymbol{u} = 0, \tag{4.67}$$

where

$$\boldsymbol{u} = \begin{pmatrix} u(x_1) & u(x_2) & \dots & u(x_N) \end{pmatrix}^T, \quad \boldsymbol{B} = \begin{pmatrix} 1 & 0 & \dots & 0 \\ 0 & \dots & 0 & 1 \end{pmatrix}, \tag{4.68}$$

and $\boldsymbol{D}$ is the appropriately sized Chebyshev differentiation matrix. To project this into the nullspace of $\boldsymbol{B}$, we set $\boldsymbol{U} = \text{nullspace}(\boldsymbol{B})$, with $\boldsymbol{U}^\dagger\boldsymbol{U} = \boldsymbol{I}$ and assume $\boldsymbol{u}_*$ holds the coordinates of $\boldsymbol{u}$ expressed in the nullspace of $\boldsymbol{B}$ so that

$$\boldsymbol{u} = \boldsymbol{U}\boldsymbol{u}_*. \tag{4.69}$$

This leads to

$$\boldsymbol{D}^2\boldsymbol{U}\boldsymbol{u}_* = -\lambda\boldsymbol{U}\boldsymbol{u}_*, \tag{4.70}$$

and upon multiplication on the left by $\boldsymbol{U}^\dagger$, we have

$$\boldsymbol{M}\boldsymbol{u}_* = -\lambda\boldsymbol{u}_*, \tag{4.71}$$

with $\boldsymbol{M} = \boldsymbol{U}^\dagger\boldsymbol{D}^2\boldsymbol{U}$.

This is exactly how one would arrive at (4.22) using this method. Here we will walk through the procedure for the left-hand side of (4.22). We would have $\boldsymbol{A} \equiv \omega(\boldsymbol{D}^2 - k^2\boldsymbol{I})$

and $\boldsymbol{E} \equiv \omega \boldsymbol{I}$. Next we need to project the operator

$$\boldsymbol{H}_d \equiv \begin{pmatrix} \boldsymbol{A} & \mathbf{0} \\ \mathbf{0} & \boldsymbol{E} \end{pmatrix} \tag{4.72}$$

into the nullspace of the appropriate boundary condition operator. For no-stress conditions with heat-flux modulation at the bottom and a fixed-temperature condition at the top, we have $w(0) = w''(0) = \theta'(0) = 0$ at the bottom and $w(1) = w''(1) = \theta(1) = 0$ at the top. The boundary condition operator is therefore

$$\boldsymbol{B} \equiv \left(\begin{array}{cccc|cccc} 1 & 0 & \dots & 0 & 0 & \dots & \dots & 0 \\ 0 & \dots & 0 & 1 & 0 & \dots & \dots & 0 \\ \multicolumn{4}{c|}{\boldsymbol{D}^{\mathbf{2}}[\mathbf{1,:}]} & 0 & \dots & \dots & 0 \\ \multicolumn{4}{c|}{\boldsymbol{D}^{\mathbf{2}}[\boldsymbol{N}\mathbf{,:}]} & 0 & \dots & \dots & 0 \\ 0 & \dots & \dots & 0 & \multicolumn{4}{c}{\boldsymbol{D}[\mathbf{1,:}]} \\ 0 & \dots & \dots & 0 & 0 & \dots & \dots & 1 \end{array}\right), \tag{4.73}$$

so that

$$\boldsymbol{B} \begin{pmatrix} \boldsymbol{w} \\ \boldsymbol{\theta} \end{pmatrix} = \mathbf{0}. \tag{4.74}$$

The boundary condition operator $\boldsymbol{B}$ is unrelated to the $\boldsymbol{B}$ in (4.22), and the vertical line separates the columns applying to $\boldsymbol{w}$ and $\boldsymbol{\theta}$. The notation $\boldsymbol{D}[\mathbf{1,:}]$ indicates the first row of the derivative matrix, similar to the notation employed in many programming languages. The point corresponding to $z = 0$ is assumed to reside in the first index of $\boldsymbol{w}$ and $\boldsymbol{\theta}$. We now define

$$\boldsymbol{U} \equiv \text{nullspace}(\boldsymbol{B}) \tag{4.75}$$

and project $\boldsymbol{H}_d$ into this nullspace using

$$\boldsymbol{M} = \boldsymbol{U}^\dagger \boldsymbol{H}_d \boldsymbol{U}. \tag{4.76}$$

The same procedure is followed for the right-hand side of (4.24), with the result that all solutions to the resulting eigenvalue problem satisfy the boundary conditions.

4.8.2 Chebyshev collocation in coefficient space

For collocation with Chebyshev polynomials, we express the solutions in terms of basis functions consisting of Chebyshev polynomials combined so as to meet the boundary conditions. We therefore use different basis functions for w and θ, which we write as ϕ_n^w and ϕ_n^θ for the nth basis function of each type. The domain in z is discretized $z_j = (x_j + 1)/2$ with

$$x_j = \cos\theta_j, \quad \theta_j = \pi\left(1 - \frac{j-1}{N-1}\right), \quad j = 1, 2, \ldots, N. \tag{4.77}$$

A surface with a no-slip condition satisfies $\partial_z \phi_n^w = 0$, whereas a surface with a no-stress condition satisfies $\partial_z^2 \phi_n^w = 0$. A surface with a zero-temperature boundary condition satisfies $\phi_n^\theta = 0$, and a surface with a no-flux boundary condition satisfies $\partial_z \phi_n^\theta = 0$. In order to meet the boundary conditions, we use the following forms for the basis functions,

$$\phi_n^w(z) = T_{n+3}(z) + \sum_{j=0}^{3} a_{nj} T_j(z), \quad \phi_n^\theta(z) = T_{n+1}(z) + \sum_{j=0}^{1} b_{nj} T_j(z), \tag{4.78}$$

where T_j represents the jth Chebyshev polynomial. For each n, enforcing the six boundary conditions leads to six equations for the six unknowns a_{nj} and b_{nj}, resulting in basis functions that meet the boundary conditions. The Polynomials package for the Julia programming language was helpful in working with Chebyshev polynomials numerically.

To use these basis functions, for linear stability we start from (4.20) and (4.21) and assume solutions of the form

$$w(z,t) = \sum_{n=1}^{N} w_n(t)\phi_n^w(z), \quad \theta(z,t) = \sum_{n=1}^{N} \theta_n(t)\phi_n^\theta(z), \tag{4.79}$$

to find

$$\sum_n \left(\frac{\omega}{\mathrm{Pr}} w_n'(t) L\phi_n^w(z) - w_n(t)L^2\phi_n^2(z)\right) = -\sum_n \left(k^2 \mathrm{Ra}\,\theta_n(t)\phi_n^\theta(z)\right) \tag{4.80}$$

$$\sum_n \left(\omega\theta_n'(t)\phi_n^\theta(z) - \theta_n(t)L\phi_n^\theta(z)\right) = -\sum_n \partial_z T_{\mathrm{B}} w_n(t)\phi_n^w(z). \tag{4.81}$$

Now we use collocation and enforce the equation at the Chebyshev grid points. This leads to (4.22), with the vectors $\boldsymbol{w}$ and $\boldsymbol{\theta}$ containing the coefficients $w_n(t)$ and $\theta_n(t)$. For example, for the matrices $\boldsymbol{A}$ and $\boldsymbol{E}$ in (4.22) we have

$$A_{jn} \equiv \frac{\omega}{\mathrm{Pr}} L\phi_n^w(z_j), \quad E_{jn} \equiv \omega\phi_n^\theta(z_j), \tag{4.82}$$

and the other matrices are defined in the same manner. These individual matrices are N by N, and the vector holding the unknown coefficients w_n and θ_n has total length $2N$.

4.8.3 Chebyshev Galerkin projection

Chebyshev Galerkin projection starts in the same way as Chebyshev collocation. The same basis functions are used, but the differential equation is forced by driving the residual to zero on the basis space used rather than enforcing the differential equation at specific points as in collocation. We take the inner product of $2N$ basis functions with (4.80) and (4.81) to find $2N$ equations for the $2N$ unknown coefficients. The inner product is defined as

$$(f,g) \equiv \int_{-1}^{1} \frac{f(x)g(x)}{\sqrt{1-x^2}} \mathrm{d}x. \tag{4.83}$$

Taking the inner product of each of the $2N$ basis functions with each of the two equations would result in $4N$ equations, so that a choice must be made as to which basis functions to use. We have used velocity basis functions for (4.80) and temperature basis functions for (4.81).

For example, taking the inner product of equation (4.80) with ϕ_j^w leads to

$$\sum_n \left(\frac{\omega}{\mathrm{Pr}} w_n'(t) \left(\phi_j^w, L\phi_n^w\right) - w_n(t) \left(\phi_j^w, L^2\phi_n^w\right) \right) = -\sum_n k^2 \mathrm{Ra} \theta_n(t) \left(\phi_j^w, \phi_n^\theta\right), \qquad (4.84)$$

which could be written as

$$\sum_n \left(w_n'(t) A_{j,n} - w_n(t) B_{jn}\right) = \sum_n \theta_n(t) C_{jn}. \qquad (4.85)$$

The required integrations make the Galerkin projection method slower than collocation, but in the equations treated in this paper, it seems to create better conditioned matrices as well as better accuracy for a low number of modes. For this reason, Galerkin projection is useful in conjunction with the monodromy matrix method to find Floquet multipliers.

4.9 Nonlinear stability validation

Figure 4.7 shows results from Figure 4 in Homsy (1974) for asymptotic and strong global stability alongside our results for the same exact problem. Here the bottom boundary starts out warmer than the top (as in standard RB) and is then modulated. The results are fairly close, with some possible error in the process of digitizing the plot and extracting the results, as well as possible differences from the fact that only five to seven grid points were used with Gauss quadrature in the Homsy (1974), whereas 30 grid points have been used here.

Homsy claims the asymptotic result should go to the linear result for low frequen-

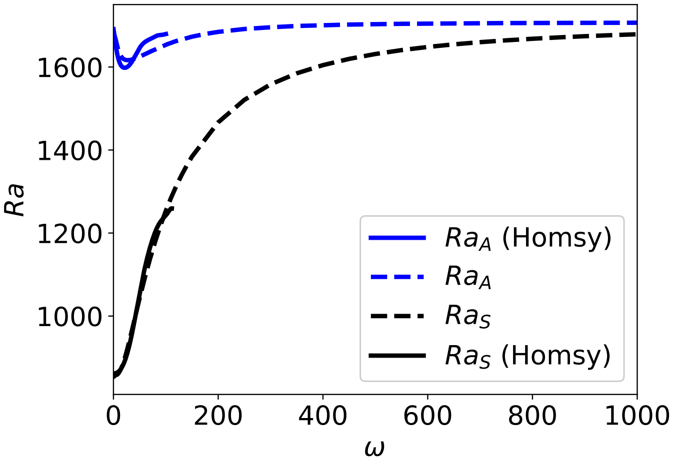

Figure 4.7: Comparison of results from Figure 4 in Homsy (1974) with our results for the same problem.

cies, but that is not what we find here. Homsy shows successfully that for no-stress conditions Ra_A goes to $\mathrm{Ra}_{L,\mathrm{steady}}$ at low frequencies for $\mathrm{Pr} = 1$, and our numerical results confirm this. He does not show anything analytically for no-slip conditions, but he does claim that his figure shows that Ra_A goes to $\mathrm{Ra}_{L,\mathrm{steady}}$ in that case as well. His figure, however, does not actually seem to show this, and our results indicate that in fact Ra_A goes to 1679 rather than 1708. For Ra_S, the low frequency limit appears to be $\mathrm{Ra}_{L,\mathrm{steady}}/2$.

Interestingly enough, Ra_A and Ra_S both go to $\mathrm{Ra}_{L,\mathrm{steady}}$ at large ω. At $\omega = 10^5$, both critical Rayleigh numbers are approximately equal to the standard threshold for no-slip conditions of 1707.76 with $k_{\mathrm{cr}} = 3.116$. This is to be expected, because at very high frequencies, the modulation effects would be confined to a very thin layer near the bottom. Modulation would therefore have a negligible effect on the temperature profile, essentially reducing the temperature profile to the profile with no modulation, and the threshold for instability would be the same as in the non-modulated case.

Chapter 4, in part, is being prepared for submission for publication as "Linear and nonlinear stability of Rayleigh–Bénard convection with zero-mean modulated heat flux" by T. W. Christopher and S. G. Llewellyn Smith. The dissertation author was the primary investigator and author of this material.

Chapter 5

Linear Stability: Low-Frequency Limit

5.1 Introduction

In this chapter, the WKB approximation is used to find the linear stability of boundary-temperature-modulated convection at low modulation frequencies. This is useful because solving the full linear stability problem numerically becomes increasingly difficult as the frequency is lowered. The major caveat is that only the case with no-stress boundaries is carried out successfully. Other boundary conditions present much greater difficulties, and possible approaches to circumvent these difficulties are discussed. In the no-stress case, the linear stability problem reduces to the Mathieu equation, and the Floquet multiplier method can be used on the WKB solution to the approximated stability problem. Constructing the overall WKB solution involves connecting different WKB solutions through two turning points.

For a given ω and Pr, we sweep through values of Ra and k, computing the monodromy matrix from the WKB approximation and then finding the eigenvalues of the monodromy matrix to determine stability. The lowest Ra resulting in instability is taken as the critical Rayleigh number, and the phase of the disturbance is recorded. We find that the phase of the disturbance switches between synchronous and subharmonic (half the nondimensional forcing frequency) as the nondimensional forcing frequency varies.

This WKB analysis is discussed in Or (2001), though the notation used means no explicit critical Rayleigh numbers are given. Here we explicitly compare WKB predictions to results from the full equations. A similar WKB analysis requiring connection through turning points is performed in Deng, Biondini, and Trillo (2016) in a different context, but they use a Mathieu equation with one of the parameters set to one.

5.2 Base state for low-frequency forcing

For temperature modulation at the bottom boundary, when time is scaled by the dimensional forcing frequency, the base state temperature obeys

$$\partial_t T = \omega^{-1} \partial_z^2 T, \quad T(0,t) = \cos t, \quad T(1,t) = 0. \tag{5.1}$$

It can be shown that for small ω the z-derivative of the solution is

$$\partial_z T = -\cos t(1 + O(\sqrt{\omega})), \tag{5.2}$$

where there is no z-dependence at leading order. We can understand this intuitively, because we expect that for a very slowly varying temperature, the profile has enough time to equilibrate to a linear profile with temperature $\cos t$ at the bottom and 0 at the top, and therefore

$$\frac{\Delta T}{\Delta z} \approx \frac{0 - \cos t}{1} = -\cos t. \tag{5.3}$$

5.3 Governing equations for low-frequency forcing

The equations governing perturbations for linear stability are (4.16) and (4.17), which we rewrite here for convenience:

$$\left(\omega\partial_t\nabla^2 - \mathrm{Pr}\nabla^4\right) w_{\mathrm{p}}(\boldsymbol{x},t) = \mathrm{Ra}\mathrm{Pr}\nabla^2_{\mathrm{H}}\theta_{\mathrm{p}}(\boldsymbol{x},t), \tag{5.4}$$

$$\left(\omega\partial_t - \nabla^2\right)\theta_{\mathrm{p}}(\boldsymbol{x},t) = -(\partial_z T_{\mathrm{B}})w_{\mathrm{p}}(\boldsymbol{x},t), \tag{5.5}$$

Using normal modes as in (4.18)–(4.19) and writing $k^2 = k_x^2 + k_y^2$, $L = \partial_z^2 - k^2$, we can turn these two equations into a single equation for $w(z,t)$:

$$\left[\frac{\omega^2}{\mathrm{Pr}}L\partial_t^2 - \omega(1+\mathrm{Pr}^{-1})L^2\partial_t + (L^3 - k^2\mathrm{Ra}\partial_z T_B)\right]\hat{w}(z,t) = 0. \tag{5.6}$$

We use no-stress boundary conditions so that

$$w = \partial_z^2 w = \partial_z^4 w = 0 \quad \text{at} \quad z = 0, 1. \tag{5.7}$$

As recognized over a century ago by Rayleigh (1916), in this special instance we can meet the boundary conditions by letting

$$w(z,t) = \sum_{n=1}^{\infty} w_n(t)\sin(n\pi z) \tag{5.8}$$

and examining the worst case value of n. This removes the spatial dependence from the problem completely, with the effect that the operator L becomes simply $(-n\pi^2 - k^2)$. This comes about because the sine functions are (i) eigenfunctions of the L operator, and (ii) orthogonal to each other. Using (5.8) in the governing equation (5.6) yields

$$\sum_{n=1}^{\infty}\left[\frac{\omega^2}{\mathrm{Pr}}\lambda_n w_n''(t)-\omega(1+\mathrm{Pr}^{-1})\lambda_n^2 w_n'(t)+(\lambda_n^3-k^2\mathrm{Ra}\partial_z T_B)w_n(t)\right]\sin(n\pi z)=0, \tag{5.9}$$

where $\lambda_n=-(n^2\pi^2+k^2)$. By taking the inner product of this infinite sum with each of the sine functions, we get a single decoupled equation for each n,

$$\frac{\omega^2}{\mathrm{Pr}}\lambda_n w_n''(t)-\omega(1+\mathrm{Pr}^{-1})\lambda_n^2 w_n'(t)+(\lambda_n^3-k^2\mathrm{Ra}\partial_z T_B)w_n(t)=0. \tag{5.10}$$

Note that this assumes $\partial_z T_\mathrm{B}$ is independent of z. We can transform these equations into canonical form using

$$w_n(t)=u_n(t)\mathrm{e}^{-(1+\mathrm{Pr})t/(2\epsilon)}, \quad \epsilon=\frac{\omega}{n^2\pi^2+k^2}, \tag{5.11}$$

so that the governing equation for $u_n(t)$ becomes

$$-\epsilon^2 u_n''(t)+\left(\frac{(1-\mathrm{Pr})^2}{4}+\frac{k^2\mathrm{Pr}\mathrm{Ra}\partial_z T_B}{(-n^2\pi^2-k^2)^3}\right)u_n(t)=0. \tag{5.12}$$

Now using the low-frequency approximation for the base state $\partial_z T_B=-\cos t$ leads to the Mathieu equation

$$\epsilon^2 u_n''(t)+Q(t)u_n(t)=0, \quad Q(t)\equiv\alpha-\beta\cos t, \tag{5.13}$$

where

$$\alpha\equiv-\frac{(1-\mathrm{Pr})^2}{4}, \quad \beta\equiv\frac{k^2\mathrm{Pr}\mathrm{Ra}}{(n^2\pi^2+k^2)^3}. \tag{5.14}$$

For context, we here recall that the Mathieu stability diagram consists of mostly stable regions below the line $\alpha=\beta$ for positive α, with tongues of instability rising off the

α axis at resonance points. In this case, we see that we always have $\alpha \leq 0$, so we are in the mostly unstable region of the left half-plane of the stability diagram. We must remember, however, that the velocity perturbation w_n includes exponential damping from (5.11), so that we are not looking for where u_n itself transitions to instability, but instead where u_n grows enough to overcome the exponential damping so that w_n transitions to instability. In general, higher β leads to larger growth, so that we set $n = 1$ as the worst case in all that follows and suppress the n subscript.

5.4 Floquet theory

The growth of (5.13) is determined using standard Floquet theory. We construct the monodromy matrix out of linearly independent solutions and their derivatives, and then the eigenvalues of the monodromy matrix reveal the maximum growth. The monodromy matrix is

$$\boldsymbol{M} = \boldsymbol{W}^{-1}(-\pi)\boldsymbol{W}(\pi), \tag{5.15}$$

where

$$\boldsymbol{W}(t) \equiv \begin{pmatrix} w_1(t) & w_2(t) \\ w_1'(t) & w_2'(t) \end{pmatrix} \tag{5.16}$$

and $w_1(t)$ and $w_2(t)$ represent linearly independent solutions to (5.10). In terms of the $u(t)$, the fundamental solution matrix is

$$\boldsymbol{W}(t) = \mathrm{e}^{-\gamma t} \begin{pmatrix} u_1(t) & u_2(t) \\ u_1'(t) - \gamma u_1(t) & u_2'(t) - \gamma u_2(t) \end{pmatrix}, \tag{5.17}$$

where $\gamma = (1 + Pr)/(2\epsilon)$. Because it is easier to construct the monodromy matrix for the Mathieu equation than for the equation in $w(t)$, we now show the relationship between

(5.15) and $\boldsymbol{U}(t)$, which is defined as

$$\boldsymbol{U}(t) \equiv \begin{pmatrix} u_1(t) & u_2(t) \\ u_1'(t) & u_2'(t) \end{pmatrix}. \tag{5.18}$$

The monodromy matrix for the Mathieu equation satisfies the equivalent of (5.15),

$$\boldsymbol{M}_U = \boldsymbol{U}^{-1}(-\pi)\boldsymbol{U}(\pi), \tag{5.19}$$

We can write (5.17) as

$$\boldsymbol{W}(t) = \mathrm{e}^{-\gamma t}\left(\boldsymbol{I} - \gamma\begin{pmatrix} 0 & 0 \\ 1 & 1 \end{pmatrix}\right)\boldsymbol{U}(t) \tag{5.20}$$

Defining

$$\boldsymbol{B} \equiv \boldsymbol{I} - \gamma\begin{pmatrix} 0 & 0 \\ 1 & 1 \end{pmatrix}, \tag{5.21}$$

we have

$$\boldsymbol{W}(t) = \mathrm{e}^{-\gamma t}\boldsymbol{B}\boldsymbol{U}(t). \tag{5.22}$$

Using the monodromy matrix definitions (5.15) and (5.19) then leads to

$$\boldsymbol{M} = \mathrm{e}^{-2\gamma\pi}\boldsymbol{M}_U. \tag{5.23}$$

This allows us to find the monodromy matrix for the standard Mathieu equation, which is useful because we will need to connect WKB solutions through turning points, and this is more straightforward for the Mathieu equation than for the original equation.

5.5 WKB approximation

The small parameter ϵ in (5.13) gives us the option of using the WKB approximation rather than finding a full numerical solution. In general, we have to find WKB solutions in three regions and connect them through the two turning points where $Q(t) = 0$. For $\alpha < -\beta$ and $\alpha > \beta$, there are no turning points, and the WKB solutions are real and imaginary exponentials, respectively. Only for $-\beta < \alpha < \beta$ are there two turning points. We do not treat the cases $\alpha = \pm\beta$, for which there would be only a single turning point.

When $\alpha < -\beta$, so that $Q(t) < 0$, there are no turning points, and the solutions are simply

$$u_{\pm}(t) = (-Q)^{-1/4} \mathrm{e}^{\pm S_i(t;\alpha,\beta)/\epsilon}, \tag{5.24}$$

where

$$S_i(t;\alpha,\beta) = \int_{-\pi}^{t} (-Q(t'))^{1/2} \mathrm{d}t'. \tag{5.25}$$

From these solutions we find that the monodromy matrix is

$$\boldsymbol{M}_U = \begin{pmatrix} \mathrm{e}^{S_i(\pi)/\epsilon} & 0 \\ 0 & \mathrm{e}^{-S_i(\pi)/\epsilon} \end{pmatrix}, \tag{5.26}$$

from which we may read off the eigenvalues.

When $-\beta < \alpha < \beta$, the overall solution is constructed using asymptotic matching of Airy functions near the turning points to the standard WKB solutions away from the turning points. The work is considerably more involved than in the previous case. We consider the turning points to be at $\pm c$ and write the solution in the first region as

$$u_1(t) = a_{11} u_{11}(t) + a_{12} u_{12}(t), \tag{5.27}$$

and the solution in the final region as

$$u_3(t) = a_{31}u_{31}(t) + a_{32}u_{32}(t). \tag{5.28}$$

By connecting through the two turning points, the relationship between the two sets of coefficients is found to be

$$\boldsymbol{a}_3 = \boldsymbol{C}\boldsymbol{a}_1 \tag{5.29}$$

where

$$\boldsymbol{C} = \frac{1}{4}\begin{pmatrix} 4\mathrm{e}^{S_2(c)/\epsilon} + \mathrm{e}^{-S_2(c)/\epsilon} & -\mathrm{i}4\mathrm{e}^{S_2(c)/\epsilon} + \mathrm{i}\mathrm{e}^{-S_2(c)/\epsilon} \\ \mathrm{i}4\mathrm{e}^{S_2(c)/\epsilon} - \mathrm{i}\mathrm{e}^{-S_2(c)/\epsilon} & 4\mathrm{e}^{S_2(c)/\epsilon} + \mathrm{e}^{-S_2(c)/\epsilon} \end{pmatrix}, \tag{5.30}$$

and

$$S_2(t) = \int_{-c}^{t} \sqrt{-Q(t')}dt', \quad -c \le t \le c. \tag{5.31}$$

To find the monodromy matrix, we need the fundamental solution matrix at the beginning and end, ensuring that we use the correct set of solutions. Before the first turning point we have

$$\boldsymbol{u}_1(t) = \boldsymbol{U}_1(t)\boldsymbol{a}_1, \tag{5.32}$$

where $\boldsymbol{u}_1(t)$ is a vector holding $u_1(t)$ and its derivative, and $\boldsymbol{a}_1$ is the vector of coefficients. After the second turning point we have

$$\boldsymbol{u}_3(t) = \boldsymbol{U}_3(t)\boldsymbol{a}_3, \tag{5.33}$$

Using (5.29) leads to

$$\boldsymbol{u}_3(t) = \boldsymbol{U}_3(t)\boldsymbol{C}\boldsymbol{a}_1. \tag{5.34}$$

The fundamental solution at the beginning is therefore $\boldsymbol{U}_1(-\pi)$, and its continuation to the end is $\boldsymbol{U}_3(\pi)\boldsymbol{C}$, so that we construct the monodromy matrix (5.19) as

$$\boldsymbol{M}_U = \boldsymbol{U}_1^{-1}(-\pi)\boldsymbol{U}_3(\pi)\boldsymbol{C}, \tag{5.35}$$

which is found to be

$$\boldsymbol{M}_U = \begin{pmatrix} \mathrm{e}^{2\mathrm{i}S_3(\pi)/\epsilon}\left(\mathrm{e}^{S_2(c)/\epsilon} + \frac{\mathrm{e}^{-S_2(c)/\epsilon}}{4}\right) & -\mathrm{i}\mathrm{e}^{2\mathrm{i}S_3(\pi)/\epsilon}\left(\mathrm{e}^{S_2(c)/\epsilon} - \frac{\mathrm{e}^{-S_2(c)/\epsilon}}{4}\right) \\ \mathrm{i}\mathrm{e}^{-2\mathrm{i}S_3(\pi)/\epsilon}\left(\mathrm{e}^{S_2(c)/\epsilon} - \frac{\mathrm{e}^{-S_2(c)/\epsilon}}{4}\right) & \mathrm{e}^{-2\mathrm{i}S_3(\pi)/\epsilon}\left(\mathrm{e}^{S_2(c)/\epsilon} + \frac{\mathrm{e}^{-S_2(c)/\epsilon}}{4}\right) \end{pmatrix}, \tag{5.36}$$

where

$$S_3(t) = \int_c^t \sqrt{-Q(t')}\mathrm{d}t'. \tag{5.37}$$

The determinant of this matrix is 1, and the trace is

$$\mathrm{tr}\ (\boldsymbol{M}_U) = 2\cos\left(\frac{2S_3(\pi)}{\epsilon}\right)\left(\mathrm{e}^{S_2(c)/\epsilon} + \frac{\mathrm{e}^{-S_2(c)/\epsilon}}{4}\right). \tag{5.38}$$

The eigenvalues of $\boldsymbol{M}_U$ can be written as

$$\nu_{1,2} = \frac{1}{2}\left(\mathrm{tr}\ (\boldsymbol{M}_U) \pm \sqrt{(\mathrm{tr}\ (\boldsymbol{M}_U))^2 - 4\det(\boldsymbol{M}_U)}\right). \tag{5.39}$$

If $\cos(2S_3(\pi)/\epsilon) \neq 0$, then as $\epsilon \to 0$ we see that

$$\nu_{1,2} \to \mathrm{tr}\ (\boldsymbol{M}_U), 0 \quad (\epsilon \to 0). \tag{5.40}$$

The Floquet multipliers $\lambda_{1,2}$ determining stability of the original system come from the eigenvalues of $\boldsymbol{M}$, which from the relation between $\boldsymbol{M}$ and $\boldsymbol{M}_U$ in (5.23) are simply

$$\lambda_{1,2} = \mathrm{e}^{-2\gamma\pi}\nu_{1,2}. \tag{5.41}$$

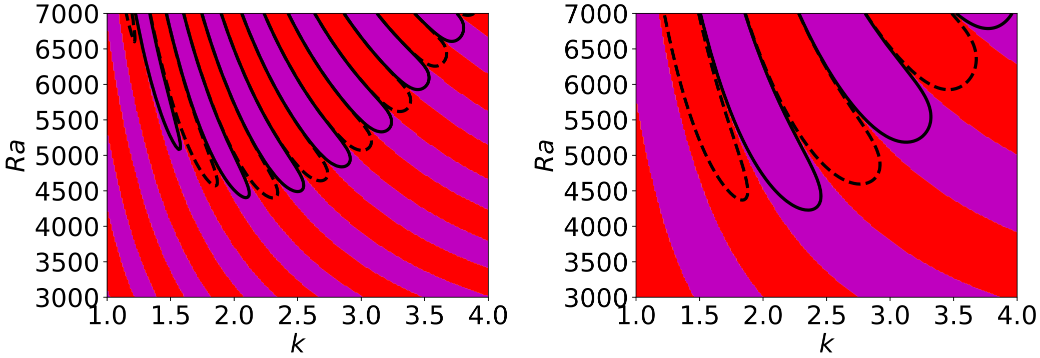

Figure 5.1: Stability diagrams with the stable and unstable regions separated by black curves. Left: $\omega = 2$; Right: $\omega = 5$. Red indicates the solution at that point is subharmonic, while magenta indicates the solution is synchronous. The bands of common phase narrow as the frequency is decreased.

Specializing now to $\epsilon \to 0$ and assuming $S_2(c) > 0$, we have

$$\lambda = 2\cos\left(\frac{2S_3(\pi)}{\epsilon}\right)\exp\left(\frac{S_2(c) - (1+\mathrm{Pr})\pi}{\epsilon}\right). \tag{5.42}$$

We see that the dividing point between Floquet multipliers that go to zero and those that grow exponentially as ϵ goes to zero must be where $S_2(c) = (1+\mathrm{Pr})\pi$. The combination that makes $S_2(c) - (1+\mathrm{Pr})\pi = 0$ is approximately $k = \pi/\sqrt{2}$, $\mathrm{Ra} = 4520$.

For each Pr and ω, we can produce a stability diagram in terms of Ra and k by finding the Floquet multiplier with the largest absolute value at each point. The lowest Ra resulting in instability is then deemed the critical Rayleigh number, Ra_{cr} for those values of Pr and ω. Example stability diagrams are shown in Figure 5.1, where $\mathrm{Pr} = 1$ and $\omega = 2$ and 5. We see that the Floquet multiplier results appear to be banded, with adjacent bands alternating between synchronous and subharmonic phases. As the frequency decreases, the bands narrow, as can be seen by comparing the stability diagrams for the two frequencies in Figure 5.1. The movement of the bands means that the value of Ra_{cr} and the frequency of the critical disturbance can change as the ω changes.

Finally, for fixed Pr we can compute Ra_{cr} as a function of ω. The results for $\mathrm{Pr} = 1$

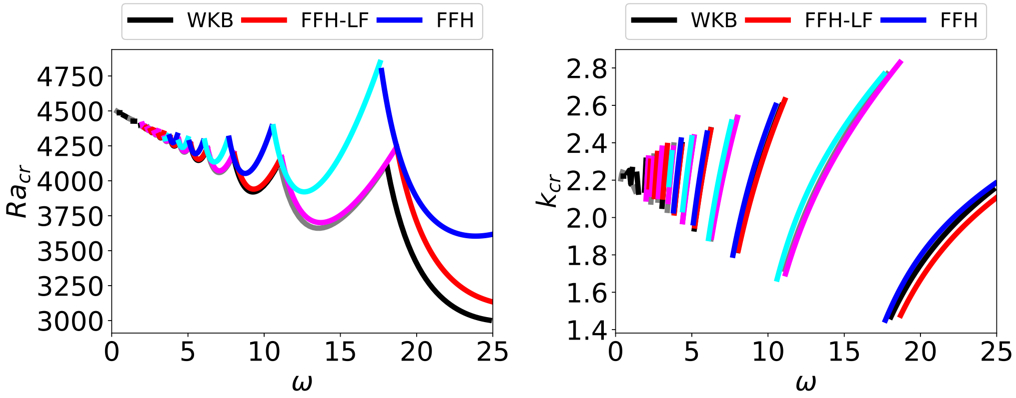

Figure 5.2: Critical Rayleigh numbers and wavenumbers for Pr = 1. Blue, red, and black correspond to critical instabilities with a subharmonic phase, whereas cyan, magenta, and gray correspond to critical instabilities with a synchronous phase. Floquet–Fourier–Hill results are indicated with FFH, and the LF designation means low frequency, i.e. that the FFH method was applied to the ODE in (5.10) with $n = 1$, which incorporates the low frequency approximation to the base state. The curves labeled simply FFH come from solving the PDE eigenvalue problem without making a low frequency approximation for the base state.

are shown in Figure 5.2, where a comparison is made with results from two separate linear stability calculations using the Floquet–Fourier–Hill method. The red/magenta curve comes from solving the exact ODE that the WKB approximation is applied to, and therefore serves as a check of the accuracy of the WKB solution. Both the Rayleigh number and wavenumber for the WKB and FFH-LF curves agree closely and even overlap up to $\omega \approx 18$, showing that the WKB approximation works well. The blue/cyan curve comes from a solution of the full PDE eigenvalue problem without using a low frequency approximation of the base state. The WKB solution increases in accuracy at lower frequencies, as expected, and even at higher frequencies is not far off in predicting the transition points between synchronous and subharmonic critical instabilities.

5.6 Difficulties posed by other boundary conditions

Treating other boundary conditions is nontrivial. The key factor that allows the no-stress conditions to be treated with relative ease is the ability to use sine functions, which have the following three key properties:

1. Meet boundary conditions
2. Eigenfunctions of L
3. Mutually orthogonal

The first property of meeting the boundary conditions is important because it is numerically preferable to use basis functions that meet the boundary conditions. The second property, that sine functions are eigenfunctions of L, means that the equation for each n involves only its own basis function, $\sin(n\pi z)$, rather than sprawling out to involve other basis functions. Tied together with the third property of orthogonality, which allows us to move from an infinite sum to a single equation for each n, we get an entirely decoupled system.

With different boundary conditions, we can no longer use sine functions, and we therefore attempt to use Chebyshev polynomials. However, we immediately must face the fact that, while we can combine Chebyshev polynomials in order to meet the new boundary conditions, the resulting functions will not necessarily be eigenfunctions of the operator L, and they will not necessarily be orthogonal to each other, though we can always make them orthogonal using Gram–Schmidt. Alternatively, we could simply use Chebyshev polynomials on their own as the basis, which would give us orthogonality, but we would then sacrifice meeting the boundary conditions, and the basis functions still would not be eigenfunctions of L, meaning we would have a coupled system. In sum, moving from no-stress conditions to other conditions means we must move away from sine functions, and that we must therefore sacrifice two of the three important properties possessed by the sine functions in the no-stress case.

5.7 Matrix WKB for other boundary conditions

To attempt to carry out the WKB analysis for other boundary conditions, we use Chebyshev polynomials combined to meet the boundary conditions. In general, for r boundary conditions, we define

$$\phi_n(x) = T_{(n+r-1)}(x) + \sum_{k=0}^{r-1} a_{nk} T_k(x), \tag{5.43}$$

and for each ϕ_n solve for the $\{a_{nk}\}$ that make ϕ_n meet the boundary conditions. We use these functions to represent the solution as

$$\hat{w}(z,t) = \sum_{n=1}^{\infty} w_n(t)\phi_n(z). \tag{5.44}$$

We use this approach on both the noncanonical and canonical form of the equations because it is not clear in advance which form might be better suited for numerical computation. We are not able to construct full solutions in either case, but we record the results here for future work to build on. The various issues preventing the finding of a complete solution are discussed in the section treating the canonical form of the differential equation.

5.7.1 Noncanonical Form

The governing differential equation can be written as

$$\left[\omega^2 a_2 L \partial_t^2 - \omega a_1 L^2 \partial_t + (L^3 + a_0 \cos t)\right] \hat{w}(z,t) = 0, \tag{5.45}$$

where

$$a_2 = \mathrm{Pr}^{-1}, \quad a_1 = 1 + \mathrm{Pr}^{-1}, \quad a_0 = k^2\mathrm{Ra}. \tag{5.46}$$

Using the form (5.44) in the differential equation leads to

$$\sum_{n=1}^{\infty} \left(\omega^2 a_2 L\phi_n w_n'' - \omega a_1 L^2 \phi_n w_n' + L^3 \phi_n w_n + a_0 \cos t \phi_n w_n\right) = 0. \tag{5.47}$$

At this point, we truncate the solution expansion at N and then use either a pseudospectral method or a Galerkin projection method to remove the spatial dependence. For the pseudospectral method, we would simply evaluate the equation at N Chebyshev grid points, and for the Galerkin projection method we would take the inner product of the first N basis functions with the equation, being left in both cases with N coupled ODEs in time. In both cases, we can write the equation in matrix form as

$$\omega^2 \boldsymbol{A}_2 \boldsymbol{w}'' + \omega \boldsymbol{A}_1 \boldsymbol{w}' + \left(\boldsymbol{A}_\alpha + \boldsymbol{A}_\beta \cos t\right) \boldsymbol{w} = 0. \tag{5.48}$$

We now use the WKB approximation and write

$$\boldsymbol{w}(t) = \mathrm{e}^{\Omega(t)/\omega} \sum_{k=0}^{\infty} \omega^k \boldsymbol{w}_k(z, t). \tag{5.49}$$

Using this in (5.48) shows that at leading order $\Omega'(t)$ satisfies the quadratic eigenvalue problem

$$O(1): \quad \left[(\lambda)^2 \boldsymbol{A}_2 + \lambda \boldsymbol{A}_1 + \left(\boldsymbol{A}_\alpha + \boldsymbol{A}_\beta \cos t\right)\right] \boldsymbol{w}_0 = 0 \tag{5.50}$$

where we have defined

$$\lambda = \Omega'. \tag{5.51}$$

The vector $\boldsymbol{w}_0$ is a right eigenvector. We define the right and left eigenvectors for this problem through

$$\left[(\lambda_n(t))^2 \boldsymbol{A}_2 + \lambda_n(t)\boldsymbol{A}_1 + (\boldsymbol{A}_\alpha + \boldsymbol{A}_\beta \cos t)\right] \boldsymbol{v}_n = 0, \tag{5.52}$$

$$\boldsymbol{u}_n^\dagger \left[(\lambda_n(t))^2 \boldsymbol{A}_2 + \lambda_n(t)\boldsymbol{A}_1 + (\boldsymbol{A}_\alpha + \boldsymbol{A}_\beta \cos t)\right] = 0, \tag{5.53}$$

and we assume the eigenvectors to be normalized to have length 1. We note that the left and right eigenvectors are not necessarily orthogonal for generalized or polynomial eigenvalue problems. For each of the $2N$ eigenvalues, we have a solution for Ω'. Writing $\Omega'_n = \lambda_n$, the corresponding $\boldsymbol{w}_0$ must be proportional to $\boldsymbol{v}_n$, so we write $\boldsymbol{w}_0$ as

$$\boldsymbol{w}_0 = f_n(t)\boldsymbol{v}_n, \tag{5.54}$$

with the understanding that we will find $2N$ viable $\boldsymbol{w}_0$ as long as all eigenvectors are independent.

At the next order, we find

$$O(\omega): \quad \boldsymbol{A}_2(2\boldsymbol{w}_0'\lambda_n + \boldsymbol{w}_0\lambda_n') + \boldsymbol{A}_1\boldsymbol{w}_0' + (\lambda_n)^2\boldsymbol{A}_2\boldsymbol{w}_1 + \lambda_n\boldsymbol{A}_1\boldsymbol{w}_1 + (\boldsymbol{A}_\alpha + \boldsymbol{A}_\beta \cos t)\boldsymbol{w}_1 = 0 \tag{5.55}$$

We multiply this equation on the left by $\boldsymbol{u}_n^\dagger$ to eliminate all terms involving $\boldsymbol{w}_1$, leaving

$$\boldsymbol{u}_n^\dagger\boldsymbol{A}_2(2\boldsymbol{w}_0'\lambda_n + \boldsymbol{w}_0\lambda_n') + \boldsymbol{u}_n^\dagger\boldsymbol{A}_1\boldsymbol{w}_0' = 0 \tag{5.56}$$

Using (5.54) then leads to

$$f_n'(t)\left(\boldsymbol{u}_n^\dagger\boldsymbol{A}_2\boldsymbol{v}_n 2\lambda_n + \boldsymbol{u}_n^\dagger\boldsymbol{A}_1\boldsymbol{v}_n\right) + f_n(t)\left(\boldsymbol{u}_n^\dagger\boldsymbol{A}_2\boldsymbol{v}_n' 2\lambda_n + \boldsymbol{u}_n^\dagger\boldsymbol{A}_2\boldsymbol{v}_n\lambda_n'\boldsymbol{u}_n^\dagger\boldsymbol{A}_1\boldsymbol{v}_n'\right) \tag{5.57}$$

If we assume

$$\boldsymbol{u}_n^\dagger \left(2\lambda_n \boldsymbol{A}_2 + \boldsymbol{A}_1\right) \boldsymbol{v}_n \neq 0, \tag{5.58}$$

then we have the solution

$$f_n(t) = \exp\left(-\int^t \frac{\boldsymbol{u}_n^\dagger \left(2\lambda_n \boldsymbol{A}_2 + \boldsymbol{A}_1\right) \boldsymbol{v}_n' + \boldsymbol{u}_n^\dagger \boldsymbol{A}_2 \boldsymbol{v}_n \lambda_n'}{\boldsymbol{u}_n^\dagger \left(2\lambda_n \boldsymbol{A}_2 + \boldsymbol{A}_1\right) \boldsymbol{v}_n} \mathrm{d}t'\right). \tag{5.59}$$

Our complete WKB approximation to the solution is then

$$\boldsymbol{w}(t) = \sum_{n=1}^{2N} c_n f_n(t) \boldsymbol{v}_n(t) \mathrm{e}^{\omega^{-1} \int_{t_0}^t \lambda_n(t')\mathrm{d}t'}. \tag{5.60}$$

Unfortunately, evaluating the failure condition in (5.58) must be done numerically, and it is not clear how to connect solutions around failure points for $N > 1$.

For $N = 1$, we recapture standard WKB. In this case if we set $\boldsymbol{A}_2 = 1$, $\boldsymbol{A}_1 = 0$, and $\boldsymbol{A}_\alpha + \boldsymbol{A}_\beta \cos t = -Q(t)$, the leading order eigenvalue problem reduces to $\lambda(t)^2 = Q(t)$. For $f_n(t)$, we find

$$f_n(t) = \exp\left(-\int^t \frac{\lambda_n'}{2\lambda_n} \mathrm{d}t'\right) = \lambda_n^{-1/2}, \tag{5.61}$$

so that the solution is

$$w(t) = \frac{c_1 \mathrm{e}^{\int^t \sqrt{Q(t')}\mathrm{d}t'} + c_2 \mathrm{e}^{-\int^t \sqrt{Q(t')}\mathrm{d}t'}}{Q^{1/4}}. \tag{5.62}$$

The solution fails when $\lambda = 0$ and therefore when $Q(t) = 0$.

5.7.2 Canonical Form

By using a suitable Chebyshev discretization, we can let the solution become a vector $\hat{w}(z, t) \to \boldsymbol{w}(t)$, and then let $\boldsymbol{w}(t) = \boldsymbol{U}(t)\boldsymbol{v}(t)$, and find the necessary $\boldsymbol{U}(t)$ to eliminate the first derivative term to arrive at the canonical second order ODE

$$\omega^2 \ddot{\boldsymbol{v}} - \boldsymbol{Q}(t)\boldsymbol{v} = 0. \tag{5.63}$$

While this equation is certainly possible to write down, it is not at all clear that it will be numerically useful. The matrix function $\boldsymbol{Q}(t)$ is defined as

$$\boldsymbol{Q}(t) = -\boldsymbol{U}^{-1}(t)\left(\omega^2 \ddot{\boldsymbol{U}}(t) + \omega \boldsymbol{A}_2^{-1}\boldsymbol{A}_1 \ddot{\boldsymbol{U}}(t) + \boldsymbol{A}_2^{-1}\boldsymbol{A}_0(t)\boldsymbol{U}(t)\right) \tag{5.64}$$

and $\boldsymbol{U}$ is

$$\boldsymbol{U}(t) = \exp\left(-\frac{t}{2\omega}\boldsymbol{A}_2^{-1}\boldsymbol{A}_1\right), \tag{5.65}$$

from which it can be shown that $\boldsymbol{Q}$ does not depend on ω.

It is possible to construct WKB approximations to solutions of this system of ODEs. We assume a solution of the form

$$\boldsymbol{v}(t) = \left(\sum_{n=0}^{\infty} \hat{\boldsymbol{v}}_n(t)\epsilon^n\right) \mathrm{e}^{\omega^{-1}\Omega(t)} \tag{5.66}$$

The leading order shows that

$$O(1): \quad \boldsymbol{Q}(t)\hat{\boldsymbol{v}}_0(t) = (\Omega'(t))^2 \hat{\boldsymbol{v}}_0(t), \tag{5.67}$$

showing that $(\Omega'(t))^2$ is an eigenvalue of $\boldsymbol{Q}(t)$, and $\hat{\boldsymbol{v}}_0(t)$ is the corresponding eigenvector. If we define

$$\boldsymbol{Q}(t)\boldsymbol{\eta}_n(t) = \lambda_n(t)\boldsymbol{\eta}_n(t), \tag{5.68}$$

where $\boldsymbol{\eta}_n(t)$ is normalized so that $\boldsymbol{\eta}_n^\dagger \boldsymbol{\eta}_n = 1$, then for each eigenvalue of $\boldsymbol{Q}$ we have two working possibilities for $\Omega'(t)$, namely

$$\Omega_n'(t) = \pm\sqrt{\lambda_n(t)}. \tag{5.69}$$

We can write the nth possibility for $\hat{\boldsymbol{v}}_0$ as

$$\hat{\boldsymbol{v}}_{n0} = f_n(t)\boldsymbol{\eta}_n(t) \tag{5.70}$$

If each of the eigenvalues λ_n is distinct, then each eigenvalue yields two solutions, so that if $\boldsymbol{v}(t)$ has N components, we find N eigenvalues and $2N$ solutions, exactly as we would expect for a problem that is second order in time. If any of the eigenvalues are repeated, however, then two of the Ω_n' are the same, and we may no longer have $2N$ linearly independent solutions. Repeated eigenvalues λ_n with different eigenvectors $\boldsymbol{\eta}_n$ will still yield linearly independent solutions, but repeated eigenvalues with the same eigenvector mean that there is no longer a full set of linearly independent solutions.

Proceeding to the next order, we find

$$O(\omega): \quad \Omega_n''(t)\hat{\boldsymbol{v}}_{n0}(t) + 2\Omega_n'(t)\hat{\boldsymbol{v}}_{n0}'(t) = \boldsymbol{Q}(t)\hat{\boldsymbol{v}}_{n1}(t) - \Omega_n'(t)^2\hat{\boldsymbol{v}}_{n1}(t). \tag{5.71}$$

Using (5.70) leads to

$$\Omega_n'' f_n\boldsymbol{\eta}_n + 2\Omega_n'(f'\boldsymbol{\eta}_n + f\boldsymbol{\eta}_n') = \boldsymbol{Q}(t)\hat{\boldsymbol{v}}_{n1}(t) - \Omega_n'(t)^2\hat{\boldsymbol{v}}_{n1}(t). \tag{5.72}$$

We can eliminate the terms on the right side of the equation by multiplying from the left side by a left eigenvector of $\boldsymbol{Q}$, where the left eigenvectors satisfy

$$\boldsymbol{\zeta}_n(t)^\dagger\boldsymbol{Q}(t) = \lambda_n(t)\boldsymbol{\zeta}_n(t)^\dagger, \quad \boldsymbol{\zeta}_m^\dagger\boldsymbol{\eta}_n = \delta_{mn}. \tag{5.73}$$

Multiplying on the left by $\boldsymbol{\zeta}_m^\dagger$ turns the $O(\omega)$ equation into

$$\Omega_n'' f_n \delta_{mn} + 2\Omega_n'(f_n' \delta_{mn} + f_n \boldsymbol{\zeta}_m^\dagger \boldsymbol{\eta}_n'(t)) = 0, \tag{5.74}$$

For $m \neq n$, this simply reduces to $\boldsymbol{\zeta}_m^\dagger \boldsymbol{\eta}_n = \delta_{mn}$, while for $m = n$ we have

$$\Omega_n'' f_n + 2\Omega_n'(f_n' + f \boldsymbol{\zeta}_n^\dagger \boldsymbol{\eta}_n'(t)) = 0, \tag{5.75}$$

Solving for $f_n(t)$ we find

$$f_n(t) = \exp\left(-\int^t \frac{\Omega_n''(s) + 2\Omega_n'(s)\boldsymbol{\zeta}_n^\dagger(s)\boldsymbol{\eta}_n'(s)}{2\Omega_n'(s)} \mathrm{d}s \right), \quad (\Omega_n' \neq 0). \tag{5.76}$$

Here we find an extra condition for our solution to be valid, namely that Ω_n' not be zero. We can simplify the solution for f_n by writing $\Omega_n''/\Omega_n' = \lambda_n'/\lambda_n$ as the derivative of $\log \Omega_n' = \log \sqrt{\lambda_n}$, leading to

$$f_n(t) = (\lambda_n(t))^{-1/4} \exp\left(-\int^t \boldsymbol{\zeta}_n^\dagger(s)\boldsymbol{\eta}_n'(s)\mathrm{d}s \right). \tag{5.77}$$

The general WKB solution to (5.63) can then be written as

$$\boldsymbol{v}(t) = \sum_{n=1}^{N} \left(a_n \mathrm{e}^{\omega^{-1}\int_{t_0}^t \sqrt{\lambda_n(s)}\mathrm{d}s} + b_n \mathrm{e}^{-\omega^{-1}\int_{t_0}^t \sqrt{\lambda_n(s)}\mathrm{d}s} \right) \lambda_n(t)^{-1/4} \mathrm{e}^{-\int_{t_0}^t \boldsymbol{\zeta}_n^\dagger(s)\boldsymbol{\eta}_n'(s)\mathrm{d}s} \boldsymbol{\eta}_n(t), \tag{5.78}$$

provided that there are N independent eigenvectors at each point in time and that there are no zero eigenvalues.

Turning point issues

This breaks down when $\lambda_n(t) = 0$ or when two eigenvectors coincide (implying two eigenvalues coincide), and we will refer to these points as turning points. At turning points, we can attempt to examine the differential equation close to the turning points and hope to diagonalize things and arrive at decoupled equations that we know asymptotic results for, as happens in the scalar case with Airy equations. Unfortunately this does not seem to be possible in general. Expanding the equation $\omega^2 \ddot{\boldsymbol{v}} - \boldsymbol{Q}\boldsymbol{v} = 0$ near a turning point at $t = t_0$ gives $\boldsymbol{Q}(t) \approx \boldsymbol{Q}(t_0) + (t - t_0)\boldsymbol{Q}'(t_0)$ and therefore

$$\omega^2 \ddot{\boldsymbol{v}} - (\boldsymbol{Q}(t_0) + (t - t_0)\boldsymbol{Q}'(t_0))\boldsymbol{v} = O((t - t_0)^2). \tag{5.79}$$

In the scalar case, the eigenvalue $\lambda(t)$ is simply $Q(t)$ and the eigenvector is 1. This means that $\Omega' = \pm\sqrt{Q(t)}$. Therefore $Q(t_0)$ must be zero for there to be a turning point, leaving us with an Airy equation for which we know asymptotic relations. However, in the vector case, $\boldsymbol{Q}(t_0)$ is not itself zero but rather has at least one zero (or repeated) eigenvalue. We can attempt to diagonalize and decouple by using the eigenvectors of $\boldsymbol{Q}(t_0)$ as our new basis, but the system does not decouple, and it is unclear how to connect solutions around turning points.

Attempt to decouple using left and right eigenvectors

We can let the left and right eigenbases of $\boldsymbol{Q}(t_0)$ be

$$\boldsymbol{Q}(t_0)\boldsymbol{Y} = \boldsymbol{Y}\boldsymbol{\Lambda}, \quad \boldsymbol{X}^\dagger \boldsymbol{Q}(t_0) = \boldsymbol{\Lambda}\boldsymbol{X}^\dagger, \quad \boldsymbol{X}^\dagger \boldsymbol{Y} = \boldsymbol{I}, \tag{5.80}$$

and then switch into the eigenbasis with

$$\boldsymbol{v}(t) = \boldsymbol{Y}\boldsymbol{v}_*(t) \tag{5.81}$$

and use this in (5.79) to find

$$\ddot{\boldsymbol{v}}_* - \boldsymbol{\Lambda}\boldsymbol{v}_* - (t - t_0)\left(\boldsymbol{X}^\dagger \boldsymbol{Q}'(t_0)\boldsymbol{Y}\right)\boldsymbol{v}_* = 0. \tag{5.82}$$

Unless $\boldsymbol{X}^\dagger \boldsymbol{Q}'(t_0)\boldsymbol{Y}$ is diagonal, this equation is coupled, and there is no reason it would necessarily be diagonal. The same issue occurs if one tries to use Jordan canonical form.

Attempt to construct integral solution

By analogy with scalar WKB, where connection formulas can be found using the Airy equation near turning points, we would like to construct the equivalent of Airy functions near our turning points. One way to do this would be to find an integral representation of the solution and then investigate the asymptotic values of the integral away from the turning point, just as can be done in the scalar case to find Airy asymptotics.

We start from (5.82), which we write as

$$\boldsymbol{u}''(t) - \boldsymbol{\Lambda}\boldsymbol{u}(t) - t\boldsymbol{B}\boldsymbol{u}(t) = 0, \tag{5.83}$$

so that the turning point is at $t_0 = 0$. To find an integral solution, we start by assuming

$$\boldsymbol{u}(t) = \int_C \mathrm{e}^{st}\hat{\boldsymbol{u}}(s)\mathrm{d}s, \tag{5.84}$$

where the path of integration C is chosen so that $\hat{\boldsymbol{u}}$ is zero at the end points. Substituting this into the ODE leads to

$$\boldsymbol{B}\hat{\boldsymbol{u}}'(s) = \boldsymbol{\Lambda}\hat{\boldsymbol{u}}(s) - s^2\hat{\boldsymbol{u}}(s). \tag{5.85}$$

Assuming we can invert $\boldsymbol{B}$, we have

$$\hat{\boldsymbol{u}}'(s) = \boldsymbol{B}^{-1}\left(\boldsymbol{\Lambda} - s^2\boldsymbol{I}\right)\hat{\boldsymbol{u}}(s). \tag{5.86}$$

We would like to solve this with a matrix exponential, so that the solution would simply be

$$\hat{\boldsymbol{u}} \overset{?}{=} \exp\left(\boldsymbol{B}^{-1}\left(\boldsymbol{\Lambda} s - \frac{s^3}{3}\boldsymbol{I}\right)\right)\boldsymbol{b}, \tag{5.87}$$

with a constant vector $\boldsymbol{b}$ determined from given conditions, but from the definition of the matrix exponential and the product rule for differentiation we know that

$$\frac{\mathrm{d}}{\mathrm{d}t}\mathrm{e}^{\boldsymbol{A}(t)} = \sum_{n=1}^{\infty}\frac{1}{n!}\left(\sum_{k=1}^{n}\boldsymbol{A}^k\boldsymbol{A}'(t)\boldsymbol{A}^{n-k-1}\right), \tag{5.88}$$

which is only equal to $\boldsymbol{A}'(t)\mathrm{e}^{\boldsymbol{A}(t)}$ if $\boldsymbol{A}'(t)$ commutes with $\boldsymbol{A}(t)$, in which case it is also equivalent to $\mathrm{e}^{\boldsymbol{A}(t)}\boldsymbol{A}'(t)$. From (5.87) we have

$$\boldsymbol{A}(s) = \boldsymbol{B}^{-1}\left(\boldsymbol{\Lambda} s - \frac{s^3}{3}\boldsymbol{I}\right) \implies \frac{\mathrm{d}}{\mathrm{d}s}\boldsymbol{A}(s) = \boldsymbol{B}^{-1}\left(\boldsymbol{\Lambda} - s^2\boldsymbol{I}\right). \tag{5.89}$$

The matrices in parentheses are diagonal, but unless $\boldsymbol{B}^{-1}$ is also diagonal (or some other special form), we do not have the desired commutation property, and therefore the matrix exponential solution written in (5.87) is not valid.

Chapter 6

Linear Stability: High-Frequency Limit

A very deep lake can be represented by letting $d \to \infty$ and using the resulting base state in the linear stability analysis. The Rayleigh number by itself loses meaning for infinite d, and the combinations $\mathrm{Ra}_\infty = \mathrm{Ra}\omega^{-3/2}$ for temperature modulation and $\mathrm{Ra}_\infty = \mathrm{Ra}\omega^{-2}$ for heat-flux modulation are used instead so that d is no longer present. This is the parameter that naturally appears if the length scale is chosen as the Stokes layer $\sqrt{\kappa/\omega_*}$ instead of d, In this limit, the nondimensional frequency goes to infinity and ceases to be a useful parameter, so that in addition to Ra_∞, the most important parameter remaining is Pr.

The nondimensional equations in this case are (2.24)–(2.26) but with length scaled by $\sqrt{\kappa/\omega_*}$ instead of d, leading to

$$\partial_t \boldsymbol{u} + \boldsymbol{u} \cdot \nabla \boldsymbol{u} = -\nabla p + \mathrm{Ra}_\infty \, \mathrm{Pr} \, T \boldsymbol{e}_z + \mathrm{Pr} \nabla^2 \boldsymbol{u}, \tag{6.1}$$

$$\nabla \cdot \boldsymbol{u} = 0, \tag{6.2}$$

$$\partial_t T + \boldsymbol{u} \cdot \nabla T = \nabla^2 T + \frac{S(t)}{\gamma} \mathrm{e}^{z/\gamma}. \tag{6.3}$$

The vertical domain is $z \in (-\infty, 0]$.

6.1 Boundary forcing

For temperature or heat-flux modulation at the boundary, $S(t)$ in (6.3) is zero. For zero-mean modulation, a single cosine with frequency ω_* is used for the forcing profile, with maximum f_0 for the temperature forcing and maximum g_0 for the flux forcing. We solve the problem on the domain $z \in (-\infty, 0]$, so that the forcing is at the top. The boundary conditions on the temperature after nondimensionalization are therefore

$$\text{Top } (z=0): \begin{cases} T = \cos t & \text{specified temperature} \\ \partial_z T = \cos t & \text{specified flux} \end{cases} \tag{6.4}$$

$$\text{Bottom } (z=-\infty): \begin{cases} T = 0 & \text{specified temperature} \\ \partial_z T = 0 & \text{no flux.} \end{cases} \tag{6.5}$$

Solving these equations for the base state temperature profile results in considerable simplification from the general base state for modulated-flux forcing in a finite domain in (4.14), namely

$$T_{\mathrm{B}}(z,t) = \begin{cases} \mathrm{e}^{z/\sqrt{2}} \cos\left(t + z/\sqrt{2}\right) & \text{specified temperature at top} \\ \mathrm{e}^{z/\sqrt{2}} \cos\left(t + z/\sqrt{2} - \pi/4\right) & \text{specified flux at top.} \end{cases} \tag{6.6}$$

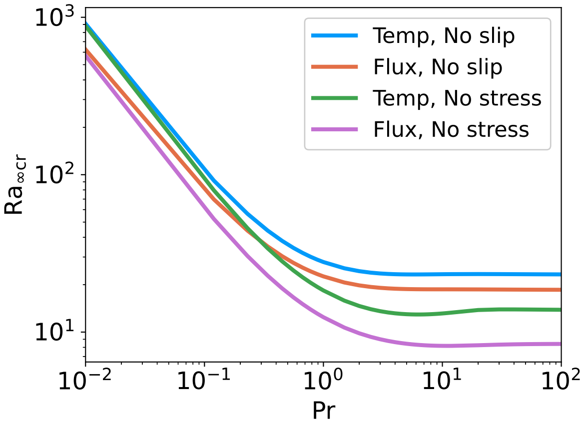

Figure 6.1: Critical Rayleigh number as a function of Pr for all combinations of top boundary forcing and boundary conditions in a semi-infinite domain. The designations "temp" and "flux" indicate temperature and heat flux modulation, respectively. The forcing profile is single-cosine modulation in all cases.

These base states are the same whether the bottom boundary condition has the temperature or flux going to zero. The Rayleigh numbers are

$$\mathrm{Ra}_\infty = \begin{cases} \alpha g f_0 \sqrt{\kappa} \left(\nu \omega_*^{3/2}\right)^{-1} & \text{specified temperature at top} \\ \alpha g g_0 \kappa \left(\nu k \omega_*^2\right)^{-1} & \text{specified flux at top} \end{cases} \tag{6.7}$$

Linear stability results are shown in figure 6.1. The critical Rayleigh number was found to always result from a Floquet exponent with an imaginary part of one half. The dependence of the critical Rayleigh number on the Prandtl number is the same as that observed for linear stability in a finite domain, as shown in Figure 4.3.

For low Pr, $\mathrm{Ra}_{\infty\mathrm{cr}}$ demonstrates a power law dependence on Pr. The difference between a no-slip and no-stress boundary at the top diminishes, with the main difference at low Pr being between modulated temperature and modulated flux at the top boundary. A low Pr indicates high heat diffusivity relative to momentum diffusivity, and therefore it is expected that as Pr goes to zero, the Rayleigh number needed for instability should increase without bound, which is seen in the results. We note, however, that as shown in

Figure 4.3 this logic does not hold for nonlinear stability.

For high Pr, $\mathrm{Ra}_{\infty\mathrm{cr}}$ appears to asymptotically approach a different constant value for each case. The dependence of $\mathrm{Ra}_{\infty\mathrm{cr}}$ on Pr starts to level out beyond a Prandtl number of one. As expected, the two no-slip cases require a higher Rayleigh number for linear instability than the two no-stress cases in this high-Pr regime.

6.2 Radiative heating

The governing equations for modulated radiative heating are the full equations in (6.1)–(6.3). To model radiative heating, we use a zero-mean modulated heat generation term in the form of an exponential that decays with depth, as discussed in 2.3. We will use a Newtonian boundary condition at $z = 0$, the same surface the radiative heating enters. The Newtonian boundary condition in dimensional terms is

$$k\partial_{z_*}T_* = h(f_*(t_*) - T_*), \tag{6.8}$$

where $f_*(t_*)$ is the ambient temperature of the atmosphere above the water surface. After the first step of nondimensionalization, we have

$$\frac{\partial T}{\partial z} = \frac{hL}{k}\left(\frac{f_0}{T_{\mathrm{sc}}}f(t) - T\right). \tag{6.9}$$

Using (2.23) to substitute for T_{sc}, we find

$$\frac{\partial T}{\partial z} = \frac{hL}{k}\left(\frac{kf_0}{S_0L}f(t) - T\right). \tag{6.10}$$

We define

$$\mathrm{H} \triangleq \frac{hL}{k}, \quad \chi \triangleq \frac{kf_0}{S_0L} \tag{6.11}$$

and arrive at

$$\frac{\partial T}{\partial z} = \mathrm{H}\left(\chi f(t) - T\right). \tag{6.12}$$

The boundary conditions become

$$\text{Top } (z=0): \quad \partial_z T = \mathrm{H}\left(\chi f(t) - T\right) \tag{6.13}$$

and

$$\text{Bottom } (z=-1): \begin{cases} T = 0 & \text{specified temperature} \\ \partial_z T = 0 & \text{no flux.} \end{cases} \tag{6.14}$$

Because we are considering a semi-infinite domain, we once again find that ω disappears into Ra_∞, leaving Pr as a key parameter. In this case, however, we must incorporate the three additional parameters H, χ, and γ, while also choosing an ambient temperature profile $f(t)$ for the Newtonian boundary condition at the top to go along with the modulation from $S(t)$ in the radiative-heating term.

We use zero-mean modulation with a single cosine with frequency ω_* for the radiative heating term. Choosing the time scale for the semi-infinite domain to be ω_*^{-1} we then

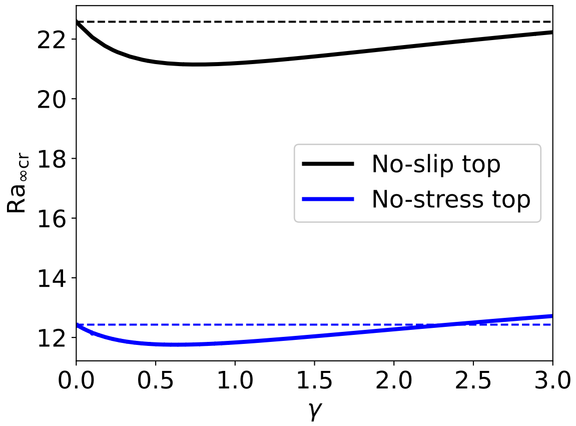

Figure 6.2: Critical Rayleigh number as a function of the e-folding scale γ for radiative heating in a semi-infinite domain. The modulated-flux result is shown as a dotted line, and the results for both top boundary conditions indicate that the radiative case reduces to the flux case in the limit of a low e-folding scale.

have

$$S(t) = \cos t \tag{6.15}$$

$$f(t) = \cos t. \tag{6.16}$$

We also use (2.21), where the length scale for a semi-infinite domain is chosen as $\sqrt{\kappa/\omega_*}$ rather than d, the additional parameters become

$$\mathrm{H} = \frac{h\sqrt{\kappa}}{k\sqrt{\omega_*}}, \quad \chi = \frac{f_0 k \omega_*}{S_0 \kappa}, \quad \gamma = \frac{d_{\mathrm{rad}}\sqrt{\omega_*}}{\sqrt{\kappa}}. \tag{6.17}$$

We now consider a scenario in which (i) the convection coefficient H between the atmosphere and the water goes to zero, so that a no-heat-flux condition results, and (ii) the e-folding scale γ of the radiative heating goes to zero, so that the incoming heat is completely dispensed in a very thin boundary layer at the surface. We also set χ equal to one, meaning the maximum of the ambient temperature is equal to the temperature scale from radiative heating. Figure 6.2 shows that when these conditions hold, we recapture the results of modulated heat flux, as expected. Furthermore, the critical Rayleigh number does not change appreciably for γ of $O(1)$, and we can therefore be confident that results using modulated flux capture the essence of radiative heating with a small e-folding scale. All critical disturbances were found to be subharmonic, meaning the Floquet exponent has an imaginary part of one half.

One problem with using simple sinusoidal modulation with radiative heating is that the symmetric nature of the term brings cooling throughout half the period along with the heating in the other half. While this is physically unrealistic, the results show that mathematically the inclusion of radiative heating has no dramatic effect in this case and does in fact reduce to an imposed heat flux in the appropriate limit mentioned above.

Chapter 7

Bounding Flow Quantities

7.1 Introduction

Investigations of the linear and nonlinear stability of modulated convection configurations go back at least to Gershuni and Zhukhovitskii (1963) for linear stability and to Homsy (1974) for nonlinear stability. The review in Davis (1976) describes the work to that time, and work has continued steadily to the present day, including recent linear stability calculations such as Hazra, Kumar, and Mitra (2020) and numerical simulations such as Yang et al. (2020).

Work on bounding flow quantities, where an upper bound is sought on a flow quantity of interest, has its roots in Malkus (1954) and Howard (1963). The method of bounding known as the background flow technique was pioneered by Doering and Constantin (1992). We are not aware of any work on bounds for modulated convection. To our knowledge, the only bounding analysis dealing with modulation is Marchioro (1994), who found a bound on energy dissipation in shear flow between horizontal parallel plates with one plate modulated horizontally.

In this paper, we use the background flow technique to find an upper bound on the temperature dissipation for the standard Rayleigh–Bénard configuration but with one boundary temperature that can vary in time. We follow Marchioro (1994) closely, but we frame the analysis in the notation of Doering and Gibbon (1995).

7.2 Setup

We work with two parallel plates extending infinitely far in the x- and y-directions containing fluid satisfying the Boussinesq equations,

$$\partial_{t_*}\boldsymbol{u}_* + \boldsymbol{u}_* \cdot \nabla_* \boldsymbol{u}_* = -\frac{1}{\rho_0}\nabla_* p_* + \alpha g T_* \hat{\boldsymbol{z}} + \nu \nabla_*^2 \boldsymbol{u}_*, \tag{7.1}$$

$$\nabla_* \cdot \boldsymbol{u}_* = 0, \tag{7.2}$$

$$\partial_{t_*} T_* + \boldsymbol{u}_* \cdot \nabla_* T_* = \kappa \nabla_*^2 T_*, \tag{7.3}$$

where asterisks represent dimensional quantities, $\boldsymbol{u}_*$ is the velocity, T_* is the temperature measured with respect to the reference temperature at the upper boundary, ρ_0 is the density at the reference temperature, g is the acceleration due to gravity, ν is the kinematic viscosity, κ is the thermal diffusivity, α is the thermal expansion coefficient, and p_* is the pressure. The boundary conditions are

$$\boldsymbol{u}_* = 0 \quad \text{at} \quad z_* = 0, d, \tag{7.4}$$

$$T_* = f_*(t_*) \quad \text{at} \quad z_* = 0, \tag{7.5}$$

$$T_* = 0 \quad \text{at} \quad z_* = 1, \tag{7.6}$$

where d is the domain size in the z-direction. On the horizontal boundaries, we take $\boldsymbol{u}_*$ and T_* to be periodic (this can be relaxed to e.g. the no-slip adiabatic conditions $\boldsymbol{u}_* = \boldsymbol{0}$

and $\partial_n T_* = 0$). We nondimensionalize using

$$t \equiv \frac{\kappa t_*}{d^2}, \quad \boldsymbol{x} \equiv \frac{\boldsymbol{x}_*}{d}, \quad \boldsymbol{u} \equiv \frac{d\boldsymbol{u}_*}{\kappa}, \quad T \equiv \frac{T_*}{\Delta T}, \quad f(t) \equiv \frac{f_*(t_*)}{\Delta T} \tag{7.7}$$

and an appropriate scaling for pressure. The temperature scale ΔT is left unspecified for now. The most convenient choice for ΔT will in general depend on the boundary temperature profile $f_*(t_*)$. This is discussed further below.

Using the nondimensional variables in (7.7), the nondimensional governing equations become

$$\partial_t \boldsymbol{u} + \boldsymbol{u} \cdot \nabla \boldsymbol{u} = -\nabla p + \mathrm{RaPr} T \hat{\boldsymbol{z}} + \mathrm{Pr} \nabla^2 \boldsymbol{u}, \tag{7.8}$$

$$\nabla \cdot \boldsymbol{u} = 0, \tag{7.9}$$

$$\partial_t T + \boldsymbol{u} \cdot \nabla T = \nabla^2 T. \tag{7.10}$$

The boundary conditions become

$$\boldsymbol{u} = 0 \quad \text{at} \quad z = 0, 1, \tag{7.11}$$

$$T = f(t) \quad \text{at} \quad z = 0, \tag{7.12}$$

$$T = 0 \quad \text{at} \quad z = 1. \tag{7.13}$$

The Rayleigh number, Ra, and Prandtl number, Pr, are defined as

$$\mathrm{Ra} \equiv \frac{\alpha g \Delta T d^3}{\nu \kappa}, \quad \mathrm{Pr} \equiv \frac{\nu}{\kappa}. \tag{7.14}$$

For later use in the bounding argument, we introduce the following two dimensionless parameters, both assumed to be finite,

$$M = \sup|f(t)|, \quad \omega = \sup|f'(t)|. \tag{7.15}$$

7.3 Finding the bound

We decompose using the background flow technique by writing the temperature as

$$T(\boldsymbol{x}, t) = \tau(z, t) + \theta(\boldsymbol{x}, t), \tag{7.16}$$

where τ satisfies the boundary conditions on T so that

$$\tau(0, t) = f(t), \quad \tau(1, t) = 0, \quad \theta(0, t) = 0 = \theta(1, t). \tag{7.17}$$

We now find appropriate power integrals. We begin by taking the inner product of $\boldsymbol{u}$ with the momentum equation (7.8) and integrating over the volume. The power integral for velocity is

$$\frac{\mathrm{d}}{\mathrm{d}t}\left(\frac{\|\boldsymbol{u}\|_2^2}{2}\right) = \mathrm{RaPr}\int_V w\theta \mathrm{d}V - \mathrm{Pr}\,\|\nabla\boldsymbol{u}\|_2^2, \tag{7.18}$$

where we have integrated by parts. The usual norms will be employed for scalars, vectors and tensors:

$$\|f\|_2^2 = \int_V f^2 \mathrm{d}V, \qquad \|\boldsymbol{a}\|_2^2 = \int_V |\boldsymbol{a}|^2 \mathrm{d}V, \qquad \|\nabla\boldsymbol{u}\|_2^2 = \int_V \left(\frac{\partial u_i}{\partial x_j}\frac{\partial u_i}{\partial x_j}\right) \mathrm{d}V. \tag{7.19}$$

For the temperature, we use the background decomposition (7.16) in (7.10), multiply the result by θ, and integrate to find

$$\frac{\mathrm{d}}{\mathrm{d}t}\left(\frac{\|\theta\|_2^2}{2}\right) = -\int_V \theta\partial_t\tau \mathrm{d}V - \int_V \theta w \partial_z \tau \mathrm{d}V - \frac{1}{2}\|\nabla T\|_2^2 + \frac{1}{2}\|\partial_z\tau\|_2^2 - \frac{1}{2}\|\nabla\theta\|_2^2. \tag{7.20}$$

Noticing that each of the power integrals has an integral involving the product $w\theta$, we divide (7.18) by RaPr and combine the two integrals to get

$$\frac{1}{2}\frac{\mathrm{d}}{\mathrm{d}t}\left(\|\theta\|_2^2 + \frac{\|\boldsymbol{u}\|_2^2}{\mathrm{RaPr}}\right) = -\int_V \theta\partial_t\tau \mathrm{d}V - \frac{\|\nabla T\|_2^2}{2} + \frac{\|\partial_z\tau\|_2^2}{2} - \mathcal{H}[\theta,\tau,\boldsymbol{u}], \tag{7.21}$$

where we have defined the quadratic-form functional

$$\mathcal{H}[\theta,\tau,\boldsymbol{u}] = \int_V \left(\frac{|\nabla\theta|^2}{2} + \frac{|\nabla\boldsymbol{u}|^2}{\mathrm{Ra}} + \theta w(\partial_z\tau - 1)\right)\mathrm{d}V. \tag{7.22}$$

We now take a time average, denoted by the operator $\langle\cdot\rangle = T^{-1}\int_0^T(\cdot)\mathrm{d}t$, to get

$$\begin{aligned}\left\langle\frac{\|\nabla T\|_2^2}{2}\right\rangle =& \left\langle\frac{\|\partial_z\tau\|_2^2}{2}\right\rangle - \left\langle\int_V \theta\partial_t\tau\mathrm{d}V\right\rangle - \langle\mathcal{H}[\theta,\tau,\boldsymbol{u}]\rangle \\ &- \frac{1}{2T}\left(\|\nabla\theta\|_2^2 + \frac{\|\nabla\boldsymbol{u}\|_2^2}{\mathrm{RaPr}}\right)\Bigg|_{t=T} + \frac{1}{2T}\left(\|\nabla\theta\|_2^2 + \frac{\|\nabla\boldsymbol{u}\|_2^2}{\mathrm{RaPr}}\right)\Bigg|_{t=0},\end{aligned} \tag{7.23}$$

which allows us to write

$$\left\langle\frac{\|\nabla T\|_2^2}{2}\right\rangle \leq \left\langle\frac{\|\partial_z\tau\|_2^2}{2}\right\rangle - \left\langle\int_V \theta\partial_t\tau\mathrm{d}V\right\rangle - \langle\mathcal{H}[\theta,\tau,\boldsymbol{u}]\rangle + \frac{1}{2T}\left(\|\nabla\theta\|_2^2 + \frac{\|\nabla\boldsymbol{u}\|_2^2}{\mathrm{RaPr}}\right)\Bigg|_{t=0}. \tag{7.24}$$

If the initial state is finite, we take $T \to \infty$ from now on, so that the last term goes to zero, leading to

$$\left\langle \frac{\|\nabla T\|_2^2}{2} \right\rangle \leq \left\langle \frac{\|\partial_z \tau\|_2^2}{2} \right\rangle - \left\langle \int_V \theta \partial_t \tau \mathrm{d}V \right\rangle - \langle \mathcal{H}[\theta, \tau, \boldsymbol{u}] \rangle . \tag{7.25}$$

Now if we impose $\mathcal{H} \geq 0$, which we shall follow Doering and Gibbon (1995) in calling the "spectral constraint," then we are left with a bound on the temperature dissipation, albeit with a dependence on the fluctuation θ that we will have to work to eliminate.

With the spectral constraint enforced, we have

$$\langle \|\nabla T\|_2^2 \rangle \leq \langle \|\partial_z \tau\|_2^2 \rangle - 2 \left\langle \int_V \theta \partial_t \tau \mathrm{d}V \right\rangle , \tag{7.26}$$

which corresponds to the solution of the variational problem

$$\begin{aligned} \langle \|\nabla T\|_2^2 \rangle \leq \inf \Bigg\{ \langle \|\partial_z \tau\|_2^2 \rangle - 2 \left\langle \int_V \theta \partial_t \tau \mathrm{d}V \right\rangle \Bigg| \\ &\mathcal{H}[\theta, \tau, \boldsymbol{u}] = \int_V \left(\frac{|\nabla \theta|^2}{2} + \frac{|\nabla \boldsymbol{u}|^2}{\mathrm{Ra}} + \theta w (\partial_z \tau - 1) \right) \mathrm{d}V \geq 0, \\ &\tau(0,t) = f(t), \ \tau(1,t) = 0, \\ &\theta(x,y,0,t) = 0 = \theta(x,y,1,t), \\ &\nabla \cdot \boldsymbol{u} = 0, \\ &\boldsymbol{u}(x,y,0,t) = 0 = \boldsymbol{u}(x,y,1,t) \Bigg\} . \end{aligned} \tag{7.27}$$

In theory, we could use Lagrange multipliers to enforce the constraints, find the Euler–Lagrange equations, and thereby solve the problem. In practice, because an exact solution is difficult, we simply try different background profiles. Any background profile satisfying the constraints will provide an upper bound on the temperature dissipation.

The guiding principle in choosing the background profile will be to satisfy the spectral constraint, and to do that we need the term $\theta w(\partial_z \tau - 1)$, to be as small as we can make it because it is the only term in the spectral constraint that can be negative. From the boundary conditions, we know that the velocity, $\boldsymbol{u}$, and the temperature fluctuations, θ, are small near the boundaries but possibly large away from the boundaries. To neutralize this, we try to make $(\partial_z\tau - 1)$ small away from the boundaries.

The simplest profile to try is a piecewise linear profile with two sections. From the above discussion, we make $\partial_z\tau = 1$ away from the bottom boundary while enforcing $\tau(0,t) = f(t)$ at the bottom boundary, which gives us

$$\tau(z,t) = \begin{cases} f(t) - z\delta^{-1}(f(t) - \delta + 1) & 0 \leq z \leq \delta \\ z - 1 & \delta \leq z \leq 1. \end{cases} \tag{7.28}$$

In order to make progress on the bound in (7.26), we use the inequalities listed in 7.6. First we ensure that we meet the spectral constraint, $\mathcal{H}[\theta, \tau, \boldsymbol{u}] \geq 0$, or

$$\left(\int_V \frac{|\nabla\theta|^2}{2} + \frac{|\nabla\boldsymbol{u}|^2}{\mathrm{Ra}} + \theta w(\partial_z\tau - 1)\right)\mathrm{d}V \geq 0, \tag{7.29}$$

which clearly requires us to work on the last term. Using our definition of the linear piecewise profile leads to

$$\int_V \theta w(\partial_z\tau - 1)\mathrm{d}V = -\frac{f(t)+1}{\delta}\int_0^\delta\left(\int_A w\theta\mathrm{d}A\right)\mathrm{d}z, \tag{7.30}$$

where A is the nondimensional horizontal area of the system. This allows us to find

$$\left|\int_V \theta w(\partial_z\tau - 1)\mathrm{d}V\right| \leq \frac{(M+1)}{\delta}\int_0^\delta \left|\int_A w\theta\,\mathrm{d}A\right|\mathrm{d}z \tag{7.31}$$

$$\leq \frac{(M+1)\delta}{2}\left\|\partial_z w\right\|_2\left\|\partial_z\theta\right\|_2 \tag{7.32}$$

$$\leq \frac{(M+1)\delta}{4}\left(\eta\left\|\partial_z w\right\|_2^2 + \frac{1}{\eta}\left\|\partial_z\theta\right\|_2^2\right) \tag{7.33}$$

$$\leq \frac{(M+1)\delta}{4}\left(\frac{\eta\left\|\nabla\boldsymbol{u}\right\|_2^2}{4} + \frac{\left\|\nabla\theta\right\|_2^2}{\eta}\right), \tag{7.34}$$

for any positive η. Here we used (7.58) to go from (7.31) to (7.32); Young's inequality, $2ab \leq \eta a^2 + \eta^{-1}b^2$ ($\eta > 0$), to go from (7.32) to (7.33); and the incompressibility inequality (7.62) and the definition of the two-norm to go from (7.33) to (7.34).

We use this result to find the necessary δ and η to enforce the spectral constraint,

$$\mathcal{H}[\theta,\tau,\boldsymbol{u}] = \left(\int_V \frac{|\nabla\theta|^2}{2} + \frac{|\nabla\boldsymbol{u}|^2}{\mathrm{Ra}} + \theta w(\partial_z\tau - 1)\right)\mathrm{d}V$$

$$\geq \frac{\left\|\nabla\theta\right\|_2^2}{2} + \frac{\left\|\nabla\boldsymbol{u}\right\|_2^2}{\mathrm{Ra}} - \frac{(M+1)\delta}{4}\left(\frac{\eta\left\|\nabla\boldsymbol{u}\right\|_2^2}{4} + \frac{\left\|\nabla\theta\right\|_2^2}{\eta}\right) \tag{7.35}$$

$$= \left\|\nabla\boldsymbol{u}\right\|_2^2\left(\frac{1}{\mathrm{Ra}} - \frac{(M+1)\eta\delta}{16}\right) + \left\|\nabla\theta\right\|_2^2\left(\frac{1}{2} - \frac{(M+1)\delta}{4\eta}\right), \tag{7.36}$$

which means that we require

$$\frac{1}{\mathrm{Ra}} \geq \frac{(M+1)\eta\delta}{16}, \quad \frac{1}{2} \geq \frac{(M+1)\delta}{4\eta} \tag{7.37}$$

to satisfy $\mathcal{H} \geq 0$. Provided that

$$\delta \leq \frac{4\sqrt{2}}{(M+1)\sqrt{\mathrm{Ra}}}, \tag{7.38}$$

any value of η satisfying $(M+1)\delta/2 \leq \eta \leq 16/(\mathrm{Ra}(M+1)\delta)$ can be used to satisfy (7.37).

From (7.26) we work towards the desired bound. We use (7.59) to get

$$\left\langle \|\nabla T\|_2^2 \right\rangle \leq \left\langle \|\partial_z \tau\|_2^2 \right\rangle + \frac{8}{15}\omega\delta^{3/2}\sqrt{A}\left\langle \|\nabla\theta\|_2 \right\rangle . \tag{7.39}$$

Next we use the convexity inequality (7.60) to obtain

$$\left\langle \|\nabla T\|_2^2 \right\rangle \leq \left\langle \|\partial_z \tau\|_2^2 \right\rangle + \frac{8}{15}\omega\delta^{3/2}\sqrt{A}\left\langle \|\nabla\theta\|_2^2 \right\rangle^{1/2} , \tag{7.40}$$

and (7.61) to eliminate the temperature fluctuation, leaving

$$\left\langle \|\nabla T\|_2^2 \right\rangle \leq \left\langle \|\partial_z \tau\|_2^2 \right\rangle + \frac{8\sqrt{2}}{15}\omega\delta^{3/2}\sqrt{A}\left(\left\langle \|\nabla T\|_2^2 \right\rangle + \left\langle \|\partial_z \tau\|_2^2 \right\rangle \right)^{1/2} , \tag{7.41}$$

which we can write as

$$\varepsilon_T \leq a + b\sqrt{\varepsilon_T + a}. \tag{7.42}$$

Solving inequality (7.42) results in

$$\varepsilon_T \leq a + \frac{b^2}{2} + \frac{b}{2}\sqrt{8a + b^2}. \tag{7.43}$$

We have

$$\varepsilon_T \equiv \left\langle \|\nabla T\|_2^2 \right\rangle , \tag{7.44}$$

$$a \equiv \left\langle \|\partial_z \tau\|_2^2 \right\rangle = A\left(\frac{\langle f^2\rangle + 2\langle f\rangle + 1}{\delta} - 2\langle f\rangle - 1 \right) , \tag{7.45}$$

$$b \equiv \frac{8\sqrt{2}}{15}\omega\delta^{3/2}\sqrt{A}, \tag{7.46}$$

Written out, the bound becomes

$$\frac{\|\nabla T\|_2^2}{A} \leq \frac{F}{\delta} - 2\langle f\rangle - 1 + \left(\frac{8}{15}\right)^2 \omega^2\delta^3 + \frac{4\sqrt{2}\omega\delta^{3/2}}{15}\left(2\left(\frac{8}{15}\right)^2\omega^2\delta^3 + 8\left(\frac{F}{\delta} - 2\langle f\rangle - 1\right)\right)^{1/2}, \tag{7.47}$$

where $F = \langle f^2\rangle + 2\langle f\rangle + 1$, and the bound is valid for all $\delta \leq \delta_{\max}$, with

$$\delta_{\max} \equiv \frac{4\sqrt{2}}{(M+1)\sqrt{\mathrm{Ra}}} \leq 1 \implies \mathrm{Ra} \geq \frac{32}{(M+1)^2}. \tag{7.48}$$

Let us denote the right-hand side of the bound in (7.47) as $h(\delta)$. It now remains to choose an optimal $\delta_{\text{opt}} \leq \delta_{\max}$ in order to obtain the smallest bound in (7.47). This leads to an optimization problem for δ_{opt} that in general must be solved numerically. We note that Ra does not appear in h explicitly, instead serving only to restrict the maximum value of δ. For large ω and Ra, we can find asymptotic representations for δ_{opt}, and therefore for the bound.

7.4 Limits and examples

7.4.1 Large-ω limit

Examining the order of the terms in (7.47) shows that $\delta_{\text{opt}} \sim \omega^{-1/2}$ provides the optimal bound for large ω. Calculating $h'(\delta)$ with $\omega = \Omega\delta_{\text{opt}}^{-2}$ and expanding for small δ leads to a quadratic for Ω^2. The appropriate solution leads to

$$\delta_{\text{opt}} = C_0 F^{1/4}\omega^{-1/2} \tag{7.49}$$

where $C_0 = (\sqrt{15}/4)(13 - 5\sqrt{19/3})^{1/4} \approx 0.78$. To leading order we find that the minimum bound corresponds to

$$\frac{\|\nabla T\|_2^2}{A} \leq D_0 F^{3/4}\sqrt{\omega} - E_0(2\langle f \rangle + 1) + O(\omega^{-1/2}), \tag{7.50}$$

where $D_0 \approx 2.26$ and $E_0 \approx 1.32$. The large ω bound depends on Ra only through the restriction that $\omega \gg \mathrm{Ra}$, as Ra does not appear explicitly in the bound. The bound breaks down when $\delta_{\mathrm{opt}} \sim \delta_{\mathrm{max}}$, which, from equating (7.49) with the expression for δ_{max} in (7.48), corresponds to

$$\omega = \frac{C_0^2}{32}(M+1)^2 F^{1/2}\mathrm{Ra} \approx 0.02(M+1)^2 F^{1/2}\mathrm{Ra}. \tag{7.51}$$

7.4.2 Large-Ra limit

With no time dependence, $\omega = 0$ and the bound in (7.47) looks like δ^{-1}, so that choosing the largest value for δ gives the best bound. Furthermore, from consideration of the large ω limit, we know that $\delta_{\mathrm{opt}} = \delta_{\mathrm{max}}$ when $\mathrm{Ra} \sim \omega$ as in (7.51) and for larger Ra. We therefore take $\delta_{\mathrm{opt}} = \delta_{\mathrm{max}}$ for large Ra. The bound on the temperature dissipation in (7.47) is then

$$\begin{aligned}\frac{\|\nabla T\|_2^2}{A} \leq & \frac{(M+1)F}{4\sqrt{2}}\sqrt{\mathrm{Ra}} - 2\langle f \rangle - 1 + \frac{c^2\omega^2\mathrm{Ra}^{-3/2}}{2(M+1)^3} \\ & + \frac{c\omega F^{1/2}\mathrm{Ra}^{-1/2}}{2^{3/4}(M+1)}\left(1 + \frac{c^2\omega^2\mathrm{Ra}^{-2}}{(M+1)^4\sqrt{2}} - \frac{8(2\langle f \rangle + 1)\mathrm{Ra}^{-1/2}}{\sqrt{2}(M+1)F}\right)^{1/2},\end{aligned} \tag{7.52}$$

where $c = 2^{(29/4)}/15$ and Ra must satisfy the restriction in (7.48). Expanding this for $\omega \ll \mathrm{Ra}$ and $\mathrm{Ra} \gg 1$, we can write the bound as

$$\begin{aligned}\frac{\|\nabla T\|_2^2}{A} \leq &\frac{(M+1)F}{4\sqrt{2}}\sqrt{\mathrm{Ra}} - 2\langle f\rangle - 1 + \frac{c\omega\sqrt{F}\mathrm{Ra}^{-1/2}}{2^{3/4}(M+1)} \\ &- \frac{2^{3/4}c\omega(2\langle f\rangle+1)}{(M+1)^2\sqrt{F}}\mathrm{Ra}^{-1} + O(\omega\mathrm{Ra}^{-3/2}, \omega^2\mathrm{Ra}^{-3/2}).\end{aligned} \tag{7.53}$$

Note that ω does not appear at leading order in this expansion. We again see the crossover to the high-ω limit when $\sqrt{\mathrm{Ra}} \sim \omega\mathrm{Ra}^{-1/2}$, so that the first and fourth terms are of the same order.

7.4.3 Bound in terms of M

The use of $\langle f^2\rangle$ and $\langle f\rangle$ in (7.43) is more general than the approach of Marchioro (1994), but the resulting bound is more complicated. We can obtain a simpler result by bounding a using $\langle f^2\rangle \leq M^2$ and $|\langle f\rangle| \leq M$, and using the resulting bound on a in (7.43), since the form of (7.43) means that it is satisfied when a is replaced by an upper bound. The result is simpler but less precise, and takes the form

$$\begin{aligned}\frac{\|\nabla T\|_2^2}{A} \leq &\frac{(M+1)^2}{\delta} + 2M - 1 + \left(\frac{8}{15}\right)^2\omega^2\delta^3 \\ &+ \frac{4\sqrt{2}\omega\delta^{3/2}}{15}\left(2\left(\frac{8}{15}\right)^2\omega^2\delta^3 + 8\left(\frac{(M+1)^2}{\delta} + 2M - 1\right)\right)^{1/2}.\end{aligned} \tag{7.54}$$

7.4.4 Examples

We now consider specific example profiles. When the average temperature at the top and bottom is different, one can define ΔT to be the difference in average temperature, which is the usual approach in steady Rayleigh–Bénard convection. For example, we can consider the sinusoidal profile $f_*(t_*) = \Delta T_0 + \Delta T_1 \cos\omega_* t_*$. For this case we choose to define ΔT as ΔT_0, so that

$$f(t) = 1 + \alpha \cos(\omega_1 t), \tag{7.55}$$

with $\alpha = \Delta T_1/\Delta T_0$ and $\omega_1 = \omega_* d^2/\kappa$. For this profile, we have $M = 1 + \alpha$, $\omega = \alpha\omega_1$, $\langle f \rangle = 1$ and $\langle f^2 \rangle = 1 + \alpha^2/2$. For $\omega \gg \mathrm{Ra}$, the bound on temperature dissipation is (7.50) with the appropriate values of $\langle f \rangle$ and $\langle f^2 \rangle$. For any fixed ω_1 and small enough α so that $\omega \ll \mathrm{Ra}$, the bound for large Ra in (7.53) becomes

$$\frac{\|\nabla T\|_2^2}{A} \leq (1 + \alpha/2)(1 + \alpha^2/8)\sqrt{2}\sqrt{\mathrm{Ra}} - 3 + O(\omega \mathrm{Ra}^{-1/2}). \tag{7.56}$$

As $\alpha \to 0$ we recover a bound for the standard setup with no modulation, namely $\|\nabla T\|_2^2/A \leq \sqrt{2}\sqrt{\mathrm{Ra}} - 3$.

If instead we take the bottom boundary temperature to have the same mean as the top boundary temperature, then $\Delta T_0 = 0$. Hence we take $\Delta T = \Delta T_1$, the maximum of the difference between the top and bottom temperatures. This leads to $f(t) = \cos(\omega_1 t)$, with $M = 1$, $\omega = \omega_1$, $\langle f \rangle = 0$, and $\langle f^2 \rangle = 1/2$. As in the previous case, the bound on temperature dissipation for $\omega \gg \mathrm{Ra}$ is (7.50) with the appropriate values of $\langle f \rangle$ and $\langle f^2 \rangle$. For large Rayleigh numbers with $\omega \ll \mathrm{Ra}$, the bound (7.53) becomes

$$\frac{\|\nabla T\|_2^2}{A} \leq \frac{3}{4\sqrt{2}}\sqrt{\mathrm{Ra}} - 1 + O(\omega \mathrm{Ra}^{-1/2}). \tag{7.57}$$

7.5 Discussion

Using the background method, we have found a bound on the temperature dissipation rate for a Rayleigh–Bénard-like setup with a modulated bottom boundary. We have investigated the bound for large Ra and ω, and we have considered specific simple examples of modulated temperature profiles.

The resulting bound is expressed in terms of the maximum of the temperature on the boundary, M, as well as its maximum rate of change, ω, mean, $\langle f \rangle$ and mean square, $\langle f^2 \rangle$. The spectral constraint must be satisfied at all times, so that it involves M, which hence is present in the bound. However, the inequalities used to obtain the final bound itself use the mean and mean square, resulting in a sharper bound than using M alone.

The calculation of the bound may also be carried out with an additional boundary layer of thickness δ at the top. If the interior profile for $\tau(z,t)$ is chosen simply as z to make $(\partial_z \tau - 1)$ equal zero, then it turns out that $\delta_{\max}$ is the same as in the single boundary layer case. The only difference in (7.47) is that F now becomes $F = \langle f^2 \rangle + 1$. When $\langle f \rangle = 0$, there is therefore no difference between using one or two boundary layers in the background profile. For the example with different average temperatures, this leads to an improvement in the small-α limit of the prefactor with $\|\nabla T\|_2^2 / A \leq \sqrt{\mathrm{Ra}/2} - 3$.

The Nusselt number, which is the ratio of the total to conductive heat transfer, is commonly used as the quantity to bound in convection problems in Rayleigh–Bénard convection, because with no time dependence the Nusselt number is proportional to the temperature dissipation, meaning that the bound on temperature dissipation yields a bound on heat transport. The time dependence in more complicated problems, such as the one considered here, makes the relationship between the Nusselt number and the temperature dissipation more complicated, and therefore the Nusselt number is not as useful in these cases as the temperature dissipation. The latter appears naturally in the bounding process. Furthermore, the temperature dissipation can be shown to be directly proportional to entropy production from heat conduction under the Boussinesq approximation, as discussed in Howard (1963) and also more recently in the context of horizontal convection in Rocha et al. (2020).

Besides the background flow technique, more recent bounding methods include polynomial sum-of-squares, as reviewed in Chernyshenko et al. (2014), and the auxiliary functional method, as applied in Fantuzzi (2018) to fixed-flux convection with free-slip conditions. These other methods have the potential for finding better bounds, while generally reducing to the background flow technique if certain parameter choices are made.

7.6 Inequalities

We make use of the following inequalities:

$$\left| \int_A w\theta \, \mathrm{d}A \right| \leq z \left\| \partial_z w \right\|_2 \left\| \partial_z \theta \right\|_2 \tag{7.58}$$

$$\left| \int_V \theta \partial_t \tau \, \mathrm{d}V \right| \leq \frac{4}{15} \omega \delta^{3/2} \sqrt{A} \left\| \nabla \theta \right\|_2 \tag{7.59}$$

$$\langle \left\| \nabla \theta \right\|_2 \rangle \leq \langle \left\| \nabla \theta \right\|_2^2 \rangle^{1/2} \tag{7.60}$$

$$\left\| \nabla \theta \right\|_2^2 \leq 2 \left\| \nabla T \right\|_2^2 + 2 \left\| \partial_z \tau \right\|_2^2 \tag{7.61}$$

$$\left\| \partial_z w \right\|_2^2 \leq \frac{1}{4} \left\| \nabla \boldsymbol{u} \right\|_2^2 \tag{7.62}$$

(7.58) is a consequence of the fundamental theorem of calculus, the Cauchy–Schwarz inequality, extending the domain of integration and the definition of the two-norm, in that order. It also holds with z replaced by $1 - z$. Inequality (7.59) is equivalent to (19) in Marchioro (1994), but with the prefactor improved from 1/2 to 4/15. Jensen's inequality leads to (7.60), while (7.61) is obtained using Young's inequality or the AMGM (arithmetic mean–geometric mean) inequality. A derivation of (7.62) can be found in Doering and Constantin (1996), equations (5.13)–(5.16).

7.7 Two boundary layers

Here we further discuss the use of two boundary layers to find a bound. An example background profile is shown in Figure 7.1. For simplicity, we take the additional boundary

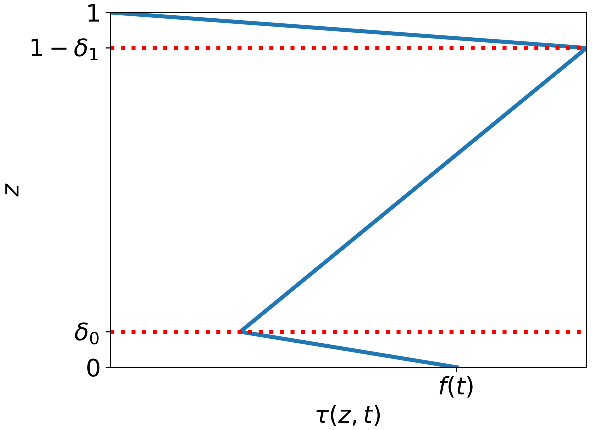

Figure 7.1: Background profile with two boundary layers.

layer to have the same thickness as the original boundary layer. If the interior profile for $\tau(z,t)$ is chosen simply as z to make $(\partial_z\tau - 1)$ equal zero, the profile is

$$\tau(z,t) = \begin{cases} z\left(\frac{\delta - f(t)}{\delta}\right) + f(t) & 0 \leq z \leq \delta \\ z & \delta \leq z \leq 1-\delta \\ \frac{(1-z)(1-\delta)}{\delta} & 1-\delta \leq z \leq 1. \end{cases} \tag{7.63}$$

Enforcing the spectral constraint leads to the same restrictions on η and δ as in (7.37), so that $\delta_{\max}$ is the same as in the single boundary layer case.

The additional boundary layer only makes a difference in the bound through $\|\partial_z\tau\|_2^2$, which appears as a in the bound (7.43). Calculating $\langle\|\partial_z\tau\|_2^2\rangle$ leads to

$$\langle\|\partial_z\tau\|_2\rangle = \frac{\langle f^2\rangle + 1}{\delta} - 2\langle f\rangle - 1 \tag{7.64}$$

Comparing with (7.45) and the previous definition of F shows that for two boundary layers we simply redefine F as

$$F = \begin{cases} \langle f^2 \rangle + 2\langle f \rangle + 1 & \text{1BL} \\ \langle f^2 \rangle + 1 & \text{2BL.} \end{cases} \tag{7.65}$$

If $\langle f \rangle = 0$, there is therefore no difference between using one or two boundary layers in the background profile. For the example with different average temperatures, so that $\langle f \rangle \neq 0$, using two boundary layers leads to an improvement in the small-α limit of the prefactor with $\|\nabla T\|_2^2 / A \leq \sqrt{\mathrm{Ra}/2} - 3$. The one and two boundary layer cases are compared in Figure 7.2, which shows the bounds for the example with different average temperatures where $f(t)$ is defined in (7.55) with $\alpha = 0.1$. There are two clear regimes in the figure corresponding to the limits $\omega \ll \mathrm{Ra}$ and $\omega \gg \mathrm{Ra}$. We expect the transition point between the limits to occur when the optimal δ becomes $\delta_{\max}$, which from (7.51) is

$$\omega \approx 0.02(2+\alpha)^2 F^{1/2} \mathrm{Ra}. \tag{7.66}$$

For $\mathrm{Ra} = 10^4$, as shown in figure 7.2 the transition point is expected to be at $\omega \approx 1700$ for one boundary layer and $\omega \approx 1200$ for two boundary layers, which both correspond with the transition points seen in the figure.

7.8 Relationship of Nu to $\langle \|\nabla T\|_2^2 \rangle$

The Nusselt number is

$$\mathrm{Nu} = 1 + \frac{\langle J \rangle}{\langle f(t) \rangle A}, \tag{7.67}$$

where

$$J = \int_V wT \mathrm{d}V. \tag{7.68}$$

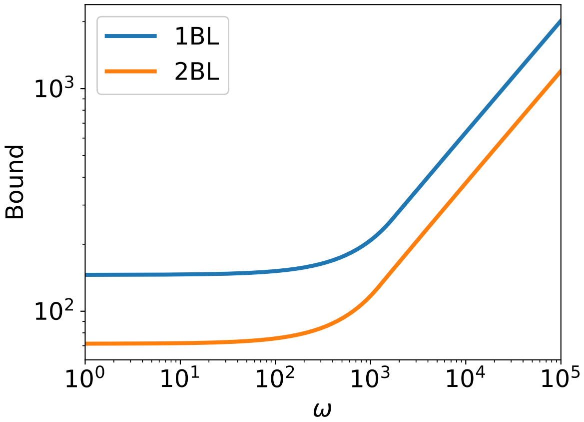

Figure 7.2: Comparison of bound with one and two boundary layers at $\mathrm{Ra} = 10^4$ with $f(t)$ defined as in (7.55) and $\alpha = 0.1$.

We would like to trade $\langle J \rangle$ for the temperature dissipation rate. To do this, we first find

$$\frac{\mathrm{d}(zT)}{\mathrm{d}t} = wT + \nabla \cdot (z\nabla T) - \partial_z T. \tag{7.69}$$

Integrating over the volume, averaging over time, and assuming the volume integral of zT is finite leads to

$$\left\langle \int_V wT\mathrm{d}V \right\rangle = -\langle f(t)\rangle A - \left\langle \int_{A_{\mathrm{top}}} \partial_z T\mathrm{d}A \right\rangle. \tag{7.70}$$

From the temperature equation power integral we have

$$\frac{1}{2}\frac{\mathrm{d}}{\mathrm{d}t}\|T\|_2^2 = \int_S T\nabla T \cdot \mathbf{d}\boldsymbol{S} - \|\nabla T\|_2^2 \tag{7.71}$$

Only one term survives in the surface integral, and taking a time average of the result leads to

$$\langle \|\nabla T\|_2^2 \rangle = -\left\langle \int_{A_{\mathrm{bot}}} f(t)\partial_z T\mathrm{d}A \right\rangle \tag{7.72}$$

It is unclear how to use this in a bounding argument for general f. For f constant, this can be related to the above expressions to derive a relation between Nu and $\langle \|\nabla T\|_2^2 \rangle$. For a statistically stationary flow, the heat in the bottom must equal the heat out the top, and therefore

$$\left\langle \int_{A_{\mathrm{bot}}} \partial_z T \mathrm{d}A \right\rangle = \left\langle \int_{A_{\mathrm{top}}} \partial_z T \mathrm{d}A \right\rangle . \tag{7.73}$$

This allows us to combine (7.70) and (7.72) with $f = 1$ to find

$$\langle \|\nabla T\|_2^2 \rangle = \left\langle \int_V wT \mathrm{d}V \right\rangle + A. \tag{7.74}$$

Recalling the definition of Nu in (7.67), we find that

$$\frac{\langle \|\nabla T\|_2^2 \rangle}{A} = \mathrm{Nu}. \tag{7.75}$$

7.9 Anti-turbulence

In Paparella and Young (2002), the authors prove what they call the anti-turbulence theorem for horizontal convection. The name stems from the law of finite energy dissipation in Frisch (1995), which states that for a flow to be turbulent, the energy dissipation per unit mass must tend to a finite limit even as the viscosity tends to zero. Anti-turbulence is said to occur when the law of finite energy dissipation is violated, meaning the energy dissipation goes to zero along with the viscosity. In this section, we will show that the anti-turbulence argument also applies to zero-mean modulated convection.

We start from the dimensional equations (7.1)–(7.3), set $b = \alpha g T_*$ for ease of comparison with Paparella and Young (2002), and drop the asterisks with the understanding that all variables are still dimensional. This gives us

$$\partial_t \boldsymbol{u} + \boldsymbol{u} \cdot \nabla \boldsymbol{u} = -\frac{1}{\rho_0} \nabla p + b\hat{\boldsymbol{z}} + \nu \nabla^2 \boldsymbol{u}, \tag{7.76}$$

$$\nabla \cdot \boldsymbol{u} = 0, \tag{7.77}$$

$$\partial_t b + \boldsymbol{u} \cdot \nabla b = \kappa \nabla^2 b, \tag{7.78}$$

Taking the inner product of (7.76) with the velocity, integrating over the entire volume, and taking a time average leads to

$$\left\langle \int_V wb \, \mathrm{d}V \right\rangle = \nu \left\langle \|\nabla \boldsymbol{u}\|_2^2 \right\rangle, \tag{7.79}$$

Now we use (7.78) to find another expression for $\langle \int_V wb \mathrm{d}V \rangle$. Taking a time average of (7.78) and using the divergence theorem leads to

$$\left\langle \int_S b\boldsymbol{u} \cdot \mathbf{d}\boldsymbol{S} \right\rangle = \kappa \left\langle \int_S \nabla b \cdot \mathbf{d}\boldsymbol{S} \right\rangle. \tag{7.80}$$

We take the volume enclosed by these surfaces to be the fluid between the top surface, a surface at height z, and four side surfaces perpendicular to the horizontal directions. Assuming periodicity or no-flux/no-penetration conditions in the horizontal directions, only the surfaces perpendicular to the vertical survive from this equation, and we have

$$\left\langle \int_{A(d)} bw \, \mathrm{d}A \right\rangle - \left\langle \int_{A(z)} bw \, \mathrm{d}A \right\rangle = \kappa \left\langle \int_{A(d)} \partial_z b \, \mathrm{d}A \right\rangle - \kappa \left\langle \int_{A(z)} \partial_z b \, \mathrm{d}A \right\rangle. \tag{7.81}$$

No penetration of fluid through the top eliminates the $A(d)$ integral on the left-hand side, and a no-flux condition at the top eliminates the $A(d)$ integral on the right. We then have

$$\left\langle \int_{A(z)} (bw - \kappa \partial_z b) \, \mathrm{d}A \right\rangle = 0. \tag{7.82}$$

This shows that the time-averaged net heat flux through any horizontal surface in the domain is zero.

We now find another expression for the total volume integral of wb to go along with that in (7.79) by integrating (7.82) in z from the bottom to the top, resulting in

$$\left\langle \int_V bw \, \mathrm{d}V \right\rangle = \kappa \left\langle \int_{A(d)} b \, \mathrm{d}A \right\rangle - \kappa \left\langle \int_{A(0)} b \, \mathrm{d}A \right\rangle . \tag{7.83}$$

Eliminating the wb term between (7.79) and (7.83) leads to

$$\nu \left\langle \|\nabla \boldsymbol{u}\|_2^2 \right\rangle = \kappa \left\langle \int_A (b(d) - b(0)) \, \mathrm{d}A \right\rangle . \tag{7.84}$$

Physically, we assume that the time average of the average buoyancy difference between the top and bottom is bounded. We therefore bound the right-hand side of (7.84) with

$$\kappa \left\langle \int_A (b(d) - b(0)) \, \mathrm{d}A \right\rangle \leq \kappa A (b_{\max} - b_{\min}), \tag{7.85}$$

Letting $b_0 \equiv b_{\max} - b_{\min}$, we then have

$$\nu \left\langle \|\nabla \boldsymbol{u}\|_2^2 \right\rangle \leq \kappa b_0 A. \tag{7.86}$$

The energy dissipation per unit time and mass is defined as

$$\varepsilon \equiv \frac{\nu}{V} \left\langle \|\nabla \boldsymbol{u}\|_2^2 \right\rangle , \tag{7.87}$$

so we divide (7.86) by the volume, V, to find

$$\varepsilon \leq \frac{\kappa b_0}{d} . \tag{7.88}$$

Letting $\kappa \to 0$ shows that the energy dissipation also goes to zero in this limit, violating the law of finite energy dissipation. We can also use $\mathrm{Pr} = \nu/\kappa$ and let ν and κ both go to zero while Pr tends to a finite constant, and in this case as well the law of finite energy dissipation is violated. Hence we conclude that RB convection with zero-mean temperature modulation at one boundary and a no-flux condition at the other is anti-turbulent.

Chapter 7, in part, has been published in *Physical Review Fluids*, "Bounding temperature dissipation in time-modulated Rayleigh Bénard convection" by T. W. Christopher and S. G. Llewellyn Smith, 2021, **6**, L051501 (American Physical Society). The dissertation author was the primary investigator and author of this material.

Chapter 8

Conclusion

In this dissertation, we have considered the fundamental fluid dynamics scenario of convection between two surfaces with time-modulated heating either at the boundary or in the bulk of the fluid through radiative heating. The modulation profile is generally taken as one in which the mean of the heat flux or temperature difference between the surfaces is zero, which we call zero-mean modulation, and which has not received as much attention as nonzero-mean modulation in the literature. The different facets of convection dealt with have been linear stability, nonlinear stability, and bounding of flow quantities. Here we summarize the results from each line of investigation, and we finish by discussing the application of these results and potential future work.

For linear stability, we have found critical Rayleigh numbers for setups with modulated boundary temperature, modulated boundary heat flux, and modulated radiative heating. Our analysis led to the key parameter of the nondimensional frequency ω, which compares the Stokes layer depth to the liquid depth, or equivalently the time scale from diffusion to the time scale of the forcing frequency. In general, a higher nondimensional frequency leads to a larger critical Rayleigh number, though at lower frequencies, the critical Rayleigh number increases non-monotonically with increasing frequency, with the critical disturbance alternating between being synchronous and subharmonic.

At a certain $O(10)$ frequency for each case considered, the disturbance at the critical threshold ceases switching and remains subharmonic for all higher frequencies. At this point, an asymptotic balance is found between the critical Rayleigh number and the frequency such that an appropriate combination of the two approaches a constant value at higher frequencies, with the specific combination depending on the type of heating under consideration.

This high-frequency regime can also be accessed mathematically by considering a semi-infinite domain. The results found from the semi-infinite domain agree with the results from the finite domain with high forcing frequency. We also address modulated radiative heating in a semi-infinite domain, specifically investigating what happens to the critical Rayleigh number as the penetration depth of the radiative heating is decreased towards zero. We find that the modulated heat flux results are recaptured.

The low frequency limit also proves interesting in the linear stability analysis. As opposed to the high-frequency limit, which becomes easier numerically, the low-frequency limit becomes much more difficult numerically, becoming too ill-conditioned to find results below a certain $O(1)$ frequency. We make progress below that frequency using a WKB approximation, though only in the case of symmetric no-stress boundary conditions with temperature modulation can the analysis be carried out in full. For other conditions, we have derived the appropriate WKB solutions without being able to continue them through turning points, and therefore without being able to find linear stability thresholds.

For nonlinear stability, we have found critical Rayleigh numbers for setups with modulated boundary temperature and heat flux. Two types of nonlinear stability are considered, asymptotic and global. For all cases studied, the thresholds for nonlinear stability fall below the linear stability threshold. This means that the potential for subcritical instabilities exists. While the window of Rayleigh numbers that could create a subcritical instability is small at low frequencies with an $O(1)$ Prandtl number, at very high frequencies the window grows very large, as it also does at very low Prandtl numbers with a fixed frequency.

The nonlinear stability results do not indicate noticeable low and high frequency regimes. At high frequencies, a specific balance between the critical Rayleigh number and frequencies is expected to emerge, as it does in the linear stability results. The balance is the ratio between the Rayleigh number and frequency that appears naturally in the consideration of a semi-infinite domain. This balance does not emerge in the nonlinear stability results, indicating that the scaled critical Rayleigh numbers for nonlinear stability go to zero in the high-frequency/deep-water limit.

For bounding of flow quantities, we have used the background method to derive the first exact mathematical bound on temperature dissipation in modulated convection. The specific setup investigated has a boundary temperature that can vary arbitrarily in time, and we have also looked at the form the bound takes for specific example profiles. For fixed frequency with the Rayleigh number much larger than the frequency, the bound grows with the square root of the Rayleigh number. For fixed Rayleigh number with the frequency much larger than the Rayleigh number, the bound grows with the square root of the frequency. The specific factors in the bound depend on properties of the modulation profile.

8.1 Applications and Future Work

The inspiration for this study was lake convection, and that is also the main application envisioned. The stability results all indicate that conditions at Lake Superior during springtime warming place the lake solidly above all Rayleigh number stability thresholds. Though the lake is likely to be well above the stability threshold, the critical wavenumbers at instability might provide a length scale for the resulting instability. Future work could include an investigation of the flow just beyond stability, though even in that case the results may not apply to a situation with a Rayleigh number far above the critical Rayleigh number.

Throughout the dissertation, we have used a cosine modulation profile. Daily heating from the sun clearly results in a more complicated heating profile at the surface of a lake, and future work could take a specific profile and expand it in a Fourier series to easily incorporate it into the analysis we have performed here. A more realistic heating profile tailored to measurements could be used in place of the simple cosine used here.

Complication arises if a modulation profile is used that leads to a net input or output of heat, and therefore a base state temperature whose mean over one period changes from period to period. It would likely be possible to account for this growth or decay with a linearly growing or decaying term in the base state, but care would have to be taken to check that the fluid would not change its state or properties drastically before transient terms became unimportant enough to be ignored.

In the low frequency regime, the linear stability calculation as carried out in this dissertation becomes numerically difficult. For this reason, we have carried out an asymptotic analysis using the WKB method, but we were only able to find results with this method for the case of symmetric no-slip boundary conditions with temperature modulation. For all other cases, a matrix WKB problem results, and it was not clear how to connect solutions through turning points, meaning we could not find linear stability results. Future work on the matrix WKB method building off of Wasow (1985) could lead to success for these more difficult cases.

Though rotation has been discussed, we have not included rotation in the calculations in this dissertation. It is possible that rotation plays an important role in the formation of convection in the lake. In that case, the stability threshold would likely be higher, as that is the effect rotation has in standard RB, but only future work incorporating rotation could show the exact effects of rotation on stability. Incorporating rotation into the linear stability analysis is straightforward conceptually and analytically, but the resulting numerical problem does not yield solutions with the numerical methods used in this dissertation. Future work on adjusting the numerical methods to lead to better-conditioned numerical problems could allow rotation to be successfully treated in the linear stability analysis.

Incorporating rotation into the nonlinear stability analysis is fraught with difficulties from the very beginning. The standard energy used in the energy method is blind to rotation. Only by using a more complicated energy can one hope to capture the effects of rotation. In the literature to date, all methods using a more complicated energy appear to have to settle for conditional stability results dependent on the size of the initial energy rather than being able to find unconditional nonlinear stability results like those in this dissertation. This is discussed in Straughan (2013). Until an appropriate energy is found for steady RB with rotation, it will likely be difficult to treat time-modulated convection with rotation.

The bound found on temperature dissipation applies to a configuration with surface temperature modulation. Future work includes carrying out the bound analysis for configurations with surface heat flux modulation and radiative heating modulation. Because temperature dissipation is not an easy quantity to measure, establishing a clearer connection between the temperature dissipation and the Nusselt number in modulated scenarios would make comparison with experiments and observations easier. Internally heated convection has received attention in the bounding literature, (for example in Lu, Doering, and Busse (2004), Goluskin (2016), and Arslan et al. (2021)), and methods such as those used in Arslan et al. (2021), in which the background method with a quadratic auxiliary function is used, might also work for modulated radiative heating.

Appendix A

Hollow Vortex in a Corner

A.1 Introduction

A point vortex in a corner in the presence of a straining flow will move in a periodic orbit Suh (1993). In particular there is an equilibrium position at which it will remain at rest. A special case of this behaviour is that of a point vortex moving parallel to a straight boundary. This solution was generalized to the case of a hollow vortex by Pocklington (1894). Pocklington's hollow vortex solution was expressed in terms of the Schottky–Klein (hereafter SK) prime function Crowdy, Llewellyn Smith, and Freilich (2013), opening the way to further generalizations. The present work uses the SK prime function to extend the previous results to find equilibrium solutions for a hollow vortex in a corner.

The standard conformal mapping approach for free boundary value problems in inviscid flow that goes back to Michell (1890) is used to find the shape of the hollow vortex. Conformal maps are constructed between the corner, a half-plane, and a concentric annulus as shown in figure A.1. An image vortex in the non-physical portion of the half plane allows the boundary condition of no normal flow on the solid walls to be satisfied. The boundaries of the hollow vortex and its image correspond to circles in the annulus.

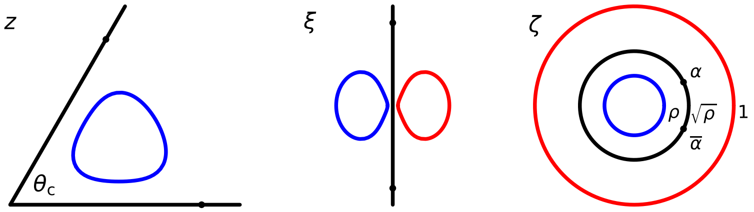

Figure A.1: (*a*) The physical z-plane with the corner; (*b*) the auxiliary ξ-plane; (*c*) the ζ-plane containing the annulus. (Here $\rho = 0.3$ and $\theta_c = \pi/3$; stagnation points along the wall are denoted by black circles.)

A.2 Problem formulation

A sketch of the physical domain is shown in figure A.1(*a*). We consider flow inside a corner with interior angle θ_c. The fluid lies between a solid wall along positive x and a solid wall making the angle θ_c with the positive real axis. We have $0 < \theta_c < 2\pi$; the case $\theta_c = \pi$ recovers the Pocklington dipole.

A hollow vortex is a steady-state constant-pressure region of finite area with non-zero circulation around it. The boundary of a hollow vortex is a streamline. For two-dimensional inviscid, incompressible, irrotational flow, Bernoulli's equation on the boundary gives

$$p + \frac{|\boldsymbol{u}|^2}{2} = \text{constant}. \tag{A.1}$$

The pressure on the hollow vortex boundary is constant, and therefore Bernoulli's equation shows that the speed of the flow must be constant on the boundary as well. This shows that the boundary of a hollow vortex is a vortex sheet, and hollow vortices can be thought of as steady vortex sheets. As this is a two-dimensional incompressible and irrotational flow, the solution can be written in terms of a complex potential, w, with a corresponding complex velocity $\mathrm{d}w/\mathrm{d}z$.

The flow describing a stationary point vortex in a corner gives insight into the hollow vortex solution, because as the area of a hollow vortex goes to zero the point vortex

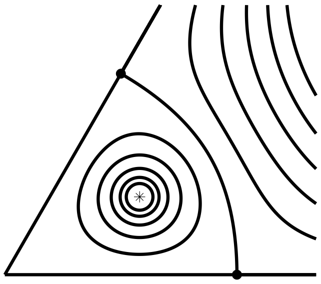

Figure A.2: Streamlines for a point vortex in equilibrium in a corner. The point vortex is denoted by an asterisk. The two stagnation points of the flow on the walls are denoted by filled circles. The speed of the flow is also zero at the origin.

flow field should be recovered. In particular the flow for a hollow vortex in a corner is therefore expected to have the same number of stagnation points as a point vortex in a corner. Furthermore, the flow far away from the hollow vortex must be the same as the flow far away from the point vortex. Streamlines for a point vortex in equilibrium in a corner are shown in figure A.2, where it can be seen that the flow has three stagnation points: one at the origin and one on each boundary. Note that the flow is self-similar: one can rescale using the distance from the corner to the stagnation points as a unit of length, and then there is a unique flow.

The complex potential for a point vortex in a corner is found using conformal mapping and the method of images and is

$$w_{\mathrm{pv}}(z) = \frac{\Gamma}{2\pi \mathrm{i}}[\log{(z^{\pi/\theta_c} - z_0^{\pi/\theta_c})} - \log{(z^{\pi/\theta_c} - \bar{z}_0{}^{\pi/\theta_c})}] - Sz^{\pi/\theta_c}, \tag{A.2}$$

where S is a real number with the same sign as Γ that describes the strength of the background generalized straining flow and z_0 is the position of the vortex. The potential (A.2) behaves like $-Sz^c$ for large $|z|$, where $c = \pi/\theta_c$. This behavior will also hold for the hollow vortex. The condition for the vortex to be stationary comes from requiring $\dot{z}_0 = 0$, where

$$\dot{z}_0 = \frac{\Gamma}{2\pi\mathrm{i}}\left[\frac{c-1}{2z_0} - \frac{cz_0^{c-1}}{z_0^c - \bar{z}_0{}^c}\right] - Scz_0^{c-1}. \tag{A.3}$$

The result is $z_0 = (\mathrm{i}\Gamma/4\pi Sc)^{1/c}$, so that z_0 is along the bisector of the corner (when $\pi = \theta_c$ the position parallel to the boundary is arbitrary and can be taken to be on the y-axis).

A.3 Conformal mapping

The solution for the hollow vortex is constructed using conformal maps between the three planes shown in figure A.1. The physical z-plane (a) is related to the ξ-plane (b) via

$$z = f(\xi) = (-\mathrm{i}\xi)^{\theta_c/\pi}, \tag{A.4}$$

where θ_c is the interior angle of the corner. The function $f(\xi)$ has a branch point at the origin, and its branch cut is taken to be in the right half-plane, i.e. outside the physical domain. The ξ-plane is essentially the same as the physical plane in Crowdy, Llewellyn Smith, and Freilich (2013). An extension of the Riemann Mapping Theorem shows that any doubly connected domain can be mapped onto a concentric annulus. We take g to be the unknown map from the circular annulus $\rho < |\zeta| < 1$ in the ζ-plane (c) to the ξ-plane with the interiors of the vortex and of its unphysical image removed. The flow region will correspond to the region $\rho < |\zeta| < \beta$, where β will be found. The map from the annulus to the corner is written as $h(\zeta) = f(g(\zeta))$.

In terms of the variable ζ, we write the complex potential describing the flow around the hollow vortex in the corner as $W(\zeta)$ and the complex velocity in the physical z-plane as $\mathrm{d}w/\mathrm{d}z = R(\zeta)$.

We require the map g to be one-to-one, and take the point at infinity in the ξ-plane to correspond to the simple pole β in the ζ-plane. Hence

$$g(\zeta) = \frac{b}{\zeta - \beta} + \cdots \tag{A.5}$$

near $\zeta = \beta$, where b is chosen to be a positive real number. This means that the inner circle $|\zeta| = \rho$ maps to the image of the vortex boundary in the left half-plane in ξ, while the circle $|\zeta| = \beta$ maps to the imaginary axis in the ξ-plane. The outer circle $|\zeta| = 1$ maps to the reflection of the vortex boundary image about the imaginary ξ-axis, which is not in the physical domain.

From the above, we see that the complex potential $W(\zeta)$ satisfies the following conditions. The kinematic boundary condition requires Im $W(\zeta)$ to be constant on the boundaries and on the vortex boundary. The circulation of the vortex, which is the change in the multivalued function $W(\zeta)$ around the vortex, is Γ. Large $|z|$ corresponds to large $|\xi|$, so that

$$W(\zeta) \sim -Sz^{\pi/\theta_c} = \mathrm{i}S\xi \sim \frac{\mathrm{i}Sb}{\zeta - \beta} \tag{A.6}$$

near $\zeta = \beta$.

In turn, the complex velocity, $\mathrm{d}w/\mathrm{d}z = R(\zeta)$, satisfies the following conditions. From differentiating the asymptotic conditions of the complex potential in the physical plane, we have

$$R(\zeta) \sim -\frac{S\pi}{\theta_c}\left(\frac{-\mathrm{i}b}{\zeta - \beta}\right)^{1-\theta_c/\pi} \tag{A.7}$$

near $\zeta = \beta$. The hollow vortex property of constant speed on the boundary from (A.1) leads to $|R(\zeta)| = q_0$ on the vortex boundary. Finally $R(\zeta) = 0$ at the two stagnation points. Its behaviour near the origin depends on the angle: it vanishes for $0 < \theta_c < \pi$, it is finite for $\theta_c = \pi$, and it has an algebraic singularity for $\pi < \theta_c < 2\pi$.

We seek a hollow vortex that is symmetric about the real and imaginary axes in the ξ-plane. These symmetries should persist in the $\zeta-$plane, and we now use them to determine which points in ζ correspond to the important points in z: the origin, infinity, and the stagnation points.

In the ξ-plane, the vortex boundaries are symmetric under reflection about the vertical axis. In the annulus, the boundaries are concentric circles, and mapping them onto each other is carried out by inversion. Hence to retain the symmetry of the vortex, the vortex boundaries should be inverse circles about the image of the axis in the annulus. The boundary circles have radii ρ and 1, so the axis between the vortices in the ξ-plane must correspond to a circle with radius $\beta \equiv \sqrt{\rho}$ inside the annulus. The stagnation points are on this circle.

In the ξ-plane, the vortex boundaries are also symmetric about the real axis which runs through the centroids of the vortices. From (A.4) we map the real ξ-axis to the real axis in the ζ-plane. The images of the ξ-axes meet at 0 and ∞, and these map to $-\beta$ and β respectively in the ζ-plane. The two stagnation points on the walls are complex conjugates of each other in the annulus, so that we can write them as α and $\bar{\alpha}$ with $|\alpha| = \beta$.

A.4 Solution

A.4.1 Complex potential and complex velocity

The conformal mapping solution is constructed using the SK prime function. SK prime functions exists for higher connectivity domains (i.e. with larger genus). For genus 2, i.e. the annulus, the SK prime function can be written explicitly as Crowdy (2020)

$$\omega(\zeta, a) = (\zeta - a) \prod_{k=1}^{\infty} \frac{(1 - \rho^{2k}\zeta/a)(1 - \rho^{2k}a/\zeta)}{(1 - \rho^{2k})}, \tag{A.8}$$

where ζ lies inside the annulus, $0 \leq \rho \leq 1$, and a can be any complex number. For the annulus, the following prime function identities hold:

$$\omega(\zeta, a) = -\zeta a \omega(1/\bar{\bar{\zeta}}, 1/\bar{a}) \qquad \omega(\rho^2 \zeta, a) = -\frac{a}{\zeta}\omega(\zeta, a). \tag{A.9}$$

The conditions on the conformal map $W(\zeta)$ characterize it as a map that takes circular vortex boundaries in ζ to horizontal lines in W. This type of map is called a parallel slit map, and can be written using the SK prime function as

$$\phi_\theta(\zeta, a) = \left(\frac{\partial}{\partial a} - \mathrm{e}^{2\mathrm{i}\theta}\frac{\partial}{\partial \bar{a}}\right)\log\left(\frac{\omega(\zeta, a)}{|a|\omega(\zeta, 1/\bar{a})}\right) \tag{A.10}$$

The map $\phi_\theta(\zeta, a)$ takes concentric circles in the annulus to parallel lines making an angle θ with the real axis, with a simple pole at $\zeta = a$. This allows us to write the complex potential as

$$W(\zeta) = D\mathrm{e}^{-\mathrm{i}\theta_p}\phi_{\theta_p}(\zeta, \beta) + \frac{\Gamma}{2\pi\mathrm{i}}\log\zeta. \tag{A.11}$$

The form of the parallel slit map ensures that W has constant imaginary part along the images of the vortex boundaries as long as D is real and θ_p is $\pi/2$. The logarithm term ensures the correct circulation. It does not affect the kinematic boundary condition, since the logarithmic term has constant imaginary part on constant $|\zeta|$. The potential (A.11) is the same as that in Crowdy, Llewellyn Smith, and Freilich (2013) and does not depend on the angle θ_c. The relations between the notation used in Crowdy, Llewellyn Smith, and Freilich (2013) and that used here are discussed in A.8.

Starting with the prime function product representation in (A.8) and carrying out the operations in the definition of a parallel slit map in (A.10), the parallel slit map for the present domain can be written as

$$\begin{aligned}\phi_\theta(\zeta,a) = &-\frac{1}{\zeta-a}+\sum_{k=1}^{\infty}\left(\frac{\rho^{2k}\zeta}{a^2(1-\rho^{2k}\zeta/a)}-\frac{\rho^{2k}/\zeta}{1-\rho^{2k}a/\zeta}\right)+\frac{1}{2}\left(\frac{a\mathrm{e}^{\mathrm{i}2\theta}-\bar{a}}{|a|^2}\right)\\ &+\frac{\mathrm{e}^{\mathrm{i}2\theta}}{\bar{a}^2(\zeta-1/\bar{a})}-\frac{\mathrm{e}^{\mathrm{i}2\theta}}{\bar{a}^2}\sum_{k=1}^{\infty}\left(\frac{\bar{a}^2\rho^{2k}\zeta}{1-\rho^{2k}\zeta\bar{a}}-\frac{\rho^{2k}/\zeta}{1-\rho^{2k}/(\zeta\bar{a})}\right),\end{aligned} \tag{A.12}$$

showing that $\phi_\theta(\zeta,a)$ has a simple pole with residue -1 at $\zeta=a$. Condition (A.6) then implies that

$$D = Sb. \tag{A.13}$$

The constants S and b are both real, and θ_p is $\pi/2$. The zeros of $\mathrm{d}w/\mathrm{d}z$ are the same as those of $W'(\zeta)$. Hence $W'(\alpha)=0$, which leads to a relationship between the constants of the problem, which is same as (24) of Crowdy, Llewellyn Smith, and Freilich (2013).

The condition of constant speed, $|R(\zeta)|$, on the boundary of the vortex leads us to view $R(\zeta)$ as a conformal map that takes the circular vortex boundaries in ζ to circular arcs in R. This type of map is called a circular slit map, and can be written using the Schottky–Klein prime function as

$$w_a(\zeta) = \frac{\omega(\zeta,a)}{|a|\omega(\zeta,1/\bar{a})}, \tag{A.14}$$

which has a simple zero at $\zeta=a$ and a simple pole outside the domain at $\zeta=1/\bar{a}$.

This allows us to write the complex velocity as

$$R(\zeta) = \frac{A}{\zeta}w_\alpha(\zeta)w_{\bar{\alpha}}(\zeta)\left(\frac{w_{-\beta}(\zeta)}{w_\beta(\zeta)}\right)^{1-\theta_c/\pi}. \tag{A.15}$$

This function has zeros at the stagnation points and has the appropriate pole at $\zeta=\beta$ to satisfy the behavior in (A.7). Any power of ζ can be considered as a circular slit map because $|\zeta|$ is constant along arcs of constant radius. The complex velocity $R(\zeta)$

is therefore a product of circular slit maps, since each individual circular slit map has constant magnitude on the circular boundaries of the domain. The inverse power of ζ in (A.15) ensures that the speed on the two boundaries in the ξ-plane is the same as in Crowdy, Llewellyn Smith, and Freilich (2013); this is essentially the method of images. The branch cut is the same as discussed previously.

One can use the definition of the prime function in (A.8) to obtain an expression for A in terms of the other quantities from

$$R(\zeta) \sim \frac{A}{\beta} w_\alpha(\beta) w_{\bar{\alpha}}(\beta) \left(\frac{w_{-\beta}(\beta) \beta \omega(\beta, 1/\beta)}{(\zeta - \beta) \prod_{k=1}^{\infty} (1 - \rho^{2k})} \right)^{1-\theta_c/\pi} \tag{A.16}$$

as $\zeta \to \beta$. Using this in (A.7) gives

$$A = -\frac{S\pi\beta^{\theta_c/\pi}}{\theta_c w_\alpha(\beta) w_{\bar{\alpha}}(\beta)} \left(\frac{-\mathrm{i}a \prod_{k=1}^{\infty} (1 - \rho^{2k})}{w_{-\beta}(\beta) \omega(\beta, 1/\beta)} \right)^{1-\theta_c/\pi} . \tag{A.17}$$

The details of this expression are not needed below, because there is still an arbitrary scaling in the solution that will be determined *a posteriori*. It is useful however to note the argument of A above in the numerical calculations.

A.4.2 Determining parameters

For each angle θ_c, we expect a one-parameter family of solutions parameterized by ρ. We require the map to be single-valued, which means that

$$\int_C \frac{\mathrm{d}z}{\mathrm{d}\zeta} \mathrm{d}\zeta = 0, \tag{A.18}$$

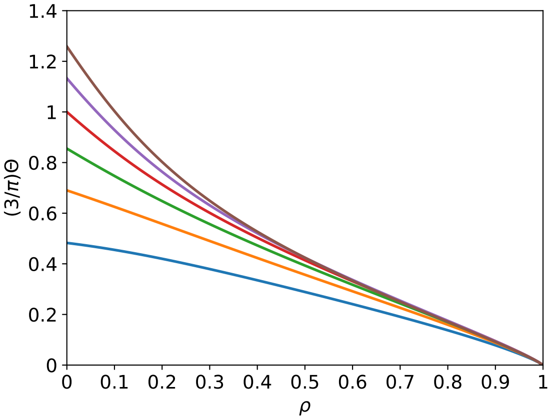

Figure A.3: Normalized stagnation point phase, $3\Theta/\pi$, as a function of ρ for $\theta_c = \pi/4$, $\pi/2$, $3\pi/2$, π, $5\pi/4$, and $3\pi/2$. Smaller values of θ_c correspond to smaller Θ.

where C is any closed loop in the domain. Note that the branch cuts lie outside the interior of the annulus with $\rho < |\zeta| < \beta$. We have

$$\frac{\mathrm{d}z}{\mathrm{d}\zeta} = \frac{\mathrm{d}W/\mathrm{d}\zeta}{R(\zeta)}, \tag{A.19}$$

where $\mathrm{d}W/\mathrm{d}\zeta$ can be obtained explicitly from (A.11). This leads to the relation

$$z(\zeta) = \int_{-\beta}^{\zeta} \frac{\mathrm{d}W/\mathrm{d}\zeta'}{R(\zeta')}\,\mathrm{d}\zeta'. \tag{A.20}$$

Given ρ and θ_c, we solve (A.18) to obtain Θ, the argument of the stagnation point α, as in Crowdy, Llewellyn Smith, and Freilich (2013). Results of Θ for a variety of corner angles are shown in figure A.3. In this and all subsequent figures, the values $\theta_c = \pi/4$, $\pi/2$, $3\pi/2$, π (the Pocklington dipole), $5\pi/4$, and $3\pi/2$ are used. One can show that

$$\Theta = \tan^{-1}\frac{\sqrt{4\theta_c\pi - \theta_c^2}}{2\pi - \theta_c} \tag{A.21}$$

for $\rho = 0$. The integrand in (A.18) is independent of the constants D and A.

This calculation leaves an undetermined parameter. This can be used to set the overall scale of the vortex. We choose it so that $|z(\alpha)| = 1$, so that the distance to the stagnation points is unity. Alternatively we can take the distance of the centroid of the vortex to the corner to be the unit of distance. As a result, the plots below do not have axes.

Once the condition (A.18) has been enforced, the boundary of the hollow vortex is found by evaluating (A.20) along the circle $|\zeta| = \rho$. We first integrated from $-\beta$ to $-\rho$ to move from the corner to the closest point of the vortex to the corner (which is along the bisector of the angle by symmetry). This integrand has an algebraic singularity at $\zeta = -\beta$, since $R(\zeta)$ is singular at a corner with $\pi < \theta_c < 2\pi$. The integral however can be carried out numerically with no trouble.

A.5 Results

Figure A.4 shows the boundaries of a number of stationary hollow vortex solutions for different values of ρ and different angles. The hollow vortices in each plot have been individually normalized so that the stagnation points are the same for all vortices. Figure A.5 shows the same solutions normalized so that their centroids are at unit distance from the corner. The point vortex solution is plotted as a filled circle in each figure. As $\rho \to 0$, the hollow vortex boundary shrinks to the point vortex, as expected. For $\theta_c > \pi$, the vortex boundary intersects itself for large enough ρ, as shown in figure A.6(b). This is similar to what happens for the hollow vortex in strain examined by Llewellyn Smith and Crowdy (2012), which self-intersects if the strain is too large.

A.6 Discussion

As shown in figure A.6(b), we find numerically that, as ρ increases for $\theta_c > \pi$, the vortex boundary ends up being tangent to itself at a point along the bisector of the

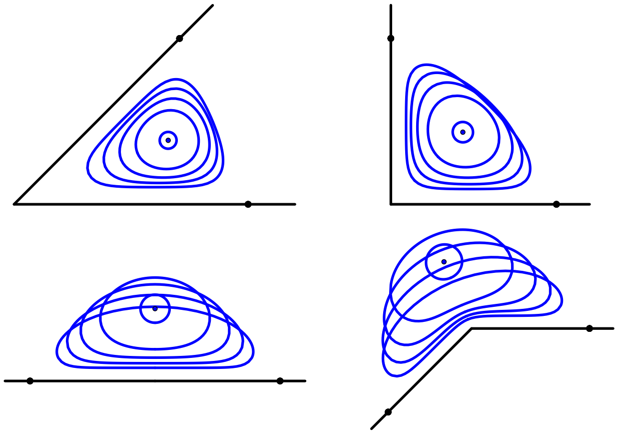

Figure A.4: The five vortices in each corner correspond to five equally spaced values of ρ in $0.01 \leq \rho \leq 0.5$. Each vortex is scaled individually so that the stagnation points are at distance unity from the corner.

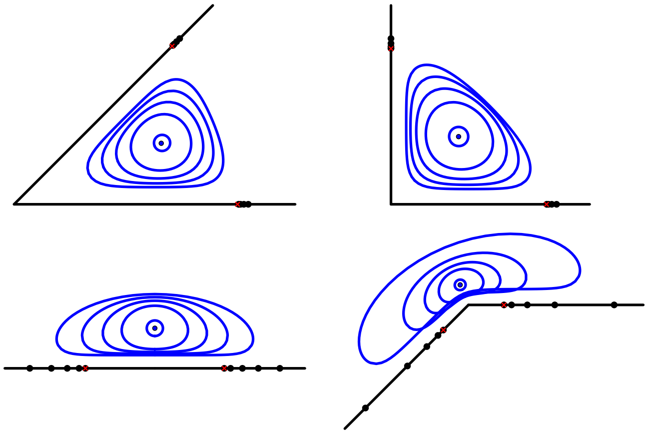

Figure A.5: As for figure A.4, but normalized so that the geometric centroid is at distance unity from the corner. The stagnation points of the point vortex are in red.

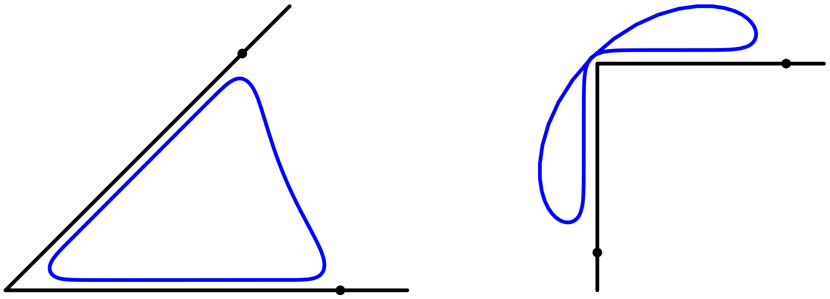

Figure A.6: (a) For $\theta_c \leq \pi$ and large ρ, the vortex conforms to the shape of the corner boundary. Here $\theta_c = \pi/4$ and $\rho = 0.8$. (b) For $\theta_c > \pi$ and large ρ, the vortex boundary can become tangent to itself, which is unphysical because the speed is constant along the boundary and would therefore have two different values at the tangency point. Here $\rho = 0.64$ and $\theta_c = 3\pi/2$.

corner, by symmetry. This solution is not physically acceptable. It is possible to find the corresponding critical value ρ_c numerically, and as θ_c increases, ρ_c decreases. One can find further solutions for $\rho > \rho_c$; these self-intersecting solutions are not physically acceptable either. Presumably another solution family branches off at the critical value of ρ_c, with the solution beyond it consisting of two symmetric vortices with near-cusps. Finding it will be difficult, since the flow domain now has genus 2, which requires a completely different analysis.

Figure A.6(a) shows that as $\rho \to 1$ for $\theta_c < \pi$, the vortex starts to conform to the shape of boundaries and take the shape of a curvilinear triangle. While there do not seem to be any discussions in the literature of the asymptotics of the prime function as $\rho \to 1$, we see physically that the solution takes the form of two narrow flows of constant velocity along the boundary, connected by a stagnation point flow near the apex of the corner, with the outer side slightly curved. The velocity profile in the jets is parallel to the boundary and uniform, and the speed is just the speed of the fluid on the vortex boundary, which is given exactly by $q_0 = |A|\rho^{-1}$. The width of the jet d can be obtained from the relation $2q_0 d = -Sa\beta^{-1}(1 + \mu \log \rho)$, resulting from the difference in streamfunction between the two vortices. We find numerically that $\mu = m(1-\rho)^{-1}$ as $\rho \to 1$ with m depending on θ_c, but the form of m does not seem to be available from analysis. We are hence led to the leading-order result

$$d \sim -\frac{Sa\sqrt{\rho}}{2|A|}\left(1+\frac{m\log\rho}{1-\rho}\right). \tag{A.22}$$

We have only examined symmetric solutions, as in CSLF. We do have some evidence that no asymmetric solution exists in this problem: if one can be found in the same form as above, but with asymmetric stagnation points on the circle $|\zeta| = \beta$, then the condition that $W'(\zeta)$ vanish at the stagnation points becomes four equations in two unknowns and is found numerically to have no solution except for the symmetric case. This is not a fully rigorous proof however.

One could also generalize to multiple vortices along the bisector of the angle. A counting argument shows that this configuration has (multiple) solutions in the point vortex case, and then an approach such as that in Llewellyn Smith (2014) indicates that desingularized versions will exist. Finding them numerically will be a challenge, requiring higher genus SK functions.

The stability of the family of vortices could be examined using the same approach as in Crowdy, Llewellyn Smith, and Freilich (2013). The nondimensional growth rate is $\sigma = \lambda\Gamma/2\pi q_0^2$, where λ is the dimensional growth rate. The general stability problem combines stability of the interface shape and stability associated with displacements of the centroid. In the point vortex limit, one finds $\sigma \sim \lambda\rho d^2/\Gamma$ (up to multiplicative factors), where d is the distance to the point vortex. Hence the spectrum of neutral modes found in CLSF has high dimensional frequency when expressed in terms of variables relevant to the point vortex pair. This is consistent with the fact that in the point vortex limit the equilibrium solution obtained from (A.3) is neutrally stable with non-zero frequency for $\theta_c < \pi$, has 0 growth rate for $\theta_c = \pi$ and is unstable for $\theta_c > \pi$ (this does not appear to have been mentioned in the literature). Hence for $\theta_c > \pi$ the system is unstable for arbitrary small ρ, and there is not much sense examining it for general ρ. As ρ increases, one can no longer separate displacement and shape instability. The stability problem is formulated in the complex w-plane, in which the vortex takes a simple shape, which is then transformed to the ζ-plane. An important difference is that there is now only one vortex, along with a solid boundary at $|\zeta| = \beta$, at which, in the notation of CLSF, $\hat{\delta} = \partial\Phi/\partial r = 0$, where $\hat{\delta}$ now designates the streamfunction perturbation along the solid boundary. We do not pursue the calculation further. It now contains θ_c-dependence, and preliminary indications suggest that as θ_c approaches 0 or π, the calculations become numerically delicate. Away from this range, one can find a critical instability threshold $\rho_c(\theta_c)$, with indications of multiple bubbles of instability (typical of Hamiltonian stability problems) in the system. The current stability problem, which has one free surface and one solid boundary, seems to have fewer degrees of freedom than that of CLSF; the values obtained for ρ_c do seem larger, of the order of 0.08–0.12. More work is required to understand the stability problem fully.

A.7 Conclusion

A stationary hollow vortex surrounded by irrotational flow has been found inside a wedge of fluid bounded by a corner of arbitrary angle using a conformal mapping approach. This is the first combined use of the SK prime function with algebraic functions to the authors' knowledge. For special values of θ_c, namely divisors of π such as $\pi/2$, $\pi/3$, $\pi/4$ and so on, it should be possible to construct the solution using higher-genus SK prime functions and symmetries. The algebra would rapidly become unmanageable, however, although presumably the final form of the solution would lead to identities between SK functions of different genus.

The problem of a steady vortex patch in a corner does not seem to have been investigated in detail, although the propagating vortex patch dipole has been examined

Deem and Zabusky (1978), Pierrehumbert (1980), and Saffman and Tanveer (1982). The Sadovskii dipole (or patch sheet), a vortex patch bounded by a vortex sheet, is a generalization of both Sadovskii (1971) and Tanveer (1986). Similarly one could examine patch sheet equilibria in a corner.

Perturbing the point vortex equilibrium with potential (A.2) leads to periodic motion for $\theta_c < \pi$. The general case of a point vortex in a right-angle corner was investigated by Suh (1993), and its transport properties provide an interesting model problem for non-periodic transport (authors' unpublished observations). The case of the point vortex in the corner could be examined similarly. For the hollow vortex, the problem is much more difficult, since the vortex sheet would evolve and would have to be obtained using a numerical approach similar to those used for water waves in e.g. Vanden-Broeck (2010) or Baker and Xie (2011).

A.8 Formulation using P, K and L

For ease of comparison with Crowdy, Llewellyn Smith, and Freilich (2013), we provide here the relevant formulas in terms of the definitions of the SK functions used in that work. For the annulus, the SK prime function and required related functions are defined by

$$P(\zeta, \rho) = (1 - \zeta) \prod_{k=1}^{\infty} (1 - \rho^{2k}\zeta)(1 - \rho^{2k}\zeta^{-1}) = -a^{-1} \prod_{k=1}^{\infty} \left(1 - \rho^{2k}\right) \omega(a\zeta, a), \tag{A.23}$$

and

$$K(\zeta, \rho) = \frac{\zeta P'(\zeta, \rho)}{P(\zeta, \rho)}, \qquad L(\zeta, \rho) = \zeta K'(\zeta, \rho). \tag{A.24}$$

Primes indicate derivatives with respect to ζ. Below we will suppress the ρ in the argument list. Then

$$W(\zeta) = \frac{\mathrm{i}Sb}{\beta}\left[K(\zeta/\beta) + K(\zeta\beta)\right] + \frac{\Gamma}{2\pi\mathrm{i}}\log\zeta = \frac{\mathrm{i}Sb}{\beta}\left[K(\zeta/\beta) + K(\zeta\beta) - \mu\log\zeta\right], \quad \text{(A.25)}$$

which is formally the same (with U replaced by S and a replaced by b) as in Crowdy, Llewellyn Smith, and Freilich (2013), and

$$R(\zeta) = \frac{A}{\zeta}\frac{P(\zeta/\alpha)P(\zeta/\bar{\alpha})}{P(\zeta\bar{\alpha})P(\zeta\alpha)}\left(\frac{P(-\zeta/\beta)P(\zeta\beta)}{P(-\zeta\beta)P(\zeta/\beta)}\right)^{1-\theta_c/\pi}, \quad \text{(A.26)}$$

where we have used the fact that β is real. Equation (24) of Crowdy, Llewellyn Smith, and Freilich (2013) is

$$L(\mathrm{e}^{\mathrm{i}\Theta}) + L(\rho\mathrm{e}^{\mathrm{i}\Theta}) = \mu. \quad \text{(A.27)}$$

Appendix A, in full, has been published in the *Journal of Fluid Mechanics*, "Hollow vortex in a corner" by T. W. Christopher and S. G. Llewellyn Smith, 2021, **908**, R2 (Cambridge University Press). The dissertation author was the primary investigator and author of this material.

Bibliography

Arslan, A., G. Fantuzzi, J. Craske, and A. Wynn (2021). “Bounds on heat transport for convection driven by internal heating”. *J. Fluid Mech.* 919, A15.

Austin, J. (2020). *Radiatively Driven Convection, 2019 field campaign.* Retrieved from the Data Repository for the University of Minnesota.

Austin, J. A. (2019). “Observations of radiatively driven convection in a deep lake”. *Limnol. Oceanogr.* 64.5, 2152–2160.

Baker, G. R. and C. Xie (2011). “Singularities in the complex physical plane for deep water waves”. *J. Fluid Mech.* 685, 83–116.

Bouillaut, V., S. Lepot, S. Aumâitre, and B. Gallet (2019). “Transition to ultimate regime in a radiatively driven convection experiment”. *J. Fluid Mech.* 861.R5, 1–12.

Chandrasekhar, S. (1961). *Hydrodynamic and Hydromagnetic Stability.* Oxford University Press.

Chernyshenko, S. I., P. Goulart, D. Huang, and A. Papachristodoulou (2014). “Polynomial sum of squares in fluid dynamics: a review with a look ahead”. *Phil. Trans. R. Soc. A* 372.2020, 20130350.

Coenen, W., A. Sánchez, R. Félez, K. Davis, and G. Pawlak (2021). “Residual streaming flows in buoyancy-driven cross-shore exchange”. *J. Fluid Mech.* 920, A1.

Crowdy, D. G. (2020). *Solving Problems in Multiply Connected Domains.* Philadelphia: SIAM.

Crowdy, D. G., S. G. Llewellyn Smith, and D. V. Freilich (2013). “Translating hollow vortex pairs”. *Eur. J. Mech. B/Fluids* 37, 180–186.

Davis, S. H. (1976). “The stability of time-periodic flows”. *Annu. Rev. Fluid Mech.* 8.1, 57–74.

Deconinck, B. and J. N. Kutz (2006). “Computing spectra of linear operators using the Floquet–Fourier–Hill method”. *J. Comput. Phys.* 219.1, 296–321. ISSN: 0021-9991.

Deem, G. S. and N. J. Zabusky (1978). "Vortex waves: stationary "V states", interactions, recurrence and breaking". *Phys. Rev. Lett.* 40, 859–862.

Deng, G., G. Biondini, and S. Trillo (2016). "Small dispersion limit of the Korteweg–de Vries equation with periodic initial conditions and analytical description of the Zabusky–Kruskal experiment". *Physica D* 333. Dispersive Hydrodynamics, 137–147. ISSN: 0167-2789.

Doering, C. R. and P. Constantin (1992). "Energy dissipation in shear driven turbulence". *Phys. Rev. Lett.* 69.11, 1648.

— (1996). "Variational bounds on energy dissipation in incompressible flows. III. Convection". *Phys. Rev. E* 53.6, 5957–5981.

Doering, C. R. and J. D. Gibbon (1995). *Applied Analysis of the Navier-Stokes Equations.* Cambridge Texts in Applied Mathematics. Cambridge University Press.

Fantuzzi, G. (2018). "Bounds for Rayleigh–Bénard convection between free-slip boundaries with an imposed heat flux". *J. Fluid Mech.* 837, R5.

Frisch, U. (1995). *Turbulence: the legacy of A. N. Kolmogorov.* Cambridge University Press.

Galdi, G. P., B. Straughan, and S. Chandrasekhar (1985). "A nonlinear analysis of the stabilizing effect of rotation in the Bénard problem". *Proc. R. Soc. Lond. A Mat.* 402.1823, 257–283.

Gershuni, G. Z. and E. M. Zhukhovitskii (1963). "On parametric excitation of convective instability". *J. Appl. Math. Mech.-USS* 27.5, 1197–1204.

— (1976). *Convective stability of incompressible fluids.* Keter Publishing House Jerusalem Ltd.

Goluskin, D. (2016). *Internally heated convection and Rayleigh-Bénard convection.* Springer.

Hazra, S., K. Kumar, and S. Mitra (2020). "Rayleigh-Bénard magnetoconvection with temperature modulation". *Proc. R. Soc. Lond. A* 476.2242, 20200289.

Holmgren, M. (2006). *XSteam for MATLAB.*

Homsy, G. M. (1974). "Global stability of time-dependent flows. Part 2. Modulated fluid layers". *J. Fluid Mech.* 62.2, 387–403.

Howard, L. N. (1963). "Heat transport by turbulent convection". *J. Fluid Mech.* 17.3, 405–432.

Hsu, C. P., C. F. Hung, and J. Y. Liao (2018). "A Chebyshev Spectral Method with Null Space Approach for Boundary-Value Problems of Euler-Bernoulli Beam". *Shock Vib.* 2018.

Joseph, D. D. (1976). *Stability of Fluid Motions I.* Springer-Verlag.

Llewellyn Smith, S. G. (2014). "Desingularized propagating vortex equilibria". *Fluid Dyn. Res.* 46, 061419.

Llewellyn Smith, S. G. and D. G. Crowdy (2012). "Structure and stability of hollow vortex equilibria". *J. Fluid Mech.* 691, 178–200.

Lu, L., C. R. Doering, and F. H. Busse (2004). "Bounds on convection driven by internal heating". *J. Math. Phys.* 45.7, 2967–2986.

Malkus, W. V. (1954). "The heat transport and spectrum of thermal turbulence". *Proc. R. Soc. Lond. A* 225.1161, 196–212.

Marchioro, C. (1994). "Remark on the energy dissipation in shear driven turbulence". *Physica D* 74, 395–398.

Michell, J. H. (1890). "On the theory of free stream lines". *Phil. Trans. R. Soc. Lond. A* 181, 389–431.

Or, A. C. (2001). "Onset condition of modulated Rayleigh-Bénard convection at low frequency". *Phys. Rev. E* 64, 050201-1–050201-3.

Or, A. C. and R. E. Kelly (1999). "Time-modulated convection with zero mean temperature gradient". *Phys. Rev. E* 60.2, 1741–1747.

Paparella, F. and W. R. Young (2002). "Horizontal convection is non-turbulent". *J. Fluid Mech.* 466, 205–214.

Pierrehumbert, R. T. (1980). "A family of steady, translating vortex pairs with distributed vorticity". *J. Fluid Mech.* 99, 129–144.

Pocklington, H. C. (1894). "The configuration of a pair of equal and opposite hollow straight vortices of finite cross-section, moving steadily through the fluid". *Proc. Camb. Philos. Soc.* 8, 178–187.

Rayleigh, L. (1916). "On convection currents in a horizontal layer of fluid, when the higher temperature is on the under side". *Lond. Edinb. Dublin Philos. Mag. J. Sci.* 32.192, 529–546.

Rocha, C. B., N. C. Constantinou, S. G. Llewellyn Smith, and W. R. Young (2020). “The Nusselt numbers of horizontal convection”. *J. Fluid Mech.* 894, A24.

Sadovskii, V. S. (1971). “Vortex regions in a potential stream with a jump of Bernoulli’s constant at the boundary”. *App. Math. Mech.* 35, 729–735.

Saffman, P. G. and S. Tanveer (1982). “The touching pair of equal and opposite uniform vortices”. *Phys. Fluids* 25, 1929–1930.

Serrin, J. (1959). “On the stability of viscous fluid motions”. *Arch. Ration. Mech. An.* 3.1, 1–13.

Souhar, K. and S. Aniss (2016). “Effect of Phase Thermal Modulation Without Stationary Temperature Gradient on the Threshold of Convection”. *J. Heat Transfer* 138.10, 102502-1–102502-8.

Straughan, B. (2013). *The energy method, stability, and nonlinear convection.* Vol. 91. Springer Science & Business Media.

Suh, Y. K. (1993). “Periodic motion of a point vortex in a corner subject to a potential flow”. *J. Phys. Soc. Japan* 62, 3441–3445.

Tanveer, S. (1986). “A steadily translating pair of equal and opposite vortices with vortex sheets on their boundaries”. *Stud. Appl. Math.* 74, 139–154.

Trefethen, L. N. (2000). *Spectral Methods in MATLAB.* SIAM.

Vanden-Broeck, J.-M. (2010). *Gravity-capillary free-surface flows.* Cambridge: Cambridge University Press.

Venezian, G. (1969). “Effect of modulation on the onset of thermal convection”. *J. Fluid Mech.* 35.2, 243–254.

Wasow, W. (1985). *Linear turning point theory.* Vol. 54. Springer Science & Business Media.

Weideman, J. A. and S. C. Reddy (2000). “A MATLAB differentiation matrix suite”. *ACM T Math. Software* 26.4, 465–519.

Yang, R., K. L. Chong, Q. Wang, R. Verzicco, O. Shishkina, and D. Lohse (Oct. 2020). “Periodically Modulated Thermal Convection”. *Phys. Rev. Lett.* 125 (15), 154502.

Yih, C.-S. and C.-H. Li (1972). “Instability of unsteady flows or configurations. Part 2. Convective instability”. *J. Fluid Mech.* 54.1, 143–152.